Effet de la porosité dans les réservoirs composites à parois épaisses : Observations expérimentales et modélisation numérique

Jan Rojek

PSL
UNIVERSITÉ PARIS

THÈSE DE DOCTORAT
DE L'UNIVERSITÉ PSL

Préparée à MINES ParisTech

Effect of voids in thick-walled composite pressure vessels: Experimental observations and numerical modelling

Effet de la porosité dans les réservoirs composites à parois épaisses : Observations expérimentales et modélisation numérique

Soutenue par
Jan ROJEK
Le 4 juin 2020

École doctorale n°621
Ingénierie des Systèmes, Matériaux, Mécanique, Energétique

Spécialité
Mécanique

Composition du jury :

Christophe BOUVET Professeur des universités, ISAE-SUPAERO	*Président*
Janice BARTON Professor, University of Bristol	*Rapporteur*
Laurent GUILLAUMAT Professeur des universités, ENSAM Angers	*Rapporteur*
Hélène WELEMANE Maître de conférence, ENIT Tarbes	*Examinateur*
Lucien LAIARINANDRASANA Directeur de recherche, MINES ParisTech	*Examinateur*
Sébastien JOANNES Chargé de recherche, MINES ParisTech	*Examinateur*
Alain THIONNET Professeur des universités, MINES ParisTech, Université de Bourgogne	*Directeur de thèse*

MINES ParisTech | PSL

Contents

Funding

The research presented in this thesis was done within the framework of the FiBreMoD project and has received funding from the European Union's Horizon 2020 research and innovation programme under the Marie Skłodowska-Curie grant agreement No 722626.

Acknowledgements

The results presented in this thesis were obtained over the course of over three years. During this time, I had the great luck of meeting multiple people who have had a deep positive influence both on my scientific work and on my personal life.

First, I need to acknowledge Alain Thionnet, who was the main supervisor during this PhD. Sébastien Joannès, also supervising this thesis, was always willing to help, both with his scientific questions, as well as with everyday problems one encounters moving to a new country. Lucien Laiarinandrasana and Anthony Bunsell, while not official supervisors, were always eager to help and share their extensive knowledge. I also owe a debt of gratitude to the whole scientific, technical and administrative staff at Centre des Matériaux. I want to thank Janice Barton and Laurent Guillaumat, who were the external reviewers of this thesis. Finally, I need to mention the other members of the defence jury: Hélène Welemane and Christophe Bouvet.

The thesis was part of the European Union's Maria Skłodowska-Curie ITN project FiBreMoD. During its course, I had a unique chance to spend periods of time at several partner institutions: University of Southampton, BAM Berin, KU Leuven and Siemens. I wish to extend my gratitude to the researchers who received me and shared their expertise: Ian Sinclair, Mark Mavrogordato, Georg Mair, Eric Duffner, Yentl Swolfs, Larissa Gorbatikh and Laszlo Farkas.

I am also grateful to my colleagues: Ana, Ashok, Aurélien, Faisal, Joseph, Martinus, Richi and the other PhD candidates in FiBreMoD. I learned a lot from them and I am happy to have them as friends.

Finally, I want to deeply thank my family, especially my parents, for always giving me their love and being there for me. This PhD was a long journey that I could not complete without their support.

Chapter 1

Introduction

Chapitre 1. Introduction

La réduction de l'empreinte écologique de notre activité est l'un des plus grands enjeux de notre société en ce début de siècle. Parmi les principaux leviers figurent la transition vers des mobilités plus propres. La réduction des masses portantes en ayant davantage recours aux matériaux composites doit s'accompagner d'une transition vers des solutions énergétiques plus vertueuses. Les voitures exploitant les piles à combustible à hydrogène sont une alternative prometteuse. Néanmoins, à cause de sa faible densité à pression atmosphérique, l'hydrogène doit être stocké à haute pression pour des applications embarquées. Cela nécessite des compromis entre la légèreté des réservoirs et leur capacité à résister à des fortes pressions internes (700 bar). Les matériaux composites à fibres de carbone remplissent ces critères.

Les réservoirs à haute pression à base de fibres de carbone sont typiquement fabriqués par enroulement filamentaire. C'est un procédé qui peut être automatisé, ce qui permet de réaliser de gains de productivité. Par contre, les structures fabriquées par cette méthode peuvent contenir un taux de porosité significatif. Il est donc important de comprendre l'influence de ces porosités sur la résistance du matériau. En outre, les réservoirs à haute pression exigent des structures composites à parois épaisses rendant difficile l'examen au cœur du matériau. Couplé à cela, un état de contraintes multi-axial s'exerce sur le matériau en particulier sur les couches les plus internes.

Le caractère fragile des fibres de carbone donne lieu à une importante dispersion expérimentale de la contrainte à rupture. Un grand nombre d'essais est nécessaire afin d'évaluer la distribution. La résistance non-uniforme des fibres est le facteur principal régissant le comportement d'un matériau composite unidirectionnel sollicité en traction longitudinale. Au fur et à mesure que le matériau est chargé, des fibres commencent à se casser d'une manière aléatoire. Un état de contrainte complexe se développe autour de ces ruptures individuelles. La charge doit être distribuée de la fibre cassée aux fibres voisines intactes, ce qui augmente la probabilité d'une nouvelle rupture à proximité de la fracture existante. Enfin, les ruptures se regroupent de plus en plus, ce qui amène finalement la défaillance du composite.

Bon nombre d'approches numériques ont été proposées pour modéliser la défaillance d'un composite unidirectionnel en traction longitudinale se basant sur la cinétique des ruptures de fibres. L'un d'entre eux est le modèle multiéchelle de Blassiau, Bunsell et Thionnet, développé à MINES ParisTech [9]. Les travaux numériques présentés dans cette thèse s'inscrivent dans le contexte de ce modèle existant, qui est présenté dans le Chapitre 2. La détermination d'un domaine élémentaire représentatif du phénomène de rupture des fibres au sein du composite est abordé dans le Chapitre 3. Le Chapitre 4 est dédié à la caractérisation des porosités au sein du réservoir composite servant de référence pour l'étude. Des observations en tomographie aux rayons X ainsi qu'en microscopie optique fournissent les paramètres morphologiques nécessaires à la modélisation. Le Chapitre 5 présente une étude expérimentale et numérique d'une résine époxy utilisée pour la réalisation de réservoirs composites. L'effet d'un état de contrainte triaxial sur la résine est particulièrement investigué. Afin d'évaluer la conséquence des porosités macroscopiques sur la résistance en chargement combiné de traction-compression à travers l'épaisseur, une étude expérimentale est menée sur des éprouvettes représentatives dans le Chapitre 6. Le Chapitre 7 présente l'intégration des observations précédentes dans une simulation du comportement à rupture d'un réservoir modèle. Un critère de rupture phénoménologique est par ailleurs proposé. Enfin, le Chapitre 8 résume les principaux résultats obtenus dans ce travail.

1.1 Industrial context

Reducing the ecological footprint of our economy is one of the biggest challenges currently facing the scientific and industrial world. The Paris Agreement signed in 2016 puts forward the objective of limiting the increase in global temperatures to below 2 °C of the pre-industrial levels. An important part of this effort is cutting down emissions in the transportation sector, which is one of the major polluters. Reducing the weight of the structural parts is among the most effective methods of limiting vehicle emissions. This means that increasing the proportion of lightweight composite materials in structural applications is a necessity.

Another important objective is the transition from fossil fuels to other energy sources. For the automotive industry, this means phasing out the internal combustion engine, which has been the standard for the past century. Hydrogen fuel cells, which produce electricity without polluting by-products, are a promising alternative. In recent years, countries such as Japan, United States and Germany have seen strong investment into hydrogen-based mobility, resulting in a growing number of fuel cell vehicles. The French government is also promoting the increased presence of hydrogen in the energy mix [99]. Nonetheless, the popularity of fuel cell vehicles is still significantly lower than that of battery electric vehicles. This can be firstly attributed to a larger effort required to set up the production and supply chains for hydrogen. Another challenge is the on-board storage of hydrogen required to power the fuel cells. Due to its low energy per volume at atmospheric pressure, hydrogen needs to be compressed to be stored in sufficient amounts for on-board applications. A service pressure in commercially available cars is 700 bar. This requires storage vessels capable of withstanding very high loads, while also being lightweight. Composite materials, and in particular carbon fibre reinforced polymers (CFRP), meet both criteria and are being widely adopted for this application.

Pressure vessels (cylinders, tanks) are commonly used in a large number of industrial applications. In the past, steel was the material of choice used in their manufacture. An early application was the steam engine. It was widely used in steam locomotives that for the first time in history enabled mass long-distance travel. These early pressure vessels suffered from frequent accidents, which led to the introduction of the first safety regulations in the nineteenth century [91]. With the appearance of fibre-reinforced composites, their attractiveness for pressure vessel manufacture was soon realized. Carbon fibre reinforced composites provide an excellent strength-to-weight ratio. However, they also come with certain disadvantages. Damage often accumulates at the microscopic scale that is difficult to monitor effectively in large structures. Due to the brittle behaviour of the fibres, the failure of a composite structure often takes place without easily identifiable warning signs at the macroscale. Additionally, the strength of composite structures can show significant scatter, further complicating the task of the designer. For on-board

applications, safety is the ultimate concern. In absence of reliable predictive tools, high safety factors are therefore required. This leads to overdesigned structures, not fully utilizing the lightweight potential of the material.

To design more efficient and safer composite structures, an accurate knowledge of the stochastic strength distribution is required. This can be achieved by manufacturing a large number of specimens and carrying out enough destructive tests to describe strength distribution of the whole population. However, this approach is often not practical and prohibitively expensive. Simulation provides an alternative approach. When a pressure vessel is filled with gas, its walls work principally in tension. For a composite-overwrapped cylinder, most of this tensile load is carried by fibres. As a result, the dominant failure mode is fibre breakage. Therefore, numerical modelling of the fibre break process provides a tool of predicting and better understanding damage accumulation and failure of composite pressure vessels.

Composite pressure vessels are typically manufactured through filament winding. In this process, a metallic or polymeric mandrel is overwrapped by resin-impregnated fibres. While the mandrel rotates, the yarn delivery eye moves along its axis. The ratio of the velocities of the mandrel and the delivery eye determines the angle at which the composite yarn is placed. The composite layers can be classified into hoop and helical layers.

Hoop layers are laid approximately perpendicular to the rotation axis and mostly carry circumferential loads. The other layers are described as helical and can carry both hoop and axial loads, depending on the lay angle. Filament winding is an attractive manufacturing method for composites, due to its automation potential, resulting in higher manufacturing efficiency and lower cost compared to other processes. However, fast manufacturing can come at a cost of a significant void content in the final product, sometimes close to 10 % [148]. Therefore, understanding and modelling the impact of void presence in filament-wound structures is of particular importance.

High pressures that need to be withstood by composite cylinders often result in a significant wall thickness, sometimes reaching 50 mm. Through the rest of this thesis, thick-walled cylinders as understood as those having the wall-thickness-to-cylinder-radius ratio higher than 0.1. In such case, the plane stress assumption is no longer justified. The bulk of the existing research is limited to thin-walled composites and it is not fully understood how much of this experience can be directly applied to thick-walled structures.

1.2 Materials and structures

1.2.1 Fibre-reinforced composite materials

Composite materials are defined as being made of two or more phases at the macroscopic scale. They consist of a reinforcement phase, which may come in the form of fibres or particles, embedded in a less stiff matrix phase. The composites studied in this thesis are continuous carbon fibre reinforced polymers (CFRP). Many materials are much stronger in fibrous form and fibre-reinforced composites allow taking advantage of that potential. The resultant materials are characterized by high stiffness in the longitudinal (fibre) direction and low density. This makes composites an attractive alternative to metallic materials, such as steel or aluminium, in many technical applications. Many types of technical fibres have been developed, e.g. glass, aramid, silicon carbide and carbon. Carbon fibres are most popular in high performance applications. Modern technical carbon fibres were first obtained in the late 1950s. They soon gained popularity thanks to their remarkable properties: high specific strength and stiffness, fatigue resistance, low weight, as well as good thermal and electrical conductivity. They have found a wide range of applications in areas such as: space and aeronautical, marine, automotive, sporting goods industry. Despite certain drawbacks, such as difficult processing, recycling, problematic damage monitoring, they have replaced metals in certain applications, in particular where light weight is an important consideration, e.g. in aircraft structures.

1.2.2 Fibre strength

Failure of single carbon fibres happens in a brittle manner and their strength shows a significant scatter. Fibre strength probability is usually described through the weakest link model, which assumes that fibre failure coincides with the failure of its weakest flaw. The flaw could be a surface defect, an inclusion or a feature of fibre nanostructure [20] [102] [4] [74] [177] [164] [112]. The most commonly used mathematical model of fibre strength is the two-parameter Weibull distribution [169]:

$$\Pr(\sigma_R \leq \sigma) = 1 - \exp\left[-\left(\frac{L}{L_0}\right)\left(\frac{\sigma}{\sigma_0}\right)^m\right], \tag{1.1}$$

expressing the probability of stress σ being greater than or equal to fibre strength σ_R. The other terms in the equation are: gauge length L, reference gauge length L_0, scale parameter σ_0 and shape parameter m. The formula predicts that fibre strength is a function of gauge length, with longer fibres failing at a lower stress. This phenomenon, observed experimentally, is a challenge in measuring fibre strength. It should be noted that despite its widespread use, the Weibull distribution has been shown not to be an accurate representation of the weakest link model [157].

The most common experimental method of fibre strength measurement is single fibre testing [19]. To reliably evaluate the strength distribution of a specific fibre type, a large number of tests is necessary [71]. Another issue is performing single fibre tests at short gauge lengths. In theory, the values of m and σ_0 obtained experimentally can be used to calculate fibre strength at an arbitrarily short gauge length using the Weibull distribution. However, it has been shown that this extrapolation diverges from the experimental results at short gauge lengths [64] [121] [166]. This is a logical conclusion, since otherwise fibre strength would increase to infinity for a gauge length approaching zero. Several alternatives to a two-parameter Weibull distribution have been proposed to better predict fibre strength, particularly at short gauge lengths [168] [43] [155].

1.2.3 Longitudinal tensile failure of fibre-reinforced composites

Fibre strength is the governing factor for the failure of unidirectional composites subjected to longitudinal tension. Non-uniform fibre strength stands at the basis of the generally accepted description of the tensile failure process. As the composite is loaded, individual filaments break at random locations throughout the composite, well before the final failure. A complex stress state develops around these random breaks. The load from the broken fibre is redistributed by the surrounding matrix, mostly through shear stress. The broken fibre recovers the far-field stress value at a certain distance from the break, called the recovery or ineffective length. An analytical solution to this problem is obtained through the shear-lag model first proposed by Cox, under the assumption of linear elastic fibres and matrix, with a perfect interface between the two [38]. The case of the perfectly plastic matrix is considered in the Cottrell-Kelly-Tyson model [37] [78].

Since the broken fibre can carry only a limited load along the recovery length, stress needs to be redistributed to the neighbouring intact fibres, leading to their overstressing in the vicinity of the break. As a result, there is an increased probability of a new fibre break appearing next to the existing one, creating a group of two adjacent breaks (2-plet). This further increases the stress on the surrounding intact fibres, promoting the formation of increasingly large i-plets. Eventually, after reaching a critical size, one of these i-plets becomes unstable, triggering the failure of the composite.

This classic description of the fibre break accumulation mechanism is owed to authors such as Hedgepeth [54], Rosen [132] and Zweben [181]. Experimental observations on model two-dimensional composites confirm the importance of stress concentrations around fibre breaks, as shown by Jones and DiBenedetto [75], Van den Heuvel et al. [162] [161] or Watanabe et al. [165]. However, modelling results

show that stress concentration factors are significantly lower for three-dimensional composites [55] [106]. Advances in X-ray computed microtomography have allowed a three-dimensional in-situ observation of damage propagation in real composite materials, confirming the gradual fibre break accumulation process [129] [136].

A number of numerical approaches have been developed to model the fibre break process in three dimensions. Apart from the multiscale model of Blassiau, Bunsell and Thionnet [9], discussed in more detail in this thesis, a non-exhaustive list includes the works of Okabe et al. [111], Pimenta and Pinho [122], Swolfs et al. [149] or Tavares et al. [153]. While the mechanism of fibre break accumulation seems to be well understood, the determination of appropriate input data remains an onerous task [150]. Predictions of load transfer around fibre breaks strongly depend on multiple factors, such as dynamic loads, plastic and time-dependent behaviour of the matrix, matrix cracking and fibre-matrix debonding around the breaks. Furthermore, no agreement exists on the fibre strength distribution at short gauge lengths, necessary to describe these microscopic phenomena. These issues pose a formidable challenge to the development of accurate models of the fibre break process. The existing approaches still do not fully capture all the microscopic failure phenomena [18].

1.3 Scientific objectives and thesis outline

The objective of the research presented in this thesis is to identify factors influencing pressure vessel strength, evaluate their significance and propose a way of including them in a numerical simulation. In particular, the influence of voids and multiaxial stresses are studied. These two aspects have been rarely considered in the existing literature concerning pressure vessels.

Given that fibre breakage is the dominant failure mode in pressure vessels, the modelling work is performed in the framework of the multiscale fibre break model of Blassiau et al. The assumptions of the model and the multiscale algorithm are introduced in Chapter 2. The phenomena unaccounted for in the existing approach are discussed.

The determination of a representative volume element (RVE) of the fibre break process is discussed in Chapter 3. First, a mathematical framework is introduced, tying the RVE choice to the notions of a stationary ergodic random function and integral range. Then, a numerical study is presented, in which the fibre break process is studied numerically in microscopic cells of various sizes and shapes. The results are interpreted in the framework of the introduced mathematical concepts introduced earlier and the topology of the fibre break process is analyzed.

Chapter 4 is dedicated to the characterization of the void content in a

thick-walled carbon-epoxy pressure vessel. X-ray computed tomography and optical microscopy are used to image the microstructure of the composite cylinder wall. Image processing algorithms are proposed and implemented in order to measure composite orientation and void volume fraction. The observations confirm the presence of a significant void content in filament-wound structures. From the tomography volumes, a segmentation of voids is carried out in three dimensions, providing information on individual void properties, such as size, shape and orientation.

Chapter 5 presents an experimental and numerical study of a thermosetting epoxy resin, used as matrix in fibre-reinforced composites. The work investigates growth of microscopic voids, at a smaller scale than observed earlier in the pressure vessel. The effect of stress triaxiality is investigated through tensile tests on double-notched round epoxy bars. Then, scanning electron microscopy and tomography observations are carried out to quantify void growth. The results are used to optimize a finite element model of the epoxy. The obtained model can be applied to realistically model the mechanical response of the matrix at the microscale of a composite material.

In Chapter 6, an experimental study is presented, aimed at evaluating the effect of macroscopic voids and a through-thickness compressive stress on the tensile strength of a carbon-epoxy composite. A biaxial load is applied to mimic the stress state in a thick-walled pressure vessel. A custom mechanical testing setup is designed in order to apply different combinations of biaxial loading. Mechanical tests on specimens with different levels of void content demonstrate the reduction in tensile strength due to through-thickness compression and the detrimental effect of voids under this type of loading.

Chapter 7 presents simulations of a thick-walled pressure vessels using the multiscale fibre break model. The numerical model is extended to account for the tendencies observed experimentally. Two methods are proposed to account for the presence of macroscopic voids. Additionally, a modified phenomenological fibre failure criterion is proposed to account for the influence of biaxial stresses. Several examples of numerical simulations are presented to evaluate the performance of the numerical approach.

Chapter 8 summarizes the main results presented in this thesis. Finally, possible directions of future investigation are discussed.

Chapter 2

Review of the MINES ParisTech multiscale fibre break model

Chapitre 2. Exposé du modèle multiéchelle de rupture des fibres de MINES ParisTech

Le travail numérique présenté dans cette thèse s'inscrit dans la continuité d'un modèle multiéchelle développé à MINES ParisTech par Blassiau, Bunsell et Thionnet [9]. Ce modèle permet de simuler la rupture d'un composite unidirectionnel sollicité en traction longitudinale. Il est basé sur les principaux mécanismes microstructuraux conduisant à la rupture d'un UD et notamment l'accumulation des ruptures de fibres et le report de charge au cours du temps. Les structures composites sont composées des millions de fibres individuelles, ce qui rend une simulation directe de l'endommagement à l'échelle microscopique irréalisable. Le modèle multiéchelle discuté ici permet de répondre à cet enjeu tout en conservant une réalité physique.

A l'échelle microscopique, le phénomène de rupture des fibres est modélisé dans un volume élémentaire représentatif (VER). Un nombre fini d'états d'endommagement est défini dans ce VER et pour chaque cas un coefficient de surcharge est calculé, décrivant l'effet de la distribution des contraintes autour des filaments cassés. Sur structure, la simulation par éléments finis n'est réalisée qu'à l'échelle macroscopique et les valeurs des coefficients de surcharge précalculées sont utilisées pour rendre compte de ce qui se déroule aux échelles les plus fines.

Avant le début d'une simulation, les valeurs aléatoires des contraintes à rupture des fibres sont attribuées dans chaque VER. Pour chaque pas de temps de la simulation numérique, quatre étapes peuvent être identifiées : la solution macroscopique par élément finis, la localisation, la solution microscopique et l'homogénéisation. L'algorithme du procédé multiéchelle ainsi que les connexions entre les différentes étapes sont expliquées dans ce chapitre.

Une évaluation critique du modèle est menée afin d'identifier les pistes d'améliorations possibles. Parmi ces pistes, les porosités aux différentes échelles du matériau semblent être l'élément principal à considérer. L'étude de ce phénomène a une importance particulière pour le cas des réservoirs à parois épaisses où l'on trouve souvent des taux de porosité élevés.

2.1 Introduction

The modelling work presented in this thesis is largely done in the framework of the multiscale fibre break model developed at MINES ParisTech by Blassiau, Bunsell and Thionnet [9]. The model offers a method of simulating tensile failure of a unidirectional composite material loaded in the longitudinal (fibre) direction. Under these conditions, the majority of the load is carried by the fibres, due to their much higher stiffness compared to the matrix. Failure of the structure is caused by an accumulation of single filament breaks, as described in Section 1.2.3.

A single carbon fibre has a diameter of 5 µm to 7 µm. This means that even small composite specimens contain thousands of fibres, making a direct simulation of damage accumulation at the microscale impractical for most purposes. The multiscale model of Blassiau et al. was developed to address this problem. It combines an analysis of the damage process at two scales, providing a link between the micromechanics of load transfer around individual fibre breaks and the macroscopic mechanical response at the structural level. A good agreement has been shown between the model's predictions and experimental data coming from acoustic emission [26] and micro-computed tomography [138].

In this chapter, we review the assumptions of the model and its performance. First, a succinct description of the model is presented. For a more exhaustive explanation, the reader can refer to other works [9] [10] [11] [12]. Next, the results of the model are shown on the example of a simulation of tensile fialure of a unidirectional carbon-epoxy coupon. Finally, a discussion is provided on the phenomena that have not been accounted for in the modelling and their significance for pressure vessel simulation. Based on these considerations, we choose the phenomena that will be further explored in this thesis.

2.2 Summary of the fibre break model

2.2.1 Description of the model at the microscopic scale

At the microscale, the unidirectional composite is modelled as non-homogeneous, considering separately the fibre and matrix material behaviours. Fibres are assumed to be perfectly aligned and distributed in a regular square array. A periodic representative volume element (RVE) is defined, consisting of 32 fibres of 4 mm length, as shown in Figure 2.1. RVE represents a microscopic volume of the studied material that is sufficiently large to predict a macroscopic property of interest - here, the longitudinal tensile strength. Based on an earlier study which determined six fibres as the size of a two-dimensional RVE [2], a cell of 6×6 fibres is assumed to constitute an RVE in a three-dimensional space. Because of geometric constraints,

the number of fibres is set to 32. The determination of RVE size is discussed in more detail in Chapter 3.

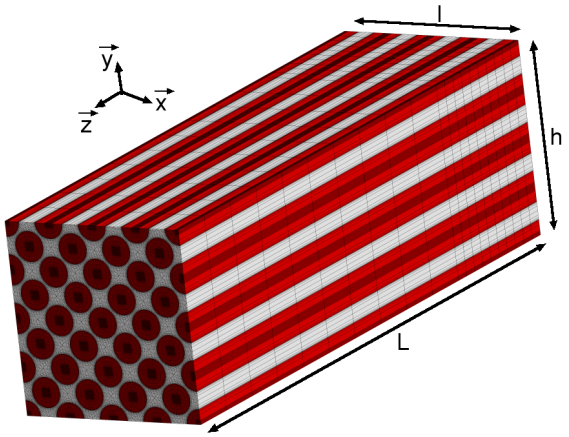

Figure 2.1: Cell representative of the RVE (for $V_f = 0.64$): $L = 4$ mm, $l = h = 0.05$ mm).

The pristine RVE with no fibre breaks is referred to as CS-32. Six damage states are defined in the RVE, corresponding to 1, 2, 4, 8, 16 and 32 broken fibres. Each fibre in the RVE is allowed to break only once and all fibres break in the same plane (the symmetry plane of the RVE). The RVE cells corresponding to the damage states are referred to as C-32 for 1 in 32 fibres broken, C-16 for 1 in 16 fibres broken, and analogously C-8, C-4, C-2 and C-1. These cells are represented in Figure 2.2. The damaged cells can also be defined in terms of i-plets ($i = 1, 2, 4, 8, 16, 32$), where i is the number of fibre breaks in the cell. For each of the damaged cells, stresses are computed through finite element analysis. The presence of broken filaments leads to overstressing of surrounding unbroken fibres. The magnitude of this overstressing is expressed through the load transfer coefficient k_r, defined as

$$k_r\left(C, V_f, F, d, t, z\right) = \frac{\int_{Z_i}^{Z_{i+1}} \int_{S_F} \sigma_{zz}^m\left(C, V_f, F, d, t, x, y, z\right) \mathrm{d}x\mathrm{d}y\mathrm{d}z}{\int_{Z_i}^{Z_{i+1}} \int_{S_F} \sigma_{zz}^m\left(\mathrm{CS}-32, V_f, F, d=0, t=0, x, y, z\right) \mathrm{d}x\mathrm{d}y\mathrm{d}z}, \tag{2.1}$$

where C is the damage state, V_f is the fibre volume fraction, F refers to the considered fibre, d is the debonding length around the break, t is time and z is the coordinate along the fibre from the plane of failure ($z = 0$); Z_{i+1} and Z_i are the abscissa of the plane sections between which k_r is calculated. The equation above describes the ratio of average stress in a fibre in a given damaged configuration to the stress in that fibre in the pristine state.

Since breaks are assumed to appear uniquely in one plane, k_r needs to be considered only for $z = 0$. The number of variables in the equation is further reduced by only considering the most loaded fibre. Furthermore, a constant debonding length

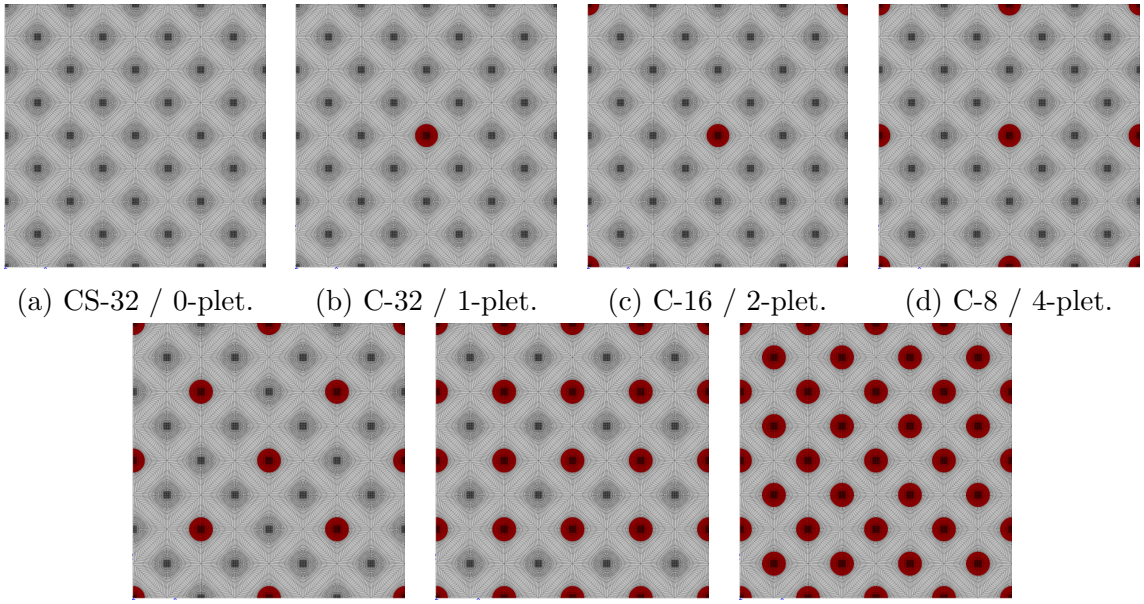

(a) CS-32 / 0-plet. (b) C-32 / 1-plet. (c) C-16 / 2-plet. (d) C-8 / 4-plet.

(e) C-4 / 8-plet. (f) C-2 / 16-plet. (g) C-1 / 32-plet.

Figure 2.2: Representative cells of the material damage state and corresponding i-plets. Broken fibres are shown in red.

of 35 µm on either side of the break is assumed. Under these conditions, the load transfer coefficient can be expressed as

$$k_r^{max}\left(C, V_f, t\right) = \frac{\int_{Z_i}^{Z_{i+1}} \int_{S_F} \sigma_{zz}^m \left(C, V_f, d = 35\mu\mathrm{m}, t, x, y, z = 0\right) \mathrm{d}x\mathrm{d}y\mathrm{d}z}{\int_{Z_i}^{Z_{i+1}} \int_{S_F} \sigma_{zz}^m \left(\mathrm{CS}-32, V_f, d = 0, t = 0, x, y, z = 0\right) \mathrm{d}x\mathrm{d}y\mathrm{d}z}. \quad (2.2)$$

The value of k_r^{max} depends only on the damage state C, fibre volume fraction V_f and time t. Thanks to the limited number of allowed damage states, the values of the coefficient k_r^{max} can be precomputed and stored in a database under the form of a function K_r^{max}:

$$K_r^{max}(C, V_f, t) = K_r'(C, V_f) + K_r^d(C, V_f) + K_r^t(t), \quad (2.3)$$

where K_r' is the contribution of the fibre break without debonding, K_r^d appears due to the debonding length of 35 µm and K_r^t is the time-dependent coefficient originating from the viscous behaviour of the matrix. For the purposes of the simulation, the three components of the load transfer coefficient are represented through smoothing functions:

$$K_r^{max}(C, V_f, t) = \underbrace{\left[K_0 + a_0 \exp\left(-\frac{C}{b_0}\right)\right]}_{K_r'} + \underbrace{\left[K_{0d} + a_d \exp\left(-\frac{C}{b_d}\right)\right]}_{K_r^d} + \underbrace{\left[\sum_{i=1}^{5} a_t^i \left(1 + \exp\left(\frac{t}{b_t^i}\right)\right)\right]}_{K_r^t}, \quad (2.4)$$

where K_0, a_0, b_0, K_{0d}, a_d, b_d, a_i^t and b_i^t are fitting coefficients, dependent on the fibre volume fraction. The values of the coefficients K_r' and K_d are given for three different volume fractions in Tables 2.1 and 2.2. K_r^t depends only on time and is plotted in Figure 2.3.

K_r'	C32	C16	C8	C4	C2
$V_f = 19\%$	0.0570	0.0572	0.0700	0.1603	0.3485
$V_f = 39\%$	0.0737	0.0739	0.0879	0.1899	0.4057
$V_f = 64\%$	0.0735	0.0738	0.0893	0.1968	0.4183

Table 2.1: Values of the load transfer coefficient K_r' due to fibre breaks.

K_r^d	C32	C16	C8	C4	C2
$V_f = 19\%$	0.0342	0.0347	0.0603	0.2142	0.5072
$V_f = 39\%$	0.0175	0.0184	0.0518	0.2277	0.5380
$V_f = 64\%$	0.0228	0.0243	0.0651	0.2448	0.5314

Table 2.2: Values of the load transfer coefficient K_r^d due to debonding.

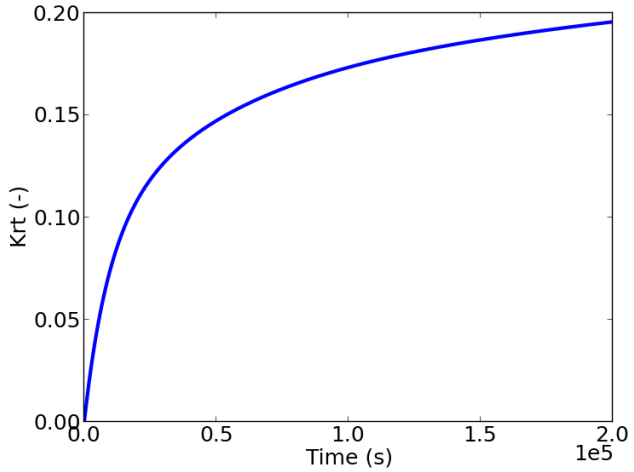

Figure 2.3: The values of the time-dependent load transfer coefficient K_r^t.

2.2.2 FE^2 simplified multiscale model for simulating failure of a composite structure

A multiscale FE^2 approach was developed for computational efficiency. It couples a calculation at the microscopic scale with a macroscale simulation homogenizing

fibres and matrix into a transversely isotropic material. The multiscale FE^2 process is defined as simplified, since the finite element problem is only solved at the macroscale, whereas the microscopic solution (the localization step) makes use of the database of precomputed load transfer coefficients $K_r^{max}(C, V_f, t)$. To build the finite element mesh, three-dimensional 8-node brick elements (C3D8) are used. Each element has eight Gauss points, each one corresponding to a single RVE. The resultant finite element has the dimensions 8.0 mm × 0.1 mm × 0.1 mm, as shown in Figure 2.4.

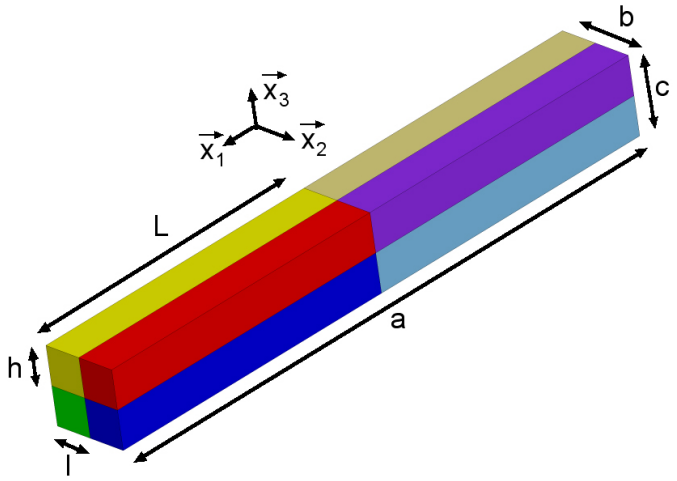

Figure 2.4: A C3D8 finite element of dimensions 8.0 mm × 0.1 mm × 0.1 mm, consisting of 8 RVEs.

Figure 2.5 shows the flowchart of the multiscale algorithm. Before the start of the simulation, five fibre strength values need to be assigned at each Gauss point. These values are randomly assigned from a two-parameter Weibull distribution, for a fibre gauge length of 4 mm, equal to the RVE length. In a similar way, local fibre volume fraction can be assigned at each Gauss point. For each time step of the simulation, four main stages can be identified: macroscopic finite element solution, localization, microscopic solution and homogenization. The consecutive steps of the algorithm are explained below.

Macroscopic solution In the macroscopic solution step, the composite is modelled using a homogenized linear elastic transversely isotropic material behaviour. The stiffness matrix at each Gauss point is assigned according to the local fibre volume fraction and the damage state. The applied loads are updated and the displacements at nodes are calculated using a standard finite element procedure. Once the nodal displacements are known, the macroscopic stress tensor at each Gauss point is readily obtained.

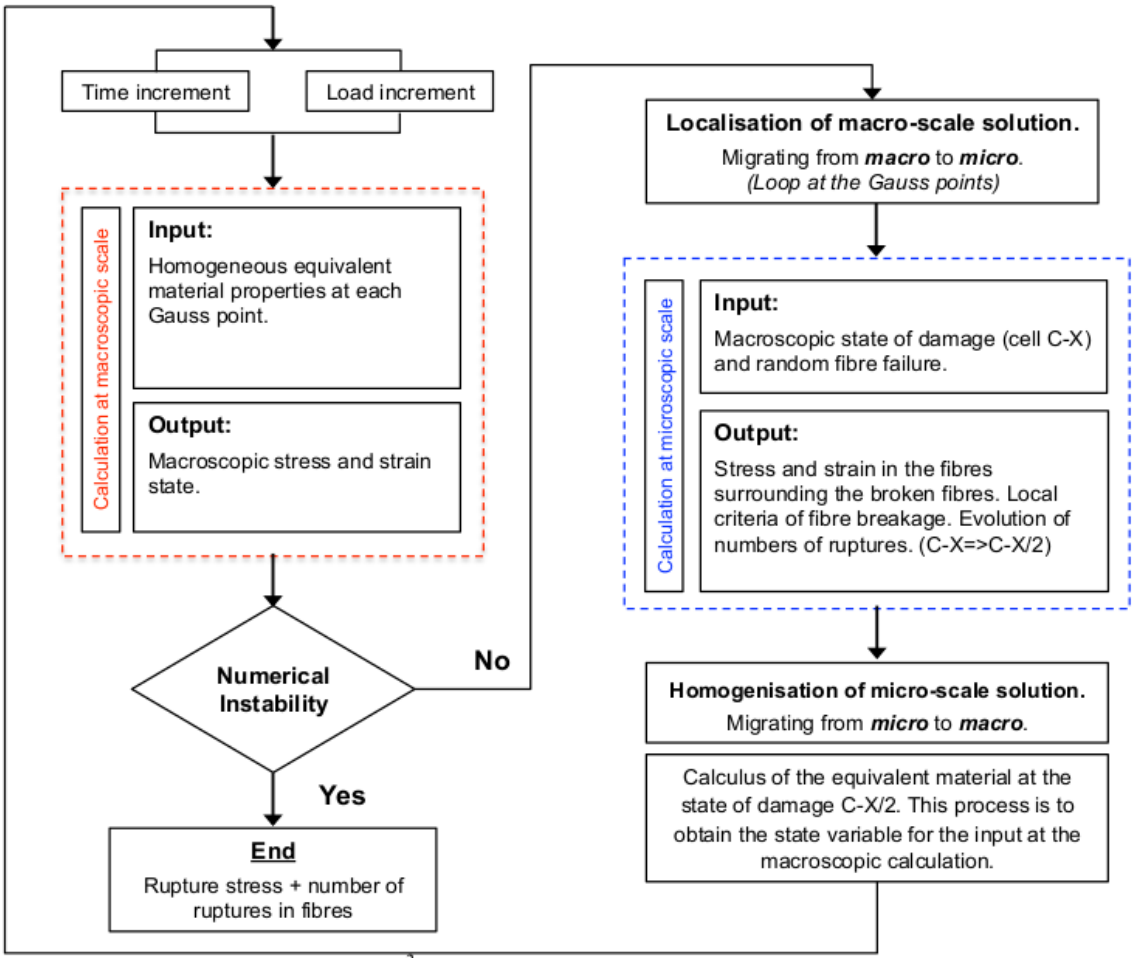

Figure 2.5: Flowchart of the MINES ParisTech fibre break model. Reproduced from: [26].

Localization and microscopic solution In the localization step, a transition is made from the macroscale to the micromechanical framework, defined at each Gauss point (RVE). At this stage, the material is treated as heterogeneous, with separate properties for fibres and matrix. The maximum stress in the fibres is evaluated using the precomputed values of the K_r^{max} coefficient stored in a database and compared against the condition:

$$\underbrace{\sigma^{macro} K_r^{max}}_{\sigma^{micro}} \geq \sigma_R, \tag{2.5}$$

where σ^{micro} is the maximum stress in the unbroken fibres, σ^{macro} is the macroscopic stress obtained from the macromechanical FEM solution and σ_R is the local fibre strength assigned at the beginning of the simulation. If the condition 2.5 is met, the damage state is updated from Cell C-X to Cell C-X/2. In practice, Cell C-32 is omitted and a step is made directly from the pristine state CS-32 to Cell C-16.

This reduces the computation time and has been shown to have a negligible effect on simulation results [154].

Homogenization The computed microscopic damage state is used to update the elastic properties of the homogenized material. Fibre breaks are assumed to only affect the longitudinal stiffness of the material. At each Gauss point, the component Q_{11} of the stiffness matrix is computed through the formula

$$Q_{11} = Q_{11}^0 \Big[1 - \frac{N_{fb}}{32}\Big], \tag{2.6}$$

where Q_{11}^0 is the value of the stiffness component for the pristine material and N_{fb} is the number of broken fibres in the RVE. The formula provides an upper bound for local stiffness reduction induced by fibre breaks, ensuring a conservative estimate of composite strength. After the macroscopic properties of the homogenized material are updated, the passage to the next time step can be made.

2.2.3 Example: tensile failure of a unidirectional specimen

The performance of the fibre break model is shown here on the example of a unidirectional tensile specimen with dimensions 64 mm × 4 mm × 1 mm, requiring a mesh of 3200 elements. No experimental reference is given here. The validation of the model against experimental results has been presented elsewhere, e.g. by Scott et al. [138]. The geometry of the specimen and the applied boundary conditions are illustrated in Figure 2.6. Axial load is applied to the nodes at each end of the specimen. The specimen is loaded in tension until failure at 0.2 MPa/s. While the size of the specimen is small compared to structural applications, it contains already approximately 13 000 fibres in the cross section. The solution of such a problem would be computationally challenging through a purely micromechanical approach.

Fibre strength values are generated from a Weibull distribution (Equation 1.2.2) with $\sigma_0 = 4.32\,\text{GPa}$ and $m = 5.62$, for a reference gauge length $L_0 = 25\,\text{mm}$. These values were obtained by Blassiau from experimental tests on T600S carbon fibres [9]. A uniform fibre volume fraction of 64 % is assigned in the entire specimen. The elastic coefficients of the unidirectional composite are summarized in Table 2.3.

Figure 2.7 shows the global stress-strain curve of the specimen and the evolution of the average number of fibre breaks in the RVEs. At first, the mechanical response of the material is linear. At low strains, almost no damage is registered. The number of fibre breaks starts growing rapidly as the strain increases, but even in the last iteration before failure there are on average less than 3 broken fibres per RVE. As a consequence, the stress-strain curve remains close to linear until late in

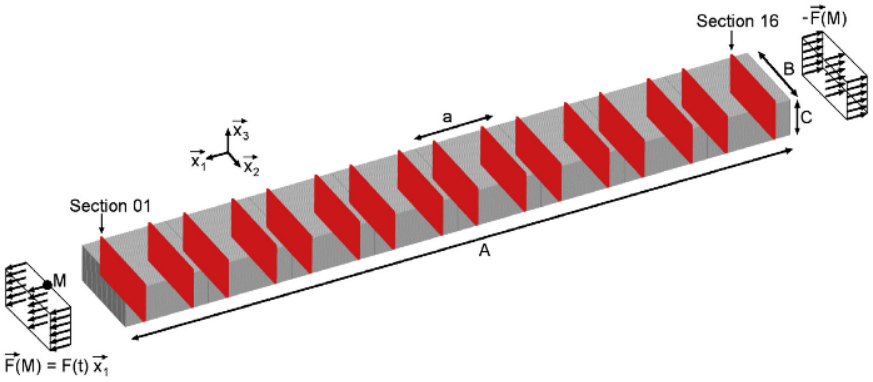

Figure 2.6: Fibre break model: geometry of a unidirectional specimen and boundary conditions. The dimensions A, B and C are equal to 64, 4 and 1 mm, respectively. The length of a C3D8 finite element a is equal to 8 mm. Image reproduced from [154].

E_{11}	E_{22}=E_{33}	$\nu_{12} = \nu_{13}$	ν_{23}	$G_{12} = G_{13}$	G_{23}
145.0 GPa	12.5 GPa	0.29 -	0.40 -	5.5 GPa	7.0 GPa

Table 2.3: Elastic properties of an undamaged UD ply for 64% fibre volume fraction.

the simulation. The failure occurs in a catastrophic fashion, manifesting through an abrupt increase in the average longitudinal strain.

Figure 2.8 shows the evolution of the number of i-plets as predicted by the model. Initially, a gradual increase in the number of 2-plets and 4-plets can be observed. 8-plets start appearing at a higher strain, but also show a stable growth until failure. 16-plets show a different behaviour. They are very unstable and usually turn into 32-plets in the next time step after their appearance. The moment of failure is marked by an abrupt increase in the number of 32-plets, in agreement with the catastrophic failure of composites observed experimentally.

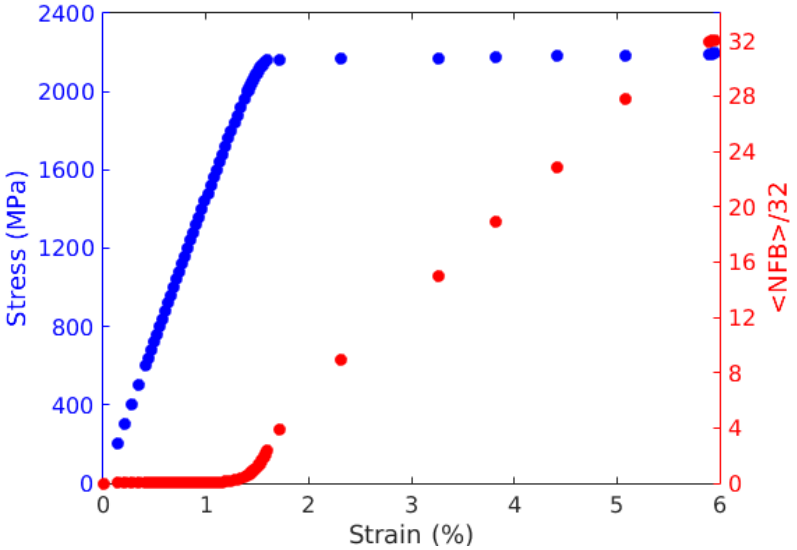

Figure 2.7: Fibre break model: the global stress strain curve and the average number of fibre breaks per RVE.

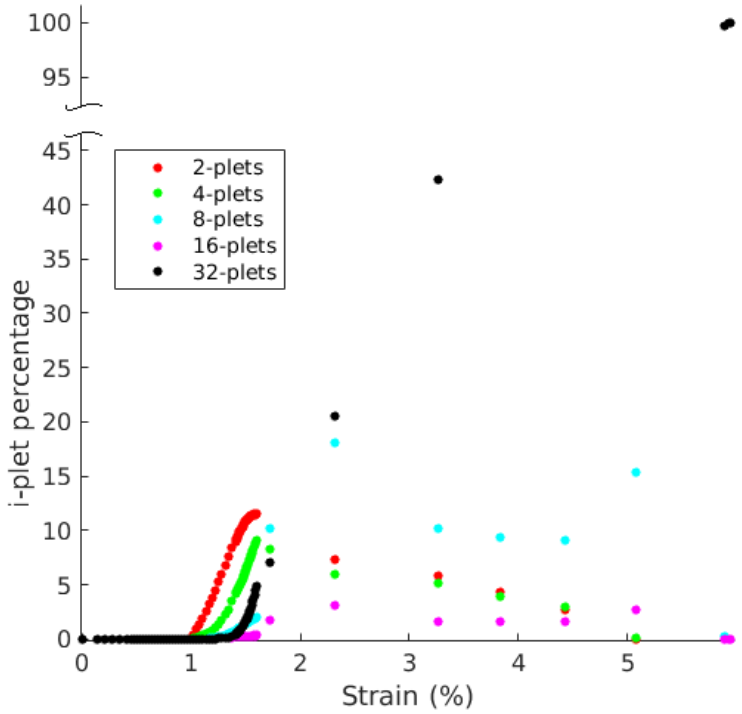

Figure 2.8: Fibre break model: evolution of i-plets. The y-axis shows the percentage of RVEs at a given i-plet state.

2.3 Factors unaccounted for in the existing modelling

As mentioned in Chapter 1, fibre breakage is the dominant damage mode in a pressure vessel. Therefore, the multiscale fibre break model of Blassiau et al. provides a suitable framework for simulating pressure vessel failure. It has shown a good agreement with experimental results of slow burst tests on composite pressure vessels [27]. While it is not possible to account for all possible factors present in the failure of a real-life material, critically evaluating the limitations stemming from the modelling choices is of great importance. This section presents selected factors that are not accounted for in the current modelling approach.

2.3.1 Validation of the three-dimensional RVE

A representative volume element (RVE) is a volume of a heterogeneous material whose apparent homogenized properties are representative of the bulk material [59]. This concept is essential for a multiscale modelling approach, serving as a link between the microscale and the macroscale of the material. In principle, the RVE size can be different for each studied property. Multiscale simulation of tensile failure in a unidirectional composite requires defining an RVE of the fibre break phenomenon. As mentioned in Section 2.2.1, the choice of RVE was made by extrapolating results of a study of tensile failure of a two-dimensional composite, carried out by Baxevanakis [2]. Confirming the validity of the 32-fibre RVE used by Blassiau et al. is necessary, in order to provide a solid base to the modelling approach. This problem is addressed in detail in Chapter 3.

2.3.2 Voids

Voids (cavities) present at different scales of a composite material are another important factor that is not often considered in modelling. Some amount of voids can be found in all composite structures. Void formation depends strongly on the manufacturing process and its parameters. It is possible to minimize their presence, but this increases significantly the price of the material and might not always be necessary.

From the point of view of fibre break modelling, the influence of voids on longitudinal tensile properties of UD composites is of special interest. Most existing research shows that axial properties of unidirectional composites are only moderately influenced by the presence of voids. Olivier et al. observed a decrease in longitudinal strength of a unidirectional composite with increasing void content and suggested that it could be caused by local fibre deformation around voids [113]. Liu et al. [89]

reported a significantly larger influence for a cross-ply laminate: for an increase in void content from 0.6 % to 3.2 %, tensile strength decreased by 14 %. Scott et al. observed a disproportionately high number of fibre breaks adjacent to voids in a unidirectional CFRP [137], although the overall tensile strength of the material was not affected. The effect of voids is known to be more severe in the transverse direction: Olivier et al. reported that an increase from 0 % to 10 % void content reduced the transverse tensile strength of a unidirectional CFRP by 30 % [113].

The mechanisms through which voids influence composite strength are not always well understood. At a basic level, voids might be seen as decreasing local fibre volume fraction, which is an important factor in composite strength. A possible mechanism affecting the tensile strength is the less effective load transfer between fibres near the voids [36]. Since part of the fibre adjacent to a void does not have any bond with the matrix (or very little), the recovery length of a broken fibre might be significantly increased. As a result, a broken fibre will affect a longer section of the neighbouring fibres, increasing the probability of a new break appearance.

Thick-walled filament-wound structures are known to show a high void content compared to composites obtained through other processes. An example of a carbon fibre cylinder cross-section with multiple voids visible is shown in Figure 2.9. The influence of these voids on pressure vessel strength is not fully understood and most numerical approaches ignore their presence. This problem will be addressed in the work presented in this thesis, using experimental and numerical techniques.

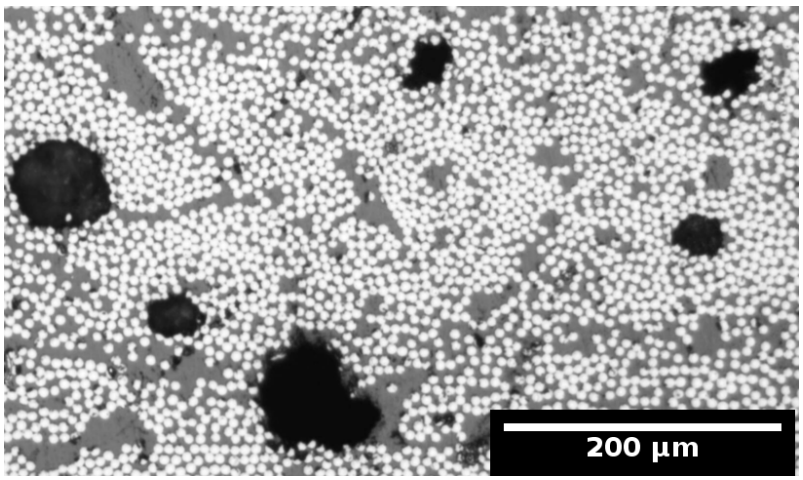

Figure 2.9: Optical microscopy of the microstructure of a carbon/epoxy pressure vessel with multiple voids visible.

2.3.3 Hygrothermal effects

Environmental factors, such as temperature, moisture and UV radiation can negatively influence the properties of composite materials. The risk of environmental degradation needs to be taken into account at the design stage and extreme operating conditions should be considered. In its lifetime, a composite structure can be exposed to conditions varying from cryogenic to elevated temperatures of several hundred degrees Celsius. Carbon fibres are generally temperature-insensitive in these conditions. By contrast, mechanical properties of polymer resins vary significantly with temperature. It is therefore the properties of the matrix that determine the temperature-dependent performance of a fibre-reinforced composite. Amorphous polymers, such as epoxy, exhibit a significant change in stiffness upon reaching the glass transition temperature T_g. Below this temperature, the polymer remains in a glassy state. At the atomic scale, this means that the polymer chains have little mobility. At values higher than T_g, the polymer transitions to a rubbery state. Polymer chains have more freedom to move past each other, which at the macroscale manifests through a lower stiffness.

Since the load transfer around fibre breaks is a function of matrix properties, tensile strength of the composite can be expected to depend on temperature [141] [178] [46]. Two competing mechanisms are at play. An earlier onset of plasticity reduces the maximum stress in fibres adjacent to a break, reducing the probability of a break appearance in the immediate vicinity of the previous one (co-planar break). At the same time, the ineffective length increases and the stresses are redistributed over a larger zone of the composite, increasing the probability of a new fibre break appearing farther away from the first one [105] [109] [3] [158].

Moisture affects mostly the matrix properties and it shows certain parallels to temperature influence. Therefore, the two factors are often grouped under the umbrella of hygrothermal effects. Similar to high temperature, moisture leads to a decrease in the yield stress of the matrix and can weaken the fibre-matrix interface [178] [25] [119]. Seawater has been shown to increase the moisture absorption rate, but the effect on mechanical properties is generally similar to that of distilled water [41] [144].

Hygrothermal effects can have a significant effect on the tensile strength of composites and on the mechanics of the damage accumulation. While the effects on the mechanical properties of the matrix are similar for moisture and temperature, there is a significant difference in the time scale between the two. It takes a long time before moisture penetrates through the thickness of the composite. Additionally, applying a protective coating can limit the penetration even further. Water absorption is therefore mostly relevant in marine applications, where composites can be exposed to high moisture for extended periods of time. In turn, temperature can exhibit variations at much shorter time scales. A composite structure can experience

a sudden temperature increase, e.g. in the event of a fire. Therefore, elevated temperature is a more important risk factor in predicting composite pressure vessel strength.

Modelling the influence of hygrothermal effects requires a detailed knowledge of matrix mechanical properties under a wide range of environmental conditions. This would require an extensive experimental campaign that does not enter into the scope of this thesis. Therefore, although the importance of moisture and temperature is realized, these factors are not addressed further in the work presented here.

2.4 Conclusions

The multiscale fibre break model introduced in this chapter is shown to be capable of simulating tensile failure of a longitudinally loaded unidirectional composite. It does it by taking into account fibre break accumulation occuring at the microscale. In this way, it establishes a link between the macroscopic structure response and the micromechanics of the fibre break process. It can be therefore used to simulate failure of composite pressure vessels that is principally caused by fibre breakage.

A critical evaluation of the model is carried out to identify unresolved issues and propose further developments. The choice of the representative volume element of the fibre break process is shown to need further validation, in order to provide a strong theoretical foundation to the multiscale model. This topic is addressed in Chapter 3.

Amongst factors not accounted for in the existing approach and relevant for simulating composite pressure vessel burst, void presence is selected as the phenomenon that requires further investigation. Filament-wound structures can often exhibit a high void content and its influence does not often receive appropriate attention. Therefore, voids and their effect at various scales of composite materials will be studied more closely in this thesis.

Chapter 3

Validation of the representative domain element of the fibre break phenomenon

Chapitre 3. Validation du domaine élémentaire représentatif du phénomène de rupture des fibres

L'extrapolation faite par Blassiau du volume élémentaire représentatif (VER) tridimensionnel d'un composite unidirectionnel, sans démonstration rigoureuse, doit être justifiée. Basée sur les concepts des fonctions aléatoires stationnaires ergodiques et de la portée intégrale (FASTEPI), une démarche systématique va permettre d'amener la preuve recherchée.

En tout premier lieu, les définitions de base nécessaires à la définition de la notion de propriété sont données. Ensuite on constate que les concepts FASTEPI permettent d'amener un cadre rigoureux à une démarche permettant de répondre positivement ou négativement au fait de pouvoir associer à une grandeur choisie le qualificatif de propriété.

En vue de la justification de l'extrapolation de Blassiau, ces concepts sont ainsi appliqués au cas de la valeur à rupture longitudinale d'un composite unidirectionnel. D'abord, on ré-examine les résultats bidimensionnels de Baxevanakis [2], à l'origine de cette extrapolation tridimensionnelle. Notamment, on s'inspire de ces travaux pour valider ou vérifier le fait que le cas tridimensionnel garde quelques similitudes avec eux : une modélisation construite sur la théorie du maillon le plus faible, la topologie des ruptures de fibres à l'état de rupture ainsi que le caractère poissonien du phénomène. Par contre, la longueur caractéristique du maillon est abandonnée : en effet, l'essai de multifragmentation qui l'a justifié dans le cadre bidimensionnel de Baxevanakis (0.5 mm), n'est pas représentatif dans un cadre qui place une fibre dans un environnement tridimensionnel. Ce sont les observations de Scott qui sont alors utilisées : la longueur caractéristique retenue est 0.1 mm [136].

Ensuite, on met en place la démarche des concepts FASTEPI pour le phénomène considéré, dans le cas tridimensionnel : la rupture longitudinale de différents domaines (taille et forme) formés de fibres unidirectionnelles est examinée d'un point de vue statistique.

Il ressort que la topologie des ruptures des fibres au sein de ces domaines est similaire au cas bidimensionnel pour l'état de rupture : toutes les fibres de ces domaines sont rompues une seule fois en moyenne, et en moyenne toutes localisées dans le même plan, pour des longueurs inférieures à 4 mm. Pour des longueurs supérieures, cette topologie se reproduit de manière périodique. Il ressort également que la variance des valeurs à rupture obéït bien à une proportionnalité inverse au volume du domaine.

Tout ceci permet de valider l'extrapolation de Blassiau : le domaine élémentaire représentatif du composite unidirectionnel est constitué de 36 fibres parallèles régulièrement réparties et pour une longueur de 4 mm.

Il convient de noter que la démarche permet de mettre en évidence que non seulement la taille (le volume) des domaines est importante mais aussi leur forme. Aussi, on abandonne désormais la dénomination de VER (volume élémentaire représentatif) au profit de celle de DER (domaine élémentaire représentatif) qui souligne l'importance de ces deux grandeurs dans la définition d'une propriété.

3.1 Introduction

As discussed in Chapter 2, the three-dimensional representative volume element (RVE) of the fibre break process used by Blassiau et al. [9] was not rigorously justified and was instead obtained by extrapolation of the two-dimensional RVE identified by Baxevanakis [2]. Since the RVE is an important component in the multiscale model, its size ought to be appropriately determined. In this chapter, this problem is addressed in a methodical way.

The concept of a representative volume element is important for modelling the effective properties of a heterogeneous material. The introduction of this concept is attributed to Hill [59]. Since then, several definitions have been proposed [53] [42]. In this chapter, an RVE is understood as a subvolume of the studied material that is sufficiently large to recover its effective properties, i.e. the properties measured at the macroscale.

Kanit et al. [77] have tied the RVE size of a random heterogeneous medium to the number of generated microstructures over which the effective properties are computed. This approach is based on the concept of the integral range [93] [87]. Initially applied to linear properties of the material, such as elastic coefficients and thermal conductivity, this method has been also extended to non-linear properties [128]. A similar statistical approach is adopted in the work presented here.

This chapter is structured as follows: first, the concepts used in the statistical approach are introduced. Then, the method of RVE size determination is explained. Next, the method is applied to the problem of longitudinal tensile failure of a unidirectional composite. The two-dimensional RVE of Baxevanakis is briefly discussed and analyzed from the point of view of the proposed statistical approach. Then, the RVE size for the three-dimensional case is identified. The topology of the fibre break process in the three-dimensional RVE is also analyzed.

3.2 Evaluation of a property using the concepts of a stationary ergodic random function (SERF) and integral range

3.2.1 Definition of a property

In this chapter, a material property is defined as a characteristic that is intensive, i.e. independent of the considered volume and independent of time. To evaluate this quantity, it is necessary to carry out measurements on one or more specimens.

These specimens constitute the measurement sample. Ideally, it would be desirable to carry out a single measurement on the total volume of the material existing in the universe, which would result in zero uncertainty. However, this is not possible and the measurements have to be performed on a finite number of smaller specimens. This introduces uncertainty into the measured value of the considered property. To ensure that the measurement is representative of the property, two conditions need to be satisfied [87]:

(i) spatial homogeneity, i.e. measurement results on several sufficiently large specimens are not significantly different
(ii) statistical inference, i.e. the possibility to evaluate unknown characteristics of a population from a single specimen of that population

3.2.2 Stationary ergodic random function (SERF)

A stationary ergodic random function (SERF) meets the two conditions introduced in the previous section and can thus represent a property. It provides a statistical framework for determining if a measurement (or a series of measurements) is representative of a material property.

First, let's assume that a certain material property is represented by a random stationary function $Z = (Z(x), x \in \mathbb{R}^d)$, with an unknown mean m and variance σ^2. The mean of this function in a volume V is defined as

$$m_Z(V) = \frac{1}{|V|} \int_{V_i} Z \mathrm{d}x. \tag{3.1}$$

For a large number of measurements N of this function in independent volumes V_i of size $|V|$, the experimental mean m_{exp} and experimental variance v_{exp} are defined:

$$m_{exp}(N, V) = \frac{1}{N} \sum_{i=1}^{N} m_Z(V_i), \tag{3.2a}$$

$$v_{exp}(N, V) = \frac{1}{N} \sum_{i=1}^{N} \left(m_z(V_i) - m_{exp}(N, V)\right)^2. \tag{3.2b}$$

The experimental mean and variance are estimators of the mean and variance of function Z in volume V:

$$\mathrm{E}\{m_Z(V)\} \approx m_{exp}(N, V), \tag{3.3a}$$

$$\mathrm{Var}\{m_Z(V)\} \approx v_{exp}(N, V). \tag{3.3b}$$

Equation 3.3b is true only if function Z is ergodic, i.e. if it satisfies the following condition:

$$\lim_{V \to \infty} \mathrm{Var}\{m_Z(V)\} = 0. \tag{3.4}$$

3.2.3 Integral range

The concept of the integral range will be now introduced [93] [94] [87] [73]. Provided that a property can be represented by a SERF, its mean can be estimated from a limited number of measurements. The concept of integral range can be used to evaluate the uncertainty of the measurement. The integral range I of a stationary ergodic random function Z is defined as

$$I = \lim_{V \to \infty} |V| \frac{\mathrm{Var}\{m_Z(V)\}}{\sigma^2}. \tag{3.5}$$

If this limit is finite and non-zero, then the following approximation is true for a large volume $|V| \gg I$:

$$I \approx |V| \frac{\mathrm{Var}\{m_Z(V)\}}{\sigma^2}. \tag{3.6}$$

By rearranging the terms, it can be written as

$$\mathrm{Var}\{m_Z(V)\} \approx \frac{\sigma^2 I}{|V|}. \tag{3.7}$$

Now, let's assume that the volume V is divided into k indepentent subdomains, such that $|V| = k|v|$ and $\infty > |V| \gg |v| \gg I > 0$. In that case, the experimental variance in the volume $|v|$ can be approximated by the expression

$$v_{exp}(k, v) \approx \frac{\sigma^2 I}{|v|}, \tag{3.8}$$

which can be further rewritten as

$$\log v_{exp}(k, v) = \log(\sigma^2 I) - \log |v|. \tag{3.9}$$

From the equation above, it can be concluded that if Z is a stationary ergodic random function and the integral range I exists and is finite and non-zero, then points $(\log |v|, \log v_{exp}(k, v))$ can be fitted to a linear regression with a slope equal to -1, for a large enough size of v. By this method, it can be verified whether experimental measurements are representative of a SERF.

3.2.4 Measurement uncertainty

Let's assume that N measurements of a certain stationary ergodic random function Z were performed. Each measurement was done in a volume v of size $|v|$. The experimental mean and variance of the sample m_{exp} and v_{exp} are defined

by Equation 3.2a and Equation 3.2b, respectively. The absolute and relative uncertainty of the measurement of the mean, ε^{abs} and ε^{rel}, are written as

$$\varepsilon^{abs} = K\frac{\sqrt{v_{exp}}}{\sqrt{N}}, \tag{3.10a}$$

$$\varepsilon^{rel} = \frac{\varepsilon^{abs}}{m_{exp}} = \frac{K}{m_{exp}}\frac{\sqrt{v_{exp}}}{\sqrt{N}}, \tag{3.10b}$$

where K is a t-value of the Student's distribution, dependent on the desired confidence interval [71]. Using Equation 3.8, the relative uncertainty can be written as

$$\varepsilon^{rel} = \sqrt{\frac{K^2\sigma^2 I}{m_{exp}^2 N|v|}}. \tag{3.11}$$

From the equation above, it can be seen that the uncertainty can be reduced by increasing the value of the product $N|v|$. This can be achieved either by taking more measurements or by increasing the volume in which they are performed. Let's assume that we want to know how many samples of size $|v|$ need to be tested to obtain a measurement error lower than ε_{max}^{rel}. To this end, Equation 3.11 can be rearranged to obtain the condition:

$$\frac{K^2\sigma^2 I}{m_{exp}^2|v|(\varepsilon_{max}^{rel})^2} < N^{min}. \tag{3.12}$$

Alternatively, the equation can be rewritten to find the minimum specimen volume for a given number of specimens N:

$$\frac{K^2\sigma^2 I}{m_{exp}^2 N(\varepsilon_{max}^{rel})^2} < |v|^{min}. \tag{3.13}$$

3.2.5 Shape of the measurement specimen

The concepts of a stationary ergodic random function and integral range, introduced above, provide a method of identifying and measuring a property. While the results depend on the volume of the specimens, the method does not take into account specimen length, width and height - or in other words its shape. It will be now shown that specimen shape can also influence the result.

Let's consider as a property the longitudinal tensile strength of a unidirectional fibre-reinforced carbon-epoxy composite. Let's construct families of parallelepipedic specimens, consisting of a single fibre embedded in matrix, like the one shown in Figure 3.1. The volume of the specimens in a given family is controlled by modifying the length of the fibre, while the cross-sectional dimensions remain constant. Specimen failure under tensile loading corresponds to the appearance

of the first fibre break. As discussed in Section 1.2, the probability of a fibre break appearance can be represented through the two-parameter Weibull distribution (Equation 1.2.2). The mean m_W and variance v_W of the Weibull distribution, written in terms of specimen volume V, are known to be equal to

$$m_W = \sigma_0 \left(\frac{V}{V_0}\right)^{-\frac{1}{m}} \Gamma\left(1+\frac{1}{m}\right) \tag{3.14}$$

and

$$v_W = \sigma_0^2 \left(\frac{V}{V_0}\right)^{-\frac{2}{m}} \left[\Gamma\left(1+\frac{2}{m}\right) - \Gamma^2\left(1+\frac{1}{m}\right)\right], \tag{3.15}$$

where Γ is the Gamma function. The last equation can be written as

$$v_W = \exp\left[-\frac{2}{m}\log V\right] \sigma_0^2 V_0^{\frac{2}{m}} \left[\Gamma\left(1+\frac{2}{m}\right) - \Gamma^2\left(1+\frac{1}{m}\right)\right]. \tag{3.16}$$

This expression allows us to quickly verify if tensile strength measured from this family of specimens represents a property of the composite. For k measurements of specimens of size $|v|$, the variance is

$$v_{exp}(k,v) = \exp\left[-\frac{2}{m}\log|v|\right] \sigma_0^2 V_0^{\frac{2}{m}} \left[\Gamma\left(1+\frac{2}{m}\right) - \Gamma^2\left(1+\frac{1}{m}\right)\right], \tag{3.17}$$

which can be written as

$$\log v_{exp}(k,v) = -\frac{2}{m}\log|v| + \log\left[\sigma_0^2 V_0^{\frac{2}{m}} \left[\Gamma\left(1+\frac{2}{m}\right) - \Gamma^2\left(1+\frac{1}{m}\right)\right]\right]. \tag{3.18}$$

Therefore, the slope of the curve $(\log|v_i|, \log v_{exp}(k,v_i))$ is equal to $-\frac{2}{m}$, which means that the measured strength does not represent a material property. This does not mean that tensile strength is not a property of the material. Instead, as will be shown below, an appropriate specimen shape needs to be selected in order to identify the property.

3.3 Determination of the representative domain element (RDE) for the longitudinal tensile strength of a unidirectional composite

The concepts introduced above will be now used to evaluate numerically the longitudinal tensile strength of a unidirectional composite and its corresponding representative domain element (RDE). The name RDE will be used here instead of RVE. This nomenclature is preferred to highlight the fact that we take into account

the shape of the specimen and not uniquely its volume. For practical reasons, only parallelepipedic specimens will be analyzed.

Let's consider an $\mathbb{R}^3$ Euclidean space with its associated orthonormal basis $(\vec{x_1}, \vec{x_2}, \vec{x_3})$. In this space, a parallelepipedic elementary domain A is defined, consisting of a section of a single fibre embedded in matrix and oriented along $\vec{x_1}$, as shown in Figure 3.1. To create parallelepipedic unidirectional composite specimens for the study of tensile strength, this domain is stacked along one or more directions $\vec{x}_i$, where $i = 1, 2, 3$. This allows building one, two or three-dimensional assemblies. An example of a one-dimensional assembly was the single fibre specimen considered in Section 3.2.5. Figure 3.2 presents schematically how a three-dimensional assembly is constructed. After defining all specimen shapes, numerical experiments will be performed in the framework of the finite element method to measure the tensile strength distribution of each specimen family. The simulations will take into account fibre strength variability, as discussed in Section 1.2.2. By using the framework of SERF and integral range, it is possible to determine whether the measured values are representative of a material property. The procedure of RDE determination consists of the following steps:

1. generate specimen families of different sizes and shapes by stacking the elementary domain A
2. carry out multiple simulations of tensile failure for each specimen family, each time for a new set of random fibre strength values
3. for each specimen family, compute the experimental mean and variance of the simulated tensile strength (Section 3.2.2)
4. verify if the measured values are representative of a property, by using the framework of SERF and integral range (Section 3.2.3)

3.4 Two-dimensional RDE

RDE size of the fibre break process was studied by Baxevanakis [2], although uniquely for a two-dimensional case. Since his results were used to justify the choice of RDE in the fibre break model of Blassiau et al., this study will be first discussed and analyzed here. The numerical study was preceded by an experimental campaign of fragmentation tests and single fibre tests on T300 carbon fibres. The relevant conclusions were:

- Stress at which a first fibre break appears in the fragmentation test shows a good agreement with fibre strength determined through single fibre tests.
- Fibre breaks in a fragmentation test are caused by flaws distributed according to a Poisson process.

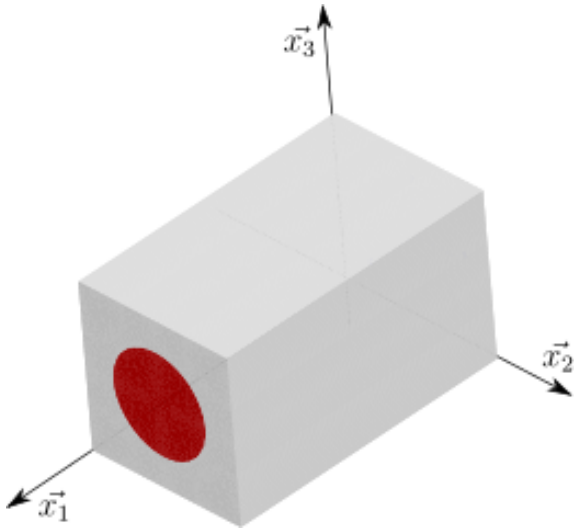

Figure 3.1: Elementary domain A for the tensile strength study. Fibre in red, matrix in grey. Fibre diameter is equal to 7 µm, fibre volume fraction $V_f = 60\%$.

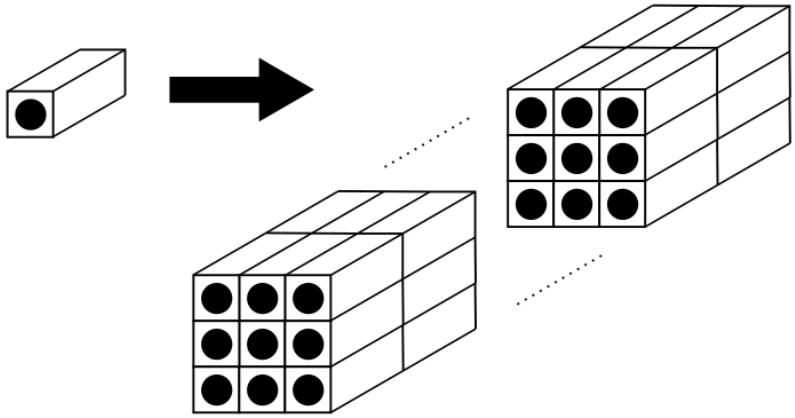

Figure 3.2: Construction of a 3×3 fibre assembly from a unit cell. The cells of 0.1 mm length are stacked longitudinally until a desired length is reached, e.g. 20 times for 2 mm.

- Fibre break occurrence in the fragmentation test follows a Poisson process far from saturation. Saturation is a state in which the increase in strain does not lead to the appearance of any new fibre breaks. For the fragmentation tests on T300 fibres, the average distance between fibre breaks at saturation was found to be $L_s = 0.5\,\text{mm}$.

Based on these observations it is concluded that the fibre strength can be modelled according to the weakest link model, with a link length of $L = L_s = 0.5\,\text{mm}$. As a result, a two-dimensional elementary domain A_{2D} is defined as a rectangle of length

$L_1 = L_s$ and width $L_2 \approx 0.01\,\text{mm}$, representing schematically a section of a fibre embedded in matrix, at a fibre volume fraction of 60%. The domain A_{2D} is shown in Figure 3.3. By stacking this elementary cell in the $\vec{x_1}$ and $\vec{x_2}$ directions, two-dimensional specimens are built, consisting of 3, 6, 8 and 12 fibres, with a length of 1.0 mm, 1.5 mm, 3.0 mm, 6.0 mm, 8.0 mm, 12.0 mm and 15.0 mm. As a result, a total of 28 different specimens families are obtained.

Finite element analysis of tensile strength is carried out for each specimen type. Each elementary domain A_{2D} inside the specimen has a failure strength assigned according to the experimentally measured fibre strength distribution. The finite element simulation is performed thirty times for each cell, each time with a new set of random strengths. For each set of thirty simulations, the mean, standard deviation and variance of tensile strength are calculated.

As the specimen dimensions increase, the mean and standard deviation values appear to converge to an asymptotic value. Not much change is observed for specimens larger than 6 fibres of 4 mm length and therefore these cells can be suspected to represent the RDE of the fibre break problem in two dimensions. However, by plotting the values of $(\log|v|, \log v_{exp})$, it can be seen that the slope of -1 characteristic of a property is only attained for the cells consisting of 12 fibres (Figure 3.4). The choice of the three-dimensional RDE made by Blassiau et al. was based on the results of Baxevanakis. If the RDE identified by Baxevanakis is not representative of a property, was its extrapolation to three dimensions a correct choice? This will be verified next.

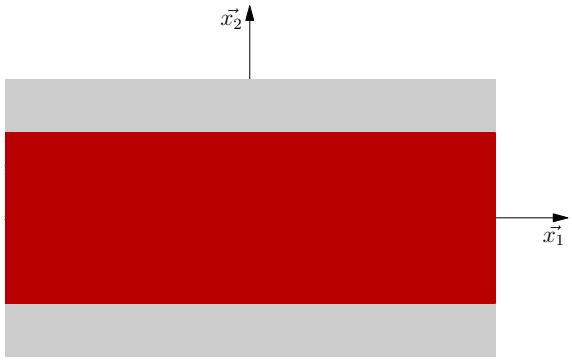

Figure 3.3: Elementary domain for the two-dimensional tensile strength study. Fibre in red, matrix in grey. Fibre radius is equal to 3.5 µm, fibre volume fraction $V_f = 60\%$.

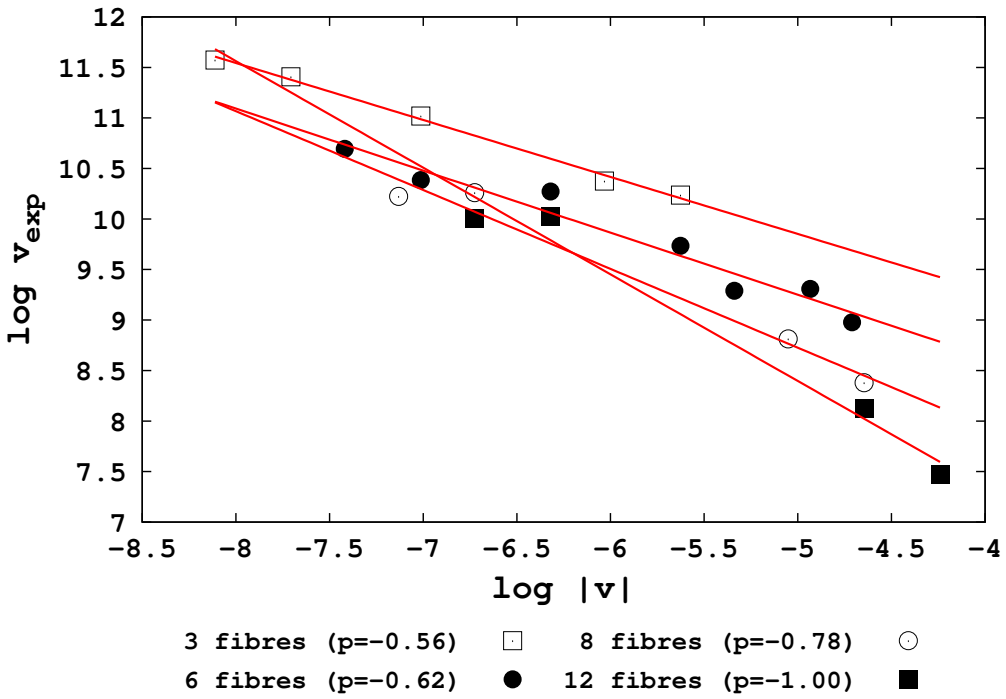

Figure 3.4: The values of $(\log|v|, \log v_{exp})$ are plotted for the fibre break process in two dimensions to verify if a given specimen geometry allows obtaining the value of the tensile strength property. This is true, if the slope p of the linear regression line is equal to -1. Here, this is achieved for 12 fibres.

3.5 Three-dimensional RDE

For the purpose of RDE identification in the three-dimensional case, a strategy analogous to that used by Baxevanakis is adopted. Certain modifications are made to the assumptions. The weakest link length of 0.5 mm obtained from the fragmentation tests overestimates the minimum distance between breaks on the same fibre in a three-dimensional composite. Based on synchrotron tomography results of Scott et al. [136], who observed distances between breaks as short as 70 µm, the weakest link length of 0.1 mm is selected instead. There is no method of directly measuring fibre strength at such a short gauge length. The strength is therefore assigned according to the bidimensional Weibull distribution, as proposed by Watanabe et al. for use at short gauge lengths [166]. For the T800S carbon fibres used in that study, the predicted strength distribution at gauge lengths shorter

than 1 mm can be closely approximated by a two-parameter Weibull distribution (Equation 1.2.2), with $m = 13.0$, $\sigma_0 = 8300\,\text{MPa}$ and $L_0 = 10\,\text{mm}$.

Taking into account the considerations mentioned above, an elementary parallelepipedic domain A_{3D} is defined, consisting of a single fibre of length 0.1 mm embedded in matrix. The fibre diameter is 7 µm and fibre volume fraction is equal to 60%. The finite element mesh of A_{3D} is shown in Figure 3.5. It consists of 136 three-dimensional linear eight-node elements (C3D8). Both fibres and matrix are assigned a linear elastic isotropic material behaviour, with the fibre modulus $E_f = 294\,\text{GPa}$, corresponding to that of T800S fibres used in the aforementioned study by Watanabe [166], and a matrix modulus $E_m = 3.9\,\text{GPa}$. For both materials, a Poisson's ratio of 0.3 is assigned. While in reality fibres can be anisotropic, this has a negligible influence on their behaviour in axial tension, justifying the isotropic material assumption. A fibre failure criterion is implemented. When the longitudinal stress in a fibre finite element reaches the previously assigned strength value, it breaks. Numerically, the properties of the element are replaced by those of the matrix. The failure of the fibre elements in a given elementary domain A_{3D} represents one fibre break.

The three-dimensional parallelepipedic specimens are assembled always keeping the same number of fibres $n = n_2 = n_3$ along directions $\vec{x_2}$ and $\vec{x_3}$. Values of $n = 1, 2, 3, ..., 7$ are used. n_1 elementary domains of length 0.1 mm are stacked along the direction $\vec{x_1}$ to obtain a given length. The tested lengths are 2.0 mm, 4.0 mm, 6.0 mm and 8.0 mm. In total, 27 specimen families are obtained. Fifty simulations are carried out for each geometry, with a new set of random local fibre strengths assigned each time. Periodic boundary conditions are applied in all three Cartesian directions. A monotonically increasing tensile loading is applied in the longitudinal direction. The size of the time step can vary, with larger time steps in the beginning of the simulation, where few fibre breaks occur. Close to failure, the applied stress is increased by no more than 10 MPa in each time step.

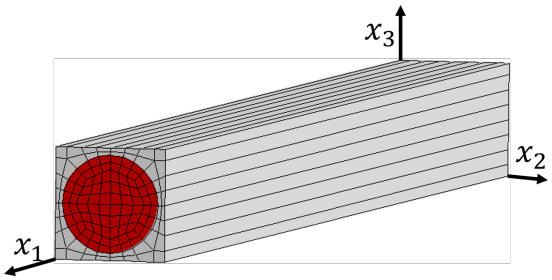

Figure 3.5: Finite element mesh of an elementary cell used to construct three-dimensional cells for validation of RVE size in three dimensions. Fibre depicted in red, grey elements correspond to the surrounding matrix. The length of the cell is 0.1 mm and the fibre volume fractions is 60%, for a fibre diameter of 7 µm.

3.5.1 Fibre break process in the three-dimensional RDE

For the purposes of this analysis, failure is defined as the moment in which the composite is split into two parts. It is not always straightforward to capture this moment in the numerical simulation, due to the random and unstable character of the fibre break process. However, the lower and upper bounds of the failure phenomenon can be easily recognized. In each simulation, the first time step in which all fibre elements are broken can be identified. This non-physical state constitutes an upper bound of the failure phenomenon. In the time step directly before that state is reached, two configurations can be identified:

(i) There exists a section of the domain perpendicular to the fibre direction in which all fibre elements are broken. This represents the moment of failure. Depending on the length of the domain, the number of broken section changes:
   - A single broken section is present for domain lengths of 2 mm and 4 mm.
   - For lengths of 6 mm and 8 mm, two broken sections are present and the number of breaks per fibre is approximately two times higher than in the case above.

(ii) There exists no section in which all fibres are broken, but there are sections in which a high percentage of fibres is broken (over 25%), indicating damage localization. This represents a lower bound for the failure phenomenon. The number of these sections is different depending on the domain length:
   - For 2 mm and 4 mm, there is one section with an elevated number of fibre breaks.
   - For 6 mm and 8 mm, there are two such sections.

A more refined time step would allow reaching a state in which failure propagates through the entire section, as described for Case (i). In terms of the average longitudinal stress in the domain, there is little difference between the two cases. Therefore, this lower bound state is identified as representing failure in the numerical simulation. From the information above, the following general conclusions on the topology of the fibre break process in a three-dimensional domain can be drawn:

- Failure coincides with the appearance of a plane perpendicular to the fibre orientation, in which all fibres are broken.
- At this point, most fibres are only broken once or twice.
- The points above are true for a domain of length 2 mm or 4 mm. For longer domains, the fibre break localization happens in two planes along the axis of the domain.

These results are illustrated on the example of the 6×6 fibre domain in Table 3.1, Figure 3.6 and Figure 3.7. The conclusions discussed above are important for

determining the SERF associated with the fibre break phenomenon. Namely, due to the different nature of the damage accumulation process, it is necessary to consider separately the results on domains of length 2 mm and 4 mm and then those obtained on domains of length 6 mm and 8 mm.

L(mm)	Mean	Std. dev.
2.0	1.49	0.176
4.0	1.64	0.370
6.0	2.76	0.423
8.0	2.50	0.258

Table 3.1: 6×6 fibre domain. Number of breaks per fibre at failure, based on the analysis of five simulations.

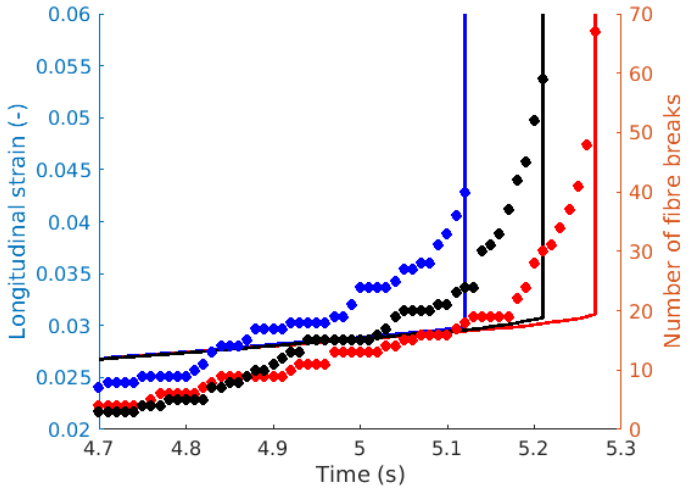

Figure 3.6: Case of 6×6 fibres, 4 mm length. Evolution of the number of fibre breaks (points) and average longitudinal strain (solid lines). Each color corresponds to a single simulation. The fibre breaks start appearing at a late stage and their number increases rapidly shortly prior to failure.

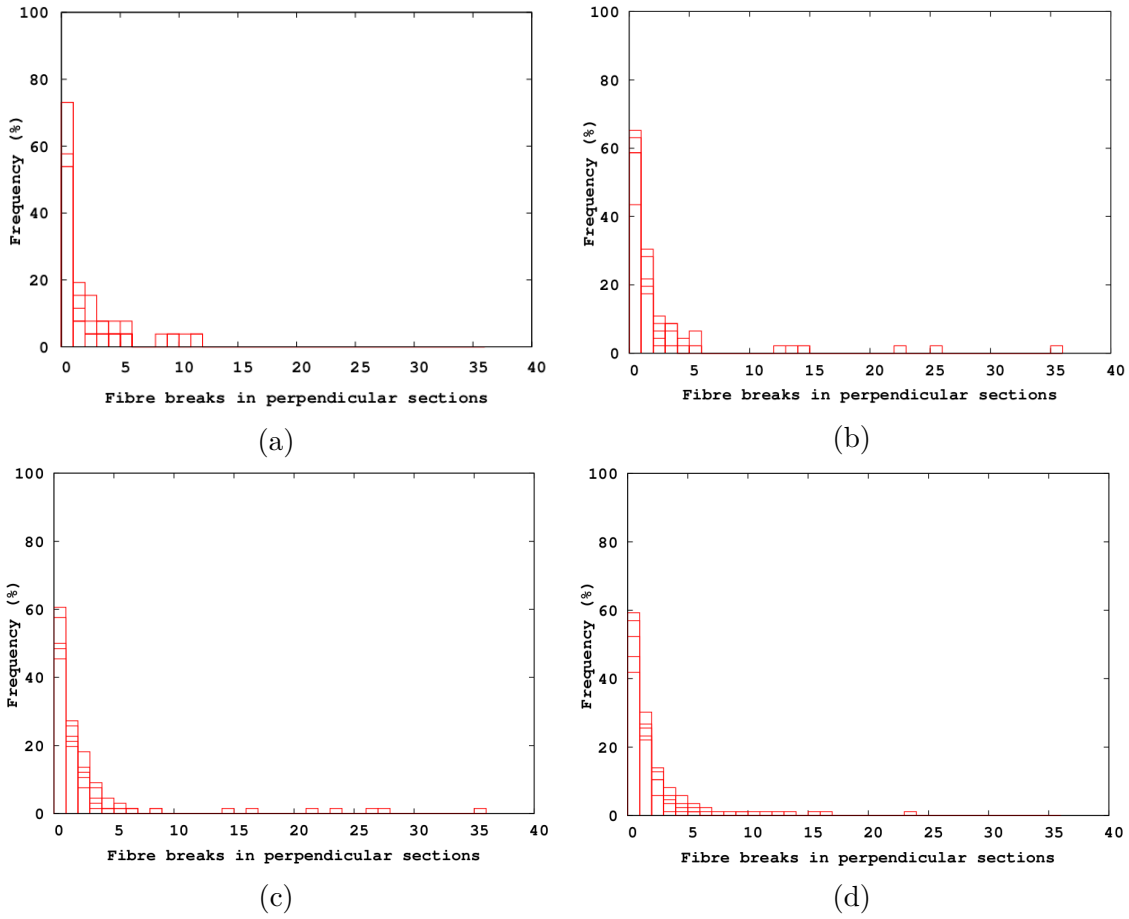

Figure 3.7: Case of 6×6 fibres. Histograms of the number of fibre breaks in perpendicular sections at the time step before reaching failure in the whole domain. For each length, five simulations are analyzed. Each figure is a superposition of five histograms. (a) Length 2 mm. For this length, a lower bound of the failure state is observed. No section is completely broken, but for each simulation there is one where approximately 10 fibre breaks are observed. Other sections are mostly intact. (b) Length 4 mm. In four cases, the lower failure bound is observed, for which there are between 15 and 25 fibre broken in a single section. In one case, the failure state is captured: all 36 fibres are broken in a single section, while other sections are mostly intact. (c) Length 6 mm and (d) 8 mm. In these two last cases, there are between 10 and 36 fibre breaks in two sections. Other sections are mostly intact.

3.5.2 Validation of a three-dimensional RDE through identifying the associated SERF

As a final step, it will be verified whether it is possible to identify a SERF describing the longitudinal strength of the 2 mm and 4 mm domains. In order to do this, the experimental variance of longitudinal strength obtained from numerical experiments on these domains will be analyzed, as summarized in Tables 3.2 and 3.3.

To verify whether the numerical experiment results are representative of a SERF, the points $(\log|v|, \log v_{exp})$ are plotted, as shown in Figure 3.9. As explained in the previous section, the main focus is on the domains of length 2 mm and 4 mm. For these cases, shown in Figure 3.9a, the linear regression has a slope of approximately -1. It is concluded that a SERF can be associated with the fibre break process phenomenon in these domains. It is worth noting that if the domains of lengths 6 mm and 8 mm are included in the analysis, as shown in Figure 3.8, the slope has a value of -1.17, significantly different from the value of -1 expected for a SERF. Therefore, the fibre break topology analysis described in the last section is of fundamental importance.

Finally, if a standard deviation of 1% is chosen, it can be concluded that a domain of 6×6 fibres and 4 mm length can represent a RDE of the fibre break process in three dimensions. This means that the choice of RDE done by Blassiau et al. is valid.

3.6 Conclusions

In this chapter, a mathematical framework has been proposed for identifying a representative domain element (RDE) of the fibre break process. The term RDE was introduced instead of RVE (representative volume element), to highlight the importance of shape in the definition of a representative volume. The selected approach is based on the concepts of a stationary ergodic random function (SERF) and integral range. After introducing the relevant concepts, an example of a single fibre failure is discussed to highlight the importance of cell shape in the choice of an RVE.

In the second part of the chapter, numerical experiments of longitudinal tensile failure are discussed. Tensile failure of a carbon-epoxy unidirectional composite is simulated in domains with a varying number of fibres and length. The mathematical framework introduced earlier is used to identify the representative domain element of fibre-dominated tensile failure. Additionally, the topology of fibre break process in the different domains is discussed. It is concluded that for the studied material, failure occurs through an accumulation of fibre breaks in a plane perpendicular

to the fibre direction (damage localization). For cells longer than 4 mm, damage localization is observed in two planes. Based on the numerical experiments, a cell of 6×6 fibres and 4 mm length is considered to be an appropriate RDE of the fibre break process.

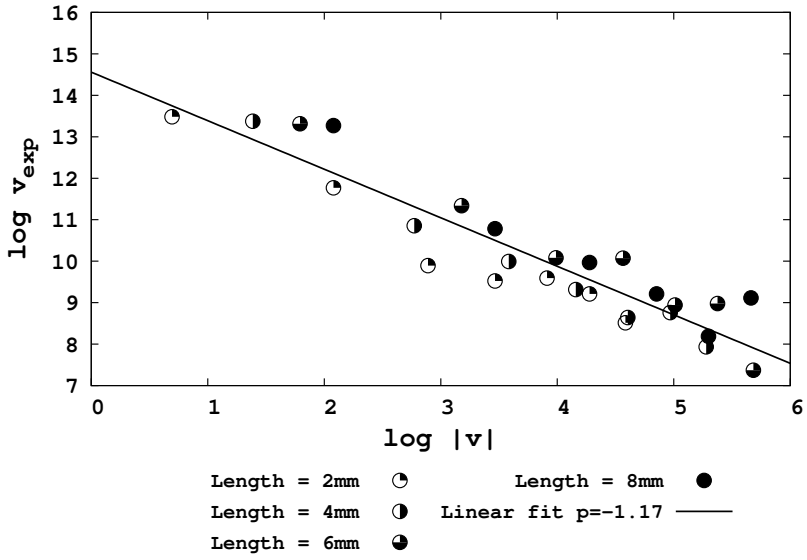

(a)

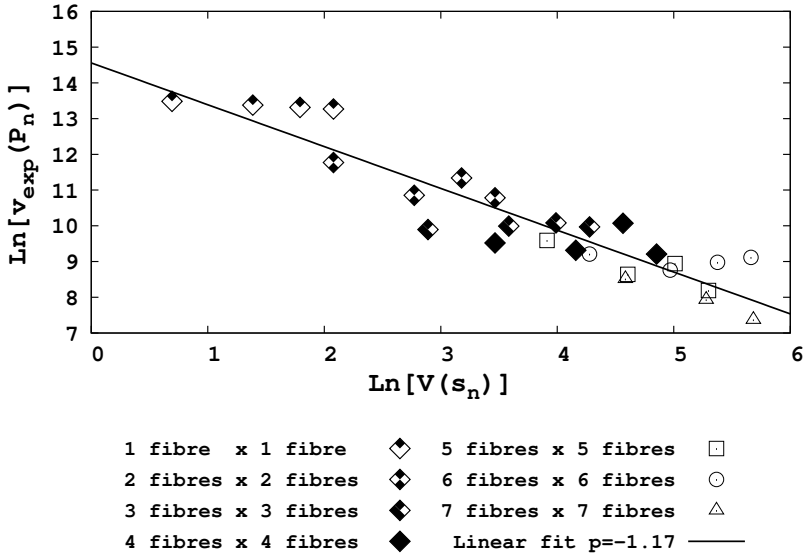

(b)

Figure 3.8: Data points $(\log|v|, \log v_{exp})$ and a linear regression for all studied domains. All results are used for the linear regression fit, while the failure phenomenon is different between cells of different lengths. As a result, the slope of the regression line is significantly different from -1, which might lead to the conclusion that it does not represent a SERF. Results need to be sorted by length, as done in Figure 3.9.

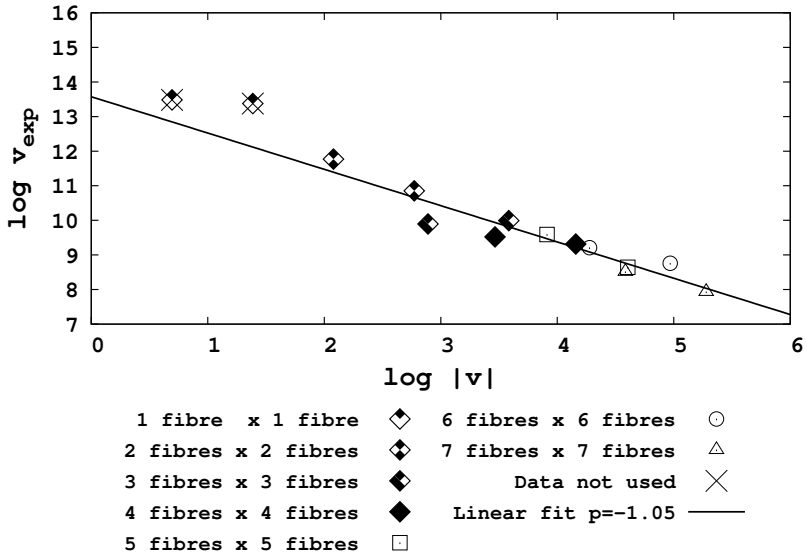

(a)

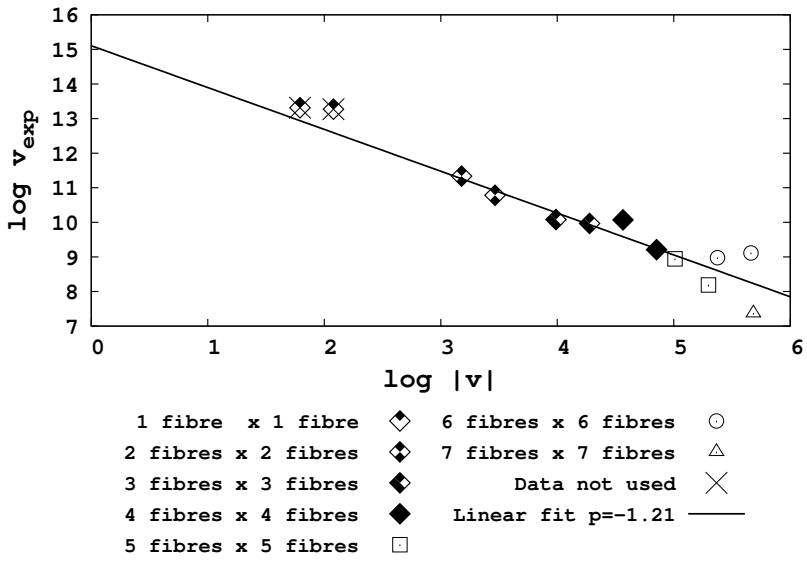

(b)

Figure 3.9: Data points $(\log|v|, \log v_{exp})$ and a linear regression sorted by domain length: a) 2 mm and 4 mm, b) 6 mm and 8 mm.

Length	Mean and std. dev. (MPa)	1 fibre × 1 fibre $n = 1$	2 fibres × 2 fibres $n = 2$	3 fibres × 3 fibres $n = 3$	4 fibres × 4 fibres $n = 4$	5 fibres × 5 fibres $n = 5$	6 fibres × 6 fibres $n = 6$	7 fibres × 7 fibres $n = 7$
2.0 mm	m_{exp}	9028	4994	5190	5218	5228	5265	5273
$n_1 = 20$	e_{exp}	846	359	140	116	120	82	70
4.0 mm	m_{exp}	8559	5028	5086	5149	5213	5208	5238
$n_1 = 40$	e_{exp}	802	227	147	105	75	67	52
6.0 mm	m_{exp}	8296	4832	5020	5109	5185	5244	5220
$n_1 = 60$	e_{exp}	778	289	154	153	87	80	39
8.0 mm	m_{exp}	8115	4826	4991	5072	5150	5215	
$n_1 = 80$	e_{exp}	761	219	146	99	60	45	

Table 3.2: Summary of the tensile strength results obtained from the numerical experiments on $N = 27$ domains. The mean and standard deviation values are obtained from fifty experiments for each specimen family.

Length	Mean and std. dev. (normalized)	1 fibre × 1 fibre $n = 1$	2 fibres × 2 fibres $n = 2$	3 fibres × 3 fibres $n = 3$	4 fibres × 4 fibres $n = 4$	5 fibres × 5 fibres $n = 5$	6 fibres × 6 fibres $n = 6$	7 fibres × 7 fibres $n = 7$
2.0 mm	m^0_{exp}	0.76329	0.42222	0.43883	0.44117	0.44200	0.44513	0.44583
$n_1 = 20$	e^0_{exp}	0.07158	0.03041	0.01190	0.00988	0.01023	0.00697	0.00597
4.0 mm	m^0_{exp}	0.72365	0.42513	0.43007	0.43536	0.44075	0.44039	0.44289
$n_1 = 40$	e^0_{exp}	0.06787	0.01923	0.01249	0.00891	0.00636	0.00568	0.00447
6.0 mm	m^0_{exp}	0.70144	0.40856	0.42444	0.43199	0.43837	0.44340	0.44138
$n_1 = 60$	e^0_{exp}	0.06578	0.02448	0.01307	0.01301	0.00740	0.00681	0.00337
8.0 mm	m^0_{exp}	0.68608	0.40802	0.42203	0.42881	0.43543	0.44094	
$n_1 = 80$	e^0_{exp}	0.06434	0.01856	0.01235	0.00845	0.00507	0.00384	

Table 3.3: Summary of the tensile strength results. The values from Table 3.2 are here normalized by $\Sigma_0 = 11\,828\,\text{MPa}$. Σ_0 is the scale factor of the input Weibull distribution, recalculated for a new gauge length $L_0 = 0.1\,\text{mm}$, equal to the length of the elementary domain A_{3D}. From the properties of the Weibull distribution, Σ_0 is the stress at which 63.2% of the elementary domains will fail [150].

Chapter 4

Void characterization in a thick-walled carbon-epoxy pressure vessel

Chapitre 4. Caractérisation de la porosité dans un réservoir carbone-époxy à parois épaisses

Afin d'étudier l'influence des porosités sur le comportement mécanique des réservoirs à haute pression, une bonne connaissance des caractéristiques de ces porosités est requise. Dans ce chapitre, des observations expérimentales sur un réservoir carbone-époxy à parois épaisses destiné au stockage d'hydrogène sont menées. Les porosités sont caractérisées à l'aide de la tomographie à rayons X et de la microscopie optique. Dans un premier temps, les différentes méthodes de caractérisation des porosités sont discutées. En suite, les procédures expérimentales utilisées pour obtenir les images microscopiques et les volumes tomographiques sont exposées, ainsi que les algorithmes de traitement d'image utilisés.

Les scans tomographiques permettent une caractérisation tridimensionnelle des porosités individuelles. Un grand nombre des grosses cavités macroscopiques est visible, localisées surtout à l'interface des couches composites à différentes orientations. Les porosités localisées au sein d'un pli ont typiquement la forme d'une aiguille, fortement allongée dans le sens des fibres. C'est le type des cavités trouvé le plus fréquemment dans les plis circonférentiels, qui contrôlent la résistance du réservoir. Les dimensions transversales de ces cavités peuvent varier entre quelques micromètres jusqu'à un ordre de grandeur de 1 mm.

La fraction volumique des cavités est estimée à partir des volumes tomographiques. Le taux des cavités mesuré est égal à 2,4 %. Les porosités ne sont pas distribuées d'une manière uniforme. On observe un gradient significatif de la fraction volumique dans le sens de l'épaisseur de la parois, avec les valeurs les moins élevées à proximité de la surface interne du réservoir.

Un algorithme est utilisé afin d'analyser la taille, la forme et l'orientation des cavités dans les volumes tomographiques. Plus de 135 000 cavités sont identifiées dans un seul volume de $26\,\text{mm} \times 21\,\text{mm} \times 17\,\text{mm}$. Les petites porosités sont beaucoup plus fréquentes, alors que les grosses cavités sont responsables pour la majorité de la fraction volumique totale. L'analyse de la morphologie des porosités montre que la plupart des celles-ci sont effectivement fortement allongées ; elles suivent l'orientation des fibres. Par contre, aucune corrélation claire n'apparaît entre la fraction volumique de la porosité et l'orientation du composite.

4.1 Introduction

Filament-wound composite pressure vessels are known to sometimes contain significant void volume fractions in comparison with structures manufactured through other methods. As discussed in Section 2.3.2, the existing studies show some influence of void content on the mechanical properties of fibre-reinforced composites. However, the influence of voids on the structural strength of pressure vessels is not thoroughly understood and requires further investigation.

In order to study void influence in pressure vessels, accurate knowledge of their characteristics is required. In this chapter, voids are analyzed in a thick-walled cylinder, i.e. one with a significant wall-thickness-to-radius ratio. The experimental observations are carried out on a filament-wound carbon-epoxy pressure vessel for hydrogen storage. The 40-litre cylinder supplied by Luxfer Gas Cylinders Ltd is shown in Figure 4.1. The service pressure of the cylinder is 700 bar. The weight of the pressure vessel is 54 kg, with a 330 mm external diameter and a length of 920 mm.

Figure 4.1: The carbon-epoxy pressure vessel inside a tomograph.

In the work presented here, voids in the pressure vessel are characterized using optical microscopy and X-ray computed tomography. First, a brief overview of the existing characterization methods is provided. The advantages of microscopy and tomography with respect to other techniques are explained. Next, an algorithm is introduced, developed to measure composite orientation from the tomography results. Digital image processing is carried out in Fiji software [134]. Finally, void characterization results are presented, including void content, as well as size and shape of individual cavities. Orientation measurement results are used to study correlation between void properties and the orientation of the surrounding composite material. The experimental observations provide information on the morphology of voids found in composite pressure vessels. The results help analyzing the influence of voids on the tensile strength of carbon fibre composites, which is studied further in later chapters.

4.2 Void characterization methods

The results of void characterization depend on the selected method and, for optical methods, also on the resolution at which the observations are carried out. In addition to voids with dimensions significantly larger than fibre diameter, there exist microscopic voids of size in the order of 1 µm or smaller. There exist multiple methods of void characterization in composite materials, such as: density measurement [40] [156], ultrasonic inspection [147] [66] [72] [104], microscopy [80] [127] [13] and X-ray tomography [88] [107] [90] [176] [145]. An extensive review of the state of the art of the various methods has been provided by Mehdikhani et al. [97]. Not all methods mentioned above provide the same type of information. For instance, the only output of the density measurement is the average void volume fraction in the sample. Ultrasonic inspection does provide information about void distribution in the composite plane, but cannot distinguish individual voids in the through-thickness direction. The advantage of the last two methods, microscopy and tomography, lies in the ability to characterize the features of individual voids: location, size and shape. The shortcoming of microscopy is the fact that the studied three-dimensional property, i.e. void fraction, is evaluated from two-dimensional data [51]. Furthermore, cutting the specimen and time-consuming polishing are typically required. X-ray tomography is the most accurate among the available methods, providing a fully three-dimensional description of void characteristics [88]. It allows a detailed analysis of void size, shape and orientation [56] [57] [96]. However, scans are costly and are usually limited to small samples, thereby providing only local information. This might be a problem if a large variation in void characteristics is present between different regions of the material.

In this chapter, both optical microscopy and X-ray tomography are used to

characterize void content in the studied pressure vessel. A succinct presentation of the applied image processing algorithms is also included. A detailed discussion of the image processing methods is outside the scope of this thesis and can be found in reference works, e.g. by Nixon [108].

4.2.1 Optical microscopy

Optical microscopy observations are carried out on a polished specimen cut out from the cylindrical section of the pressure vessel. The observed face of the specimen is perpendicular to the hoop direction and spans the complete wall thickness. In order to characterize the through-thickness void distribution, a 2 mm wide band of the material is mapped at 50× magnification. The pixel size of the digital micrographs is 670 nm. In addition to void fraction, the micrographs also allow evaluating the fibre volume fraction, as discussed in Appendix A.

To simplify image processing, the RGB micrographs are transformed to 8-bit grayscale, so that each pixel of the micrograph is represented by a grayscale intensity value from 0 (black) to 255 (white). Void segmentation is carried out by global grayscale thresholding. The threshold value is determined by Otsu's method [115]. The quality of thresholding depends on surface preparation and illumination. For the micrographs obtained in this study, an image processing algorithm is implemented in Fiji and applied prior to thresholding in order to reduce the effect of non-uniform illumination. To this end, an average "background" image is created. First, an average intensity Z-projection is obtained for all images A Gaussian averaging operator with a radius of 200 pixels is applied to this image. The grayscale values of the resultant image are shifted, so that the minimum grayscale value is equal to zero. By subtracting the grayscale values of the resultant "background" image from an original micrograph, the non-homogeneous illumination effect is reduced.

4.2.2 X-ray micro-computed tomography

X-ray micro-computed tomography (µCT) is an experimental technique that allows imaging the internal microstructure of a scanned object in three dimensions at sub-micron resolutions. It is generally non-destructive and typically requires little specimen preparation [86]. The technique has its roots in Computerized Axial Tomography (CAT), commonly used in medical diagnostics. A CAT scan produces a two-dimensional projection (radiograph) of the observed object. An X-ray beam is sent through the object and is then detected by a photodetector. The amount of absorbed X-ray radiation depends on the atomic number (Z) of the scanned material: materials with a higher Z are more absorbant, resulting in a lower intensity of the

detected beam. The beam intensity is translated into a grayscale image of the scanned object that can be then interpreted by the user.

The principle of µCT is an extension of CAT to three dimensions. In order to create a three-dimensional representation of the scanned object, multiple radiographs are taken while the object is being rotated around a single axis. An inverse Radon transform is then used to produce a three-dimensional image reconstruction from the radiographs. This allows characterizing different phases present in the material as well as features such as void or cracks. The reconstructed volume consists of voxels. A voxel is a three-dimensional counterpart of a pixel and its size is defined by its edge length. For instance, a voxel of size 20 µm is a cube of dimensions 20 µm × 20 µm × 20 µm.

The tomography scans used in this study were obtained at the µ-Vis X-Ray Imaging Centre of the University of Southampton. The images were obtained using a custom-designed dual source high-energy micro-focus CT machine. At first, the whole cylindrical portion of the pressure vessel was scanned at a 97 µm voxel size. The large size of the structure presented a technical challenge. In order to fit the whole diameter of the cylinder inside the field of view, a panel shifting procedure was used. Along the axis, six volumes were imaged to cover the whole length of the cylindrical section. The six tomography volumes were concatenated in Fiji. The grayscale levels were calibrated between the volumes to avoid a mismatch at volume boundaries. Next, a polar transformation was applied to the images, in order to align composite plies in plane.

The resolution of the overview scan is sufficient to characterize only the largest voids. In order to characterize smaller voids, four additional scans were carried out on smaller specimens cut out from the cylinder. The approximate dimensions of the imaged specimens were 20 mm × 20 mm × 25 mm, spanning the complete wall thickness of the cylinder. The resultant tomography volumes had a voxel size of 20 µm.

The characterization of voids in the pressure vessel presents a challenge due to the large size of the studied structure and a large range of void dimensions (from sub-micron to multiple centimetres). A segmentation procedure is applied to the grayscale volumes in order to identify the voids. The segmentation is carried out using an image analysis algorithm identifying voids as local minima of the grayscale distribution [8]. The segmented binary images were visually compared with the original volumes and a generally good quality of the segmentation process was observed.

A particle analysis algorithm is applied to the binary images in order to classify individual voids. This allows measuring the properties of each void, such as its volume, bounding box dimensions and the position of its centroid. For each void, an inertia ellipsoid is constructed, i.e. an ellipsoid with the same moments of inertia

around the centroid as those of the void. From now on, whenever the orientation of a void is mentioned, it refers the orientation of the major axis of its inertia ellipsoid.

4.3 Composite orientation measurement

Void fraction in filament-wound structures has been reported to be correlated with ply orientation [33] [120]. Therefore, the orientation of the surrounding material is an important parameter to consider when performing void characterization. To measure ply orientation from the tomography volumes, an image analysis algorithm was developed for the purposes of this study and implemented in Matlab and Fiji. The approach is based on the two-dimensional Fast Fourier Transform (FFT), often applied to evaluate average material orientation [124] [49] [92] [81].

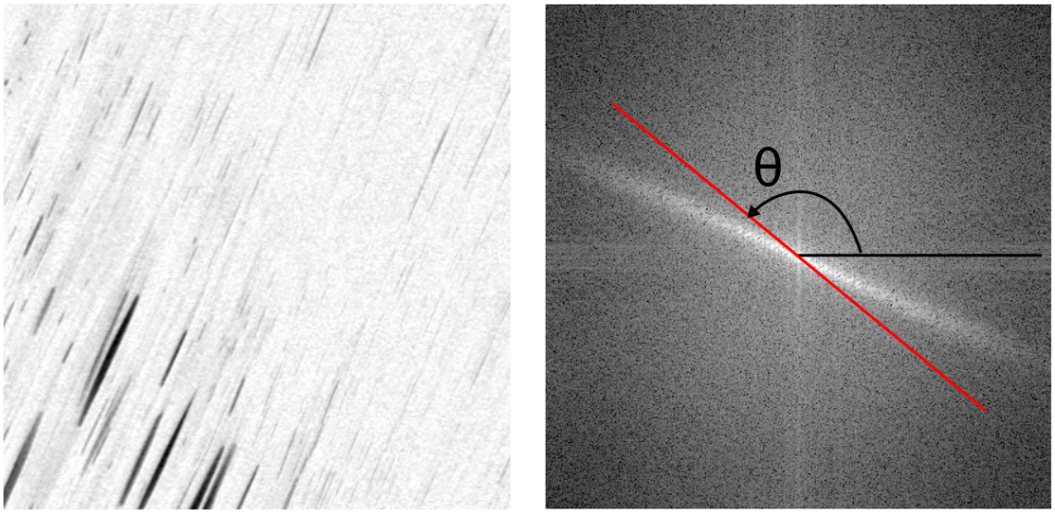

(a) Input image for computing local orientation.

(b) Power spectrum of the fast Fourier transform of the original image. The sum of pixel intensity is calculated along the red line for θ from 0 to 180 degrees.

Figure 4.2: FFT procedure for composite orientation measurement.

First, the CT volume is preprocessed using the "Straighten" function of Fiji, in order to remove the curvature of the cylinder. This ensures that a given slice of the tomography volume is contained within a single composite layer. Then, the average composite orientation is evaluated in each slice. To do that, the image is represented in the frequency domain, by applying the Fourier transform. If the grayscale intensity of the original image of dimensions $M \times N$ is represented as a

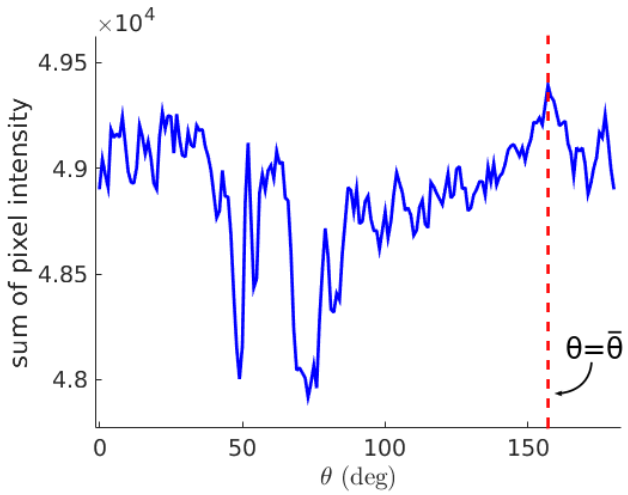

Figure 4.3: Normalized sum of pixel intensity along an angle on the power spectrum image. The red dashed line indicates the angle of maximum sum of pixel intensity, perpendicular to the average orientation of the original tomography slice (Figure 4.2a).

two-dimensional function of space $f(m,n)$, then its Fourier transform is

$$F(u,v) = \sum_{n=1}^{N}\sum_{m=1}^{M} f(m,n)\exp\left[-2\pi j\left(\frac{(u-1)(m-1)}{M}+\frac{(v-1)(n-1)}{N}\right)\right]. \quad (4.1)$$

The zero-frequencies are centred using the Matlab function "fftshift". The power spectrum of the Fourier transform is calculated as

$$P(u,v) = \mathrm{abs}(F(u,v)). \quad (4.2)$$

Figures 4.2a and 4.2b show an example of the original grayscale slice and the resultant power spectrum. From the power spectrum image, the orientation of the original image can be evaluated. To that end, the pixel intensity values of the power spectrum image are represented in polar coordinates, with the origin at the centre of the image:

$$P = P(r,\theta). \quad (4.3)$$

Next, the sum of pixel intensity is measured along angles θ_i from 0° to 180°, following the formula

$$I(\theta_i) = \sum_{r=-R}^{R} P(r,\theta_i), \quad (4.4)$$

where R is taken as half the width of the power spectrum image. The values of $I(\theta)$ for the power spectrum 4.2b are shown in Figure 4.3. The angle $\hat{\theta}$ corresponding to the highest sum of pixel intensity is defined through the equation

$$I(\hat{\theta}) = \max(I(\theta)). \quad (4.5)$$

The orientation Θ of the original image (Figure 4.2a) is perpendicular to the angle $\hat{\theta}$ and is obtained as

$$\Theta = \hat{\theta} - 90. \tag{4.6}$$

The composite ply orientation in the pressure vessel is measured by applying the procedure described above to each slice of the tomography volume in the through-thickness direction.

4.4 Results

Figure 4.4 shows voids visualized as particles in a CT volume with dimensions 26 mm × 21 mm × 17 mm. The scans show a large number of macroscopic voids with dimensions of several millimetres. The largest voids are found at the interfaces between composite layers with different orientations. An example of such void is shown in Figure 4.5. When the orientation changes, any concave areas are bridged by the yarns of the newly placed composite layer, leading to matrix accumulation and air entrapment in these regions. A similar mechanism can also be observed in helical plies, where yarns form an interlocking pattern. An example of this type of void is shown in Figure 4.6.

Voids located inside yarns are most often needle-shaped and strongly elongated along fibre direction. They are the main type of void found in the hoop plies, as shown in Figure 4.7. Since the failure of a pressure vessel depends predominantly on the strength of the hoop plies, this is also the type of void that is of particular interest for the current study.

Figure 4.8 shows a detail of the innermost hoop ply observed by microscopy. The image shows matrix-rich regions corresponding to yarn boundaries. Multiple voids are visible. There are some larger voids with dimensions in the order of 50 µm that could be detected at the available µCT resolution. These voids are often present at yarn boundaries. Some examples of these voids are shown in Figure 4.9. Additionally, there are multiple voids with cross-sectional dimensions close to 5 µm. These voids are not distributed uniformly, but tend to be concentrated in certain areas. An example of a region of the innermost hoop ply with multiple of these smaller voids is seen in Figure 4.10. Locally, these voids can be responsible for a large part of the void volume fraction. Due to their small dimensions, they are not visible in the µCT scans. For regions where these small voids are a dominant feature, µCT underestimates the void volume fraction.

Void volume fraction Void volume fraction is the most often reported void-related property. For the CT scans, it is defined as the summed volume of the voids divided by the total imaged volume. For the microscopy images, the void

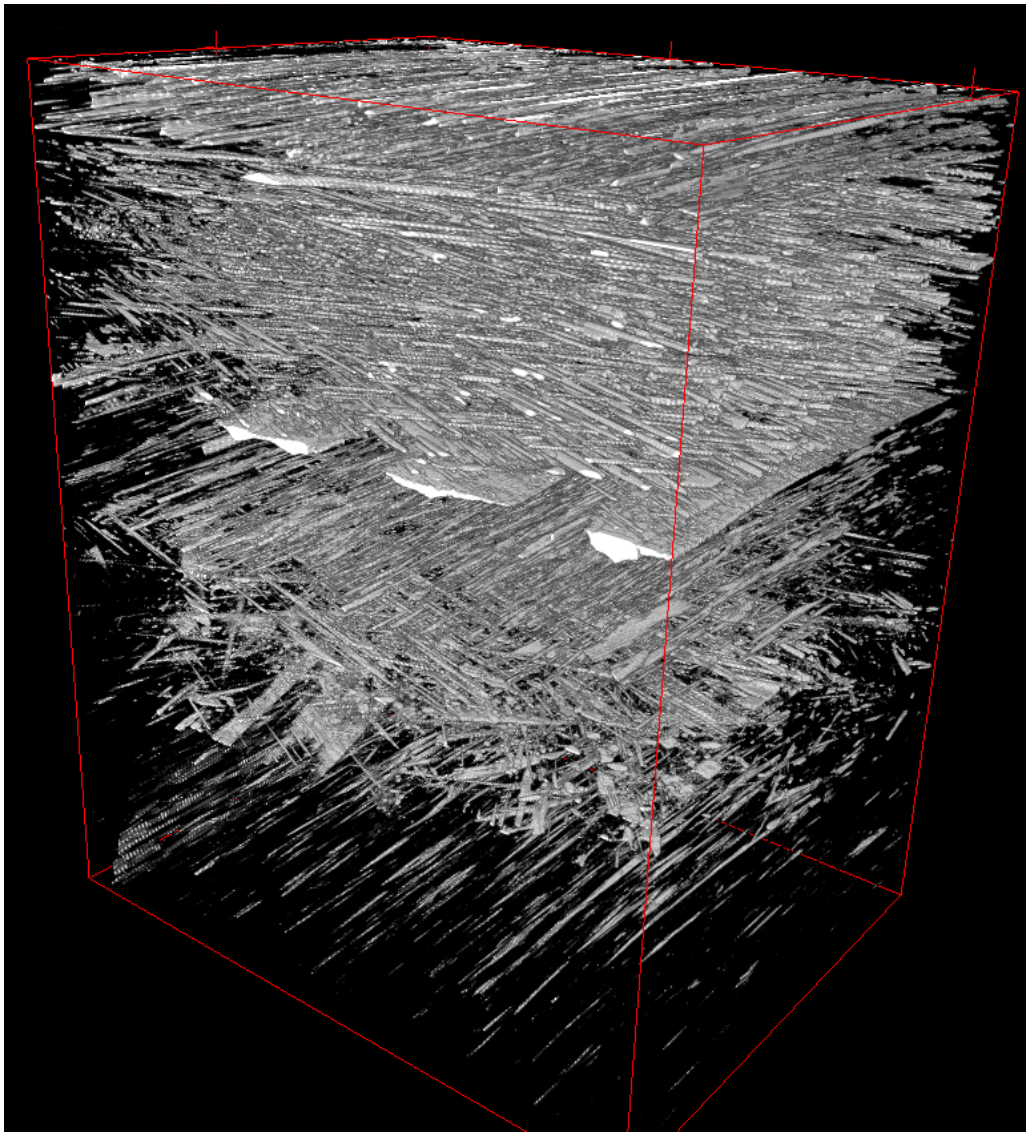

Figure 4.4: µCT: Three-dimensional visualization of voids in a scanned region of interest of dimensions 26 mm × 21 mm × 17 mm (red bounding box). The innermost hoop ply is at the bottom of the scan, and the surface ply is at the top.

area fraction in a micrograph can be a reasonable approximation of the volume fraction [67] [88]. The average void fraction measured through microscopy is equal to 2.8%, which agrees reasonably well with the 2.4% value obtained by µCT. However, the voids are not uniformly distributed. An additional analysis is performed to evaluate the through-thickness gradient of void fraction for both microscopy and µCT. Along the wall thickness, the images are divided into slices of approximately 0.6 mm thickness and void fraction is calculated in each of them. The results are shown in Figure 4.11. A clear through-thickness gradient is visible, with

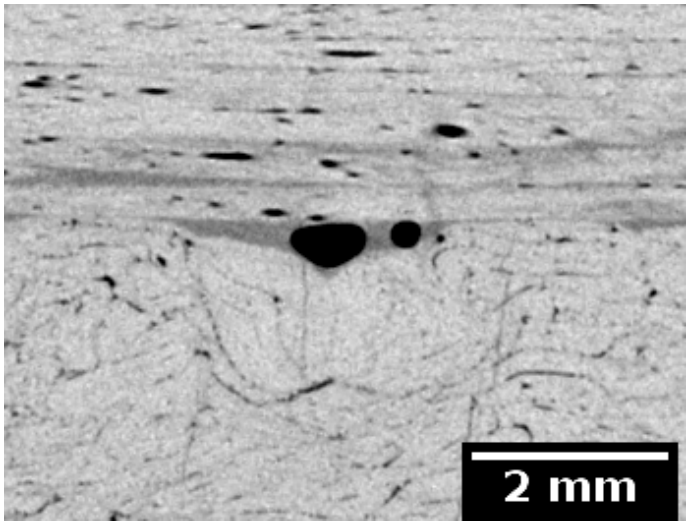

Figure 4.5: Tomography: Example of interlaminar voids. The hoop ply (bottom, fibres perpendicular to the image plane) was laid first. After a helical ply was wound on top of it, air entrapment caused the formation of matrix-rich regions and voids. Smaller intralaminar voids are also visible in both plies.

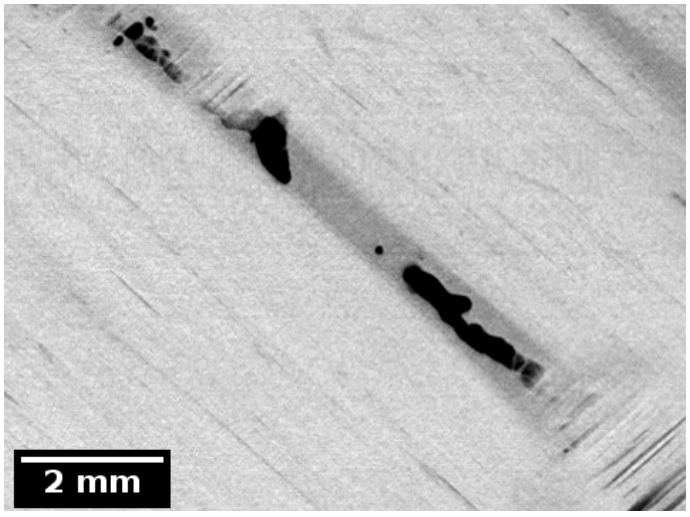

Figure 4.6: Tomography: Voids and matrix pockets formed in a gap between two yarns of a helical ply.

the lowest void fraction measured near the internal wall of the cylinder. A similar tendency was reported by Cohen [33] and Scott [135], whereas Pilato [120] observed a minimum void fraction close to the mid-thickness of the cylinder. The increased void fraction towards the outer wall could be explained by the weaker compaction force during the winding process, as well as the accumulation of resin and air being pushed out from the inner layers of the cylinder.

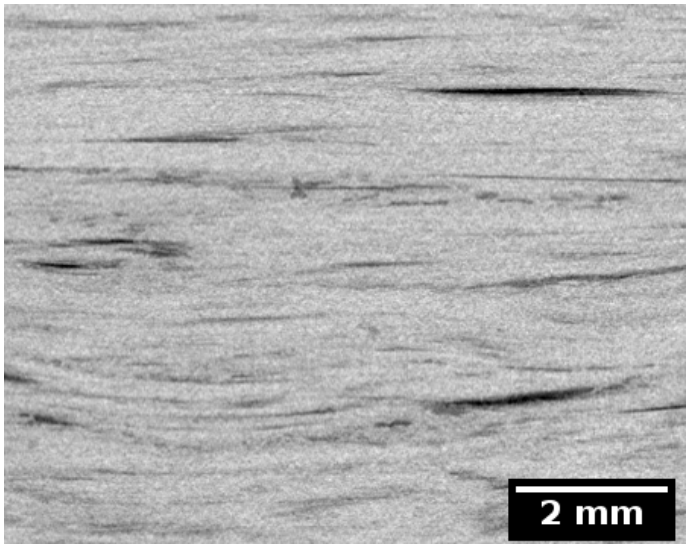

Figure 4.7: Tomography: Detail of a hoop ply. Fibres are oriented horizontally. Significant waviness and intra-yarn void presence are visible.

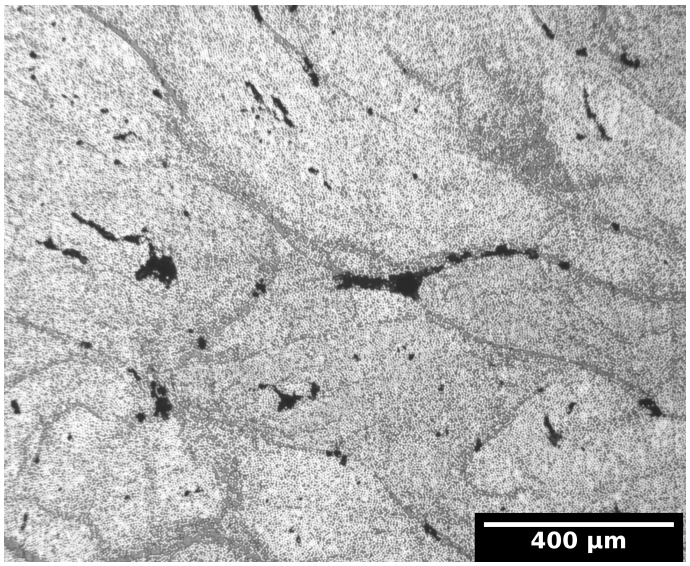

Figure 4.8: Optical microscopy: resin rich regions and voids are visible at interfaces between yarns. Macroscopic voids can have an irregular cross-section shape.

Void fraction values measured by microscopy show larger variation from point to point than those from tomography. This is especially visible in the regions with higher void fraction values. While there are fewer voids present there, their dimensions are on average larger than in the regions with a lower void fraction. This makes the microscopy measurement sensitive to a local bias. More representative values can be obtained by averaging the void fraction values on a ply-by-ply basis.

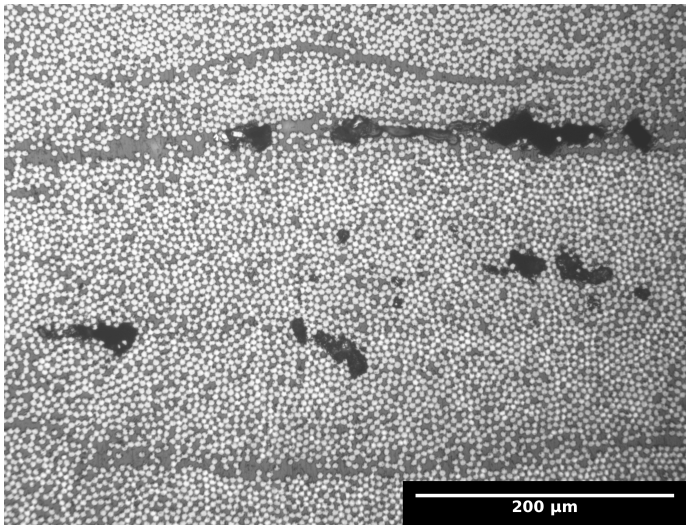

Figure 4.9: Optical microscopy: example of macroscopic voids in a hoop ply.

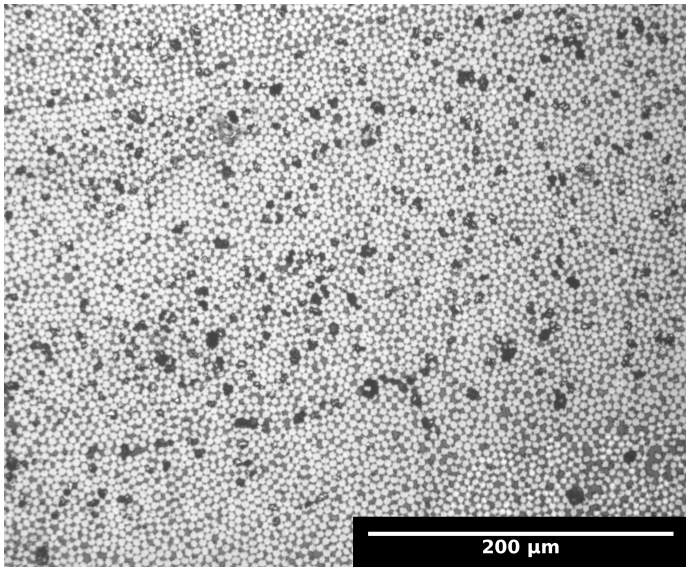

Figure 4.10: Optical microscopy: example of a region with a concentration of mesoscopic voids.

The results of such analysis are presented in Table 4.1. The ply orientations are measured using the image analysis algorithm introduced in Section 4.3. For most plies, a good match is seen between µCT and microscopy. The difference between the two is the largest in Ply 1, the innermost hoop ply. This is believed to be due to the relatively low resolution of the tomography scans, insufficient to capture small voids, which locally can be responsible for a large part of the total void volume, as observed through microscopy. For plies closer to the surface, where larger voids

account for the bulk of the void fraction, the two measurement methods show a very good agreement.

Ply	Angle	Thickness	V_v^{ms}	V_v^{ct}
1	90°	6.9 mm	0.9%	0.3%
2	±76°	0.94 mm	0.5%	1.4%
3	±25°	0.82 mm	0.5%	0.8%
4	±59°	0.66 mm	0.6%	0.8%
5	±49°	1.42 mm	1.9%	1.2%
6	±39°	0.66 mm	2.9%	3.6%
7	±16°	1.50 mm	3.5%	2.3%
8	90°	4.64 mm	3.2%	3.5%
9	±25°	1.80 mm	2.7%	3.9%
10	±20°	1.74 mm	5.1%	4.2%
11	±15°	3.34 mm	3.7%	3.7%
12	90°	1.68 mm	8.9%	5.0%

Table 4.1: Void volume fraction in the pressure vessel as measured by optical microscopy (V_v^{ms}) and computed tomography (V_v^{ct}). Plies are numbered from the interior to the exterior of the cylinder.

Void size and shape The knowledge of void volume fraction is not sufficient to analyze the effect of voids on the mechanical properties of the composite. The material response does further depend on void location, size and shape [68]. X-ray tomography is unique in its ability to provide fully three-dimensional information on void morphology. Therefore, a statistical study of void size and shape is carried out, using the particle analysis results, as described in Section 4.2.2. Over 135 000 voids are identified in a single CT volume of 26 mm × 21 mm × 17 mm. The largest interlaminar voids have a relatively irregular shape and due to their large dimensions, often do not fit within the boundaries of the imaged volume. These voids are treated as outliers and are excluded from the statistical analysis of void shape and orientation. Based on comparing the particle data and the µCT scan, an arbitrary threshold volume of 0.16 mm^3 (20 000 voxels) is selected, over which the voids are not included in the analysis. On the other end of the size spectrum, there are voids with a very small volume. In particular, orientation measurement is very sensitive to error at this scale. Therefore, voids smaller than 100 voxels (8×10^{-4} mm^3) are also excluded from the statistical analysis. For the analyzed volume, these smallest voids constitute 86% of the total number of cavities, yet are responsible for only 5% of the total void volume fraction. After excluding the largest and smallest voids, less than 10 000 cavities remain for the statistical analysis. Void volume distribution after excluding the largest and smallest cavities is presented in Figure 4.12. The

number of voids decreases quickly at higher volumes. The y-axis of the histogram is shown on a logarithmic scale, since on a linear scale the bars near the right-hand side of the histogram would be hardly visible.

To quantify the shape of the observed voids, void elongation factor is defined as proposed by Mehdikhani [96]:

$$EF = \frac{c}{\sqrt{ab}}, \tag{4.7}$$

where c, b and a are the major, semi-major and minor axes of the inertia ellipsoid, respectively. The geometric mean $\sqrt{ab}$ corresponds to the radius of a circle with the same area as the void cross section. It should be noted that the curvature of the cylinder is not taken into account in this analysis. However, this is assumed to have a negligible effect due to small dimensions of most voids. The distribution of the elongation factor is shown in Figure 4.13. The average elongation factor is approximately equal to 9. 80% of voids have an elongation factor larger than 4. This confirms the observation that most voids within the analyzed volume range are strongly elongated (needle-shaped).

Another important parameter is void orientation. As mentioned previously, void orientation is defined as the orientation of the major axis of its inertia ellipsoid. Firstly, the out-of-plane angle of the voids is considered, as shown in Figure 4.14. It can be seen that the voids predominantly follow the plane of the composite. Therefore, the orientation analysis will only consider void angle with respect to the composite plane and the out-of-plane angle is assumed to be approximately zero. Voids are mostly oriented along fibre direction, as confirmed by Figure 4.15, showing histograms for a helical ($\pm 15°$) and a hoop ply. This is further confirmed by Figure 4.16, which presents void orientation with respect to their through-thickness position. Each void is represented by a single blue dot and the red line corresponds to the composite ply orientation.

4.5 Conclusions

The microscopy and tomography observations allow a detailed characterization of void content in the cylindrical section of the composite pressure vessel, as well as void size and shape. The experimental observations confirm that voids are commonly present in pressure vessels and show a relatively high void volume fraction. Both methods provide a similar value of average void fraction: 2.4% for tomography and 2.8% for microscopy. For the described measurement methods, void volume fraction at the ply level shows good agreement for the two methods in most cases. An important through-thickness gradient is observed, with void fraction increasing toward the outer cylinder wall. No clear correlation is found between void content

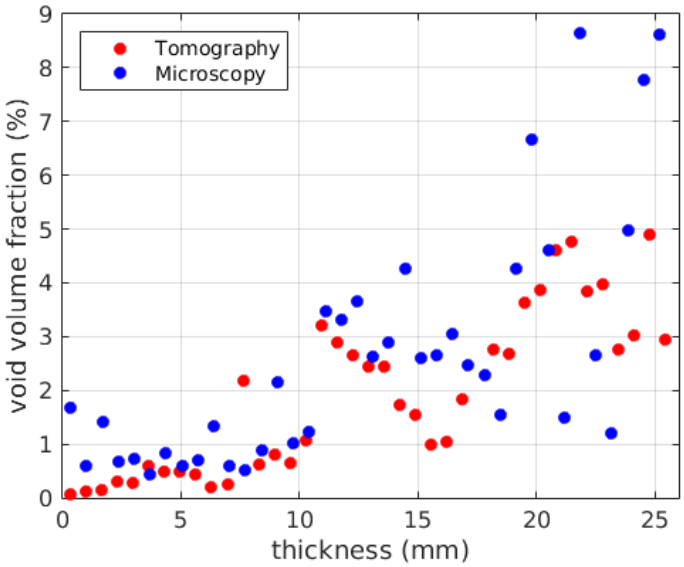

Figure 4.11: Void volume fraction in the through-thickness direction of the pressure vessel wall. The thickness is measured from the interior of the cylinder. The dots represent average values measured over regions of approximately 0.6 mm thickness.

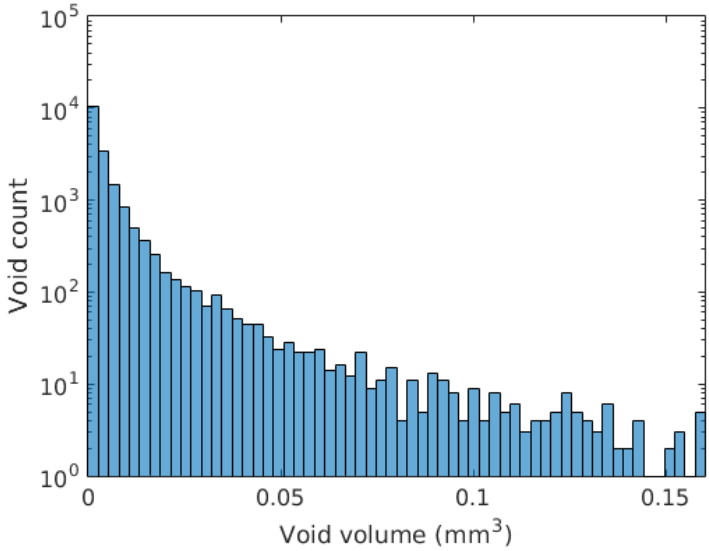

Figure 4.12: Computed tomography: void volume distribution after excluding voids smaller than 100 and larger than 20000 voxels.

and ply orientation. However, this effect could be masked by the through-thickness void fraction gradient.

A wide range of void volumes is observed. As can be seen from Figure 4.12,

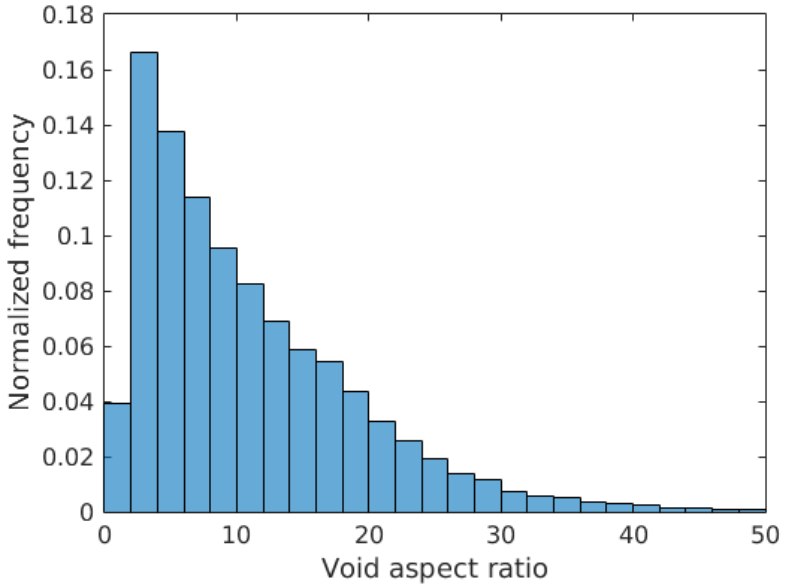

Figure 4.13: Void aspect ratio distribution. The measurements were carried out on the volume represented in Figure 4.4.

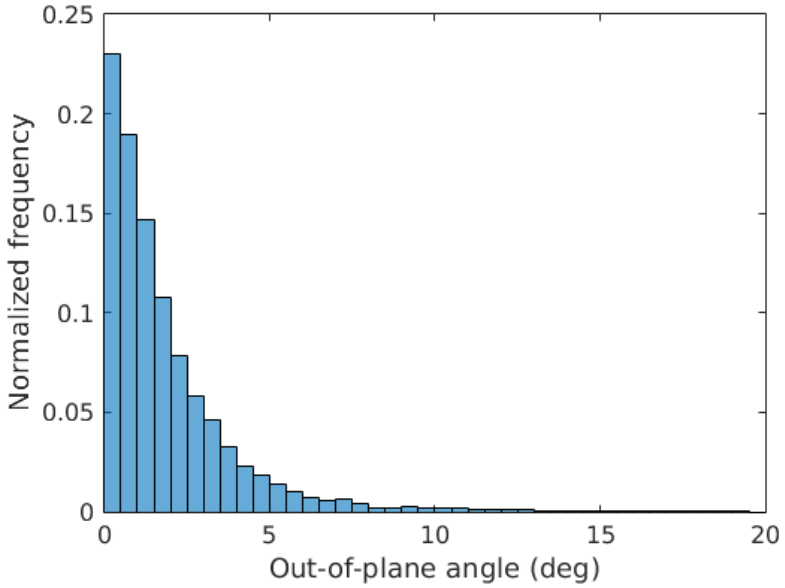

Figure 4.14: The out-of-plane angles of the voids in the pressure vessel. Only void with volumes larger than 100 voxels are included. The measurements were carried out on the volume represented in Figure 4.4.

there are no obvious boundaries which would allow classifying voids by their size.

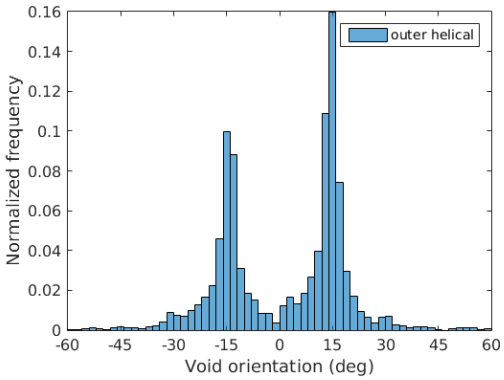

(a) Helical ply (±15°).

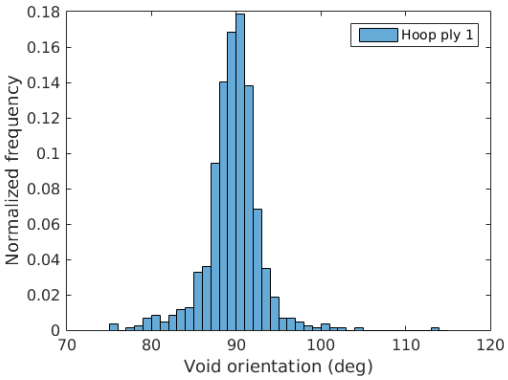

(b) Hoop ply (90°).

Figure 4.15: Void orientation in a helical and hoop ply. Voids predominantly align with the fibres.

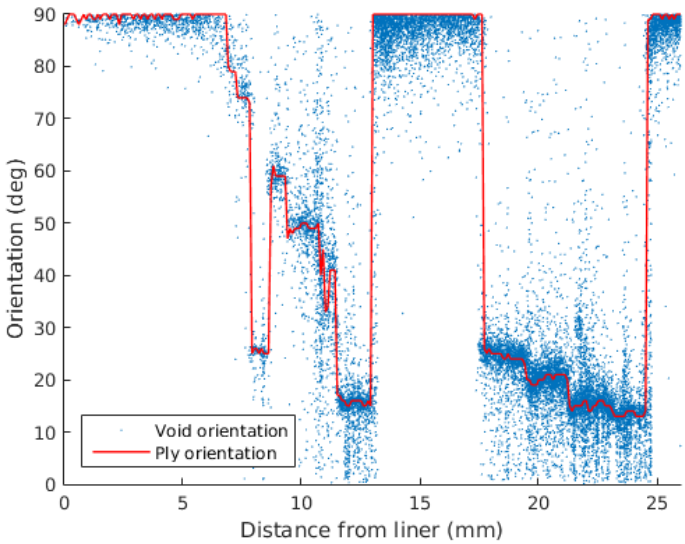

Figure 4.16: Individual void orientation superposed over ply orientation.

However, a qualitative classification can be made into the three following groups:

(i) *macroscopic voids*: mostly needle-shaped, oriented along fibre direction, with cross-sectional dimensions of several fibre diameters or larger
(ii) *mesoscopic voids*: needle-shaped, oriented along fibre direction, with cross-sectional dimensions close to fibre diameter
(iii) *microscopic voids*: approximately spherical cavities (pores), with dimensions inferior to fibre diameter; generally not observable at the resolution available in this study, but described in the literature [88]

The three types of voids are schematically represented in Figure 4.17. The approach to modelling void influence on the mechanical properties of the composite will depend on which group they are assigned to. Macroscopic and mesoscopic voids, oriented along fibre direction, are the dominant feature present in the filament-wound composite pressure vessel. Their influence is analyzed in Chapter 6, presenting an experimental study aimed at quantifying the influence of voids on composite strength under loads present in thick-walled composite pressure vessels.

Microscopic voids are significantly different from both macroscopic and mesoscopic ones. Their small size allows them to be homogenized in the matrix behaviour, in the framework of mechanics of porous media. The presence and growth of this type of voids in an epoxy resin is the topic of an experimental and numerical study presented in Chapter 5.

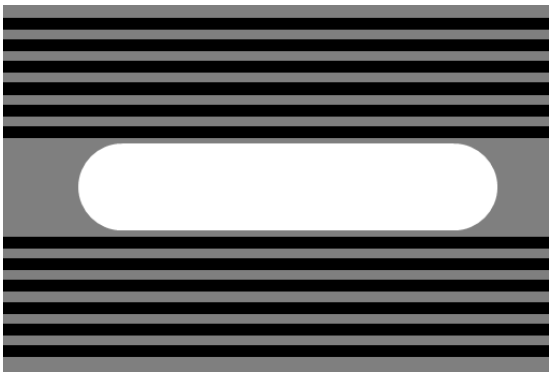

(a) Macroscopic void.

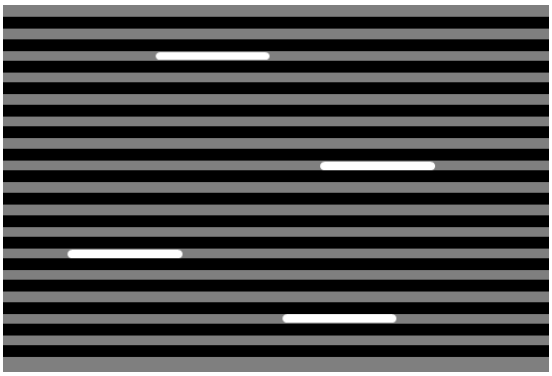

(b) Mesoscopic void.

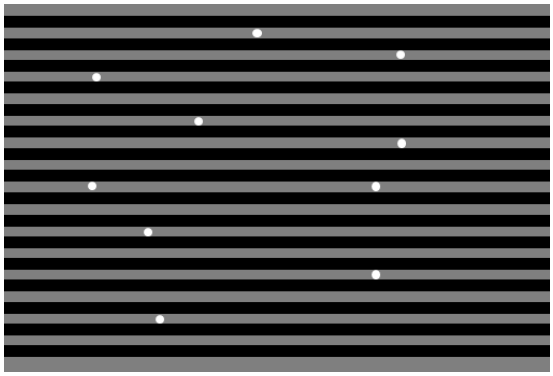

(c) Microscopic void.

Figure 4.17: Void classification.

Chapter 5

Microscopic void growth measurement and modelling in a thermosetting epoxy resin

The chapter is based on the following article [131]:

J. Rojek, C. Breite, Y. Swolfs and L. Laiarinandrasana. Void growth measurement and modelling in a thermosetting epoxy resin using SEM and tomography techniques. *Continuum Mechanics and Thermodynamics* (2020).

Chapitre 5. Mesure et modélisation de la croissance des cavités microscopiques au sein d'une résine époxy thermodurcissable

En dehors des cavités macro- ou mésoscopiques, discutées dans le Chapitre 4, ils existent aussi des cavités microscopiques dans la résine époxy, approximativement sphériques. Dans ce chapitre, une étude expérimentale et numérique présente la relation entre la croissance de ce type de cavités dans une résine époxy exposée à une sollicitation multi-axiale et son comportement mécanique.

Des éprouvettes époxy cylindriques à double entailles ont été fabriquées, puis sollicitées en traction jusqu'à rupture. Des rayons de fond d'entaille de 6 mm (éprouvettes NT6) et 1 mm (NT1) ont été testés. Les entailles introduisent un état de contraintes multi-axial et localisent la rupture. Au moment de celle-ci, l'une des entailles se casse, tandis que l'autre est déchargée, ce qui correspond à un essai interrompu. Les images des éprouvettes prises pendant les essais sont utilisés pour mesurer les déplacements locaux, tels que l'ouverture d'entaille et la réduction radiale.

Les surfaces à rupture des éprouvettes sélectionnées ont été examinées à l'aide de la microscopie électronique à balayage. Les observations mettent en évidence des sites d'amorçage typiques de la rupture fragile, liés à un défaut critique, sous la forme d'un cluster des cavités, particules ou plus simplement une inclusion. Les sites d'amorçage sont localisés à proximité de l'axe de l'éprouvette pour NT6, tandis qu'ils se trouvent près du bord de l'entaille pour NT1. Ceci souligne la sensibilité de l'époxy à l'état de contraintes multi-axiale.

Les entailles non-rompues de quatre éprouvettes ont été examinées par tomograhie au rayonnement synchrotron. Les volumes tomographiques ont été obtenus tant au sein qu'à l'extérieur des entailles, dans le but de tracer l'évolution de la distribution radiale de la porosité. La fraction volumique locale est évaluée dans un volume d'intérêt, qui est un cube de 250 µm de côté.

En utilisant les résultats MEB et la tomographie, on peut tracer l'évolution de la distribution radiale de la porosité à trois instants successifs :

1. l'état initial (tomographie réalisée sur la partie cylindrique en dehors de l'entaille)
2. au sein de l'entaille peu avant la rupture
3. après la rupture (fractographie MEB)

Aucune germination des porosités n'a été constatée entre les étapes 1 et 2, ce qui permet de conclure que l'évolution de la fraction volumique est uniquement dû à la croissance des porosités. Il est observé que la croissance des cavités a principalement lieu à proximité de l'axe de l'éprouvette pour NT6, et près du bord de l'entaille pour NT1. Ceci est le cas quelle que soit la distribution initiale des porosités.

Ensuite, l'état local de contraintes est calculé par la méthode des éléments finis, en utilisant la loi de comportement modifiée de Gurson-Tvergaard-Needleman (GTN). Les paramètres du modèle sont obtenus par optimisation inverse, en prenant en compte les observations macroscopiques (l'ouverture d'entaille) et microscopiques (la croissance des cavités). La simulation numérique prévoit que la contrainte principale maximale atteint sa valeur la plus élevée à proximité de l'axe de l'éprouvette pour NT6 et près du bord de l'entaille pour NT1. S'appuyant sur les observations expérimentales et les résultats numériques, un critère de rupture fragile est proposé, basé sur la combinaison de la valeur critique de la contrainte principale maximale et la présence d'un défaut critique.

5.1 Introduction

As discussed in Chapter 4, voids are present at different scales of the composite. At each scale, a different approach is necessary to analyze their influence on the composite material behaviour. In this chapter, an experimental study is carried out to analyze the relationship between microscopic void growth and the mechanical response of a thermosetting epoxy resin. Thermosetting epoxy resins are widely used as matrix materials in fibre-reinforced composites. They offer good mechanical properties, as well as chemical, electrical and elevated temperature resistance. Due to their numerous advantages, epoxy resins have become the most common choice in high-performance composite applications, e.g. in airframes.

To study the micromechanical behaviour of composites, it is necessary to characterize the mechanical properties of the resin. Tensile strength of polymers is routinely measured under uniaxial conditions. However, it is not clear how well these measured properties represent resin behaviour inside a composite. Locally, the polymeric matrix can experience significant deformations under multiaxial stresses [85]. This is true both for matrix-driven failure modes, as well as for fibre-dominated failure. In the latter case, single filament breaks cause local overstressing, which can lead to a formation of fibre break clusters [138]. The redistribution of stress onto the neighbouring fibres depends strongly on the properties of the matrix, which is subjected to a multiaxial and dynamic stress state [150]. It is therefore desirable to characterize the mechanical response of the polymer taking into account more complex loading conditions.

Another aspect to consider is the presence of voids in the resin. They are commonly encountered at different scales of the composite. Void growth and the influence of stress triaxiality have been studied in several thermoplastic semi-crystalline polymers, e.g. by Laiarinandrasana et al. [83], Challier et al. [23], Boisot et al. [14], Selles et al. [140]. In turn, thermosetting polymers, such as epoxy, have been usually considered to exhibit brittle failure without observable void growth, at least under tensile loading [101].

The objective of the study described here is to quantify void growth inside a thermosetting epoxy resin and provide an interpretation of the damage evolution. To this end, double-notched round bars are tested in tension. The triaxiality ratio is controlled by modifying the notch root radius. SEM and computed tomography techniques are used to evaluate in detail void growth inside the material. The next step consists in optimizing a Gurson-Tvergaard-Needleman (GTN) material behaviour [160] to model the void growth and stress state in the tested specimens. The aforementioned studies on thermoplastics use the GTN model under the assumption of a homogeneous initial void distribution [22] [84]. A critical void fraction criterion is used [23] [14], while in epoxy failure is typically linked to the presence of a critical defect [21]. In the study presented, a brittle failure criterion

is proposed and a non-uniform initial void distribution is taken into account. The obtained experimental and numerical results offer an insight into the mechanics of a thermosetting epoxy, improving the understanding of its failure and the damage processes that lead to it.

5.2 Material and methods

5.2.1 Epoxy resin material and specimen geometries

"In-house prepregging" epoxy Sicomin SR 8500 / KTA 313 slabs were produced using a method similar to that described by Morelle et al. [101]. The manufacturing process consisted of several steps. At first, the bisphenol-A type epoxy resin and the diamine hardener were degassed individually for 60 min at 70 °C. In a second step, the two components were thoroughly mixed and degassed again for 10 minutes at 70 °C. The degassed mixture was then poured into cylindrical glass moulds, coated with a high slip mould release agent Chemlease PMR-90 EZ. The filled moulds were held for 60 min at 70 °C in a convection oven, before the temperature was ramped up from 70 °C to 120 °C over a period of 50 min. The temperature was then held constant for 90 min. Once the curing step was finished, the oven was cooled down over a period of 120 min.

Axisymmetric double-notched round bars were machined from the obtained cylindrical epoxy slabs. The geometry of the specimens is shown in Figure 5.1. Two notch root radii were studied: 6 mm and 1 mm. The specimens are identified as NTx-y, where NT stands for "notched tensile", x is the notch root radius in millimetres and y is the specimen number. For both specimen geometries, the diameter outside the notch (gauge diameter) is 7 mm and notch depth is 1 mm, resulting in the net section diameter of 5 mm and a notch-to-depth ratio of 0.29.

Single and double-notched specimens similar to the ones described above have been used in a number of previous studies on damage development and failure in semi-crystalline polymers [83][14][140][22][84]. In smooth (unnotched) specimens under a tensile load, a multiaxial stress state develops locally with the onset of necking. However, the location of the necked region cannot be controlled. Introducing a notch localizes the multiaxial stress region and mimics a necked specimen. This is particularly helpful in case of a brittle material, like the epoxy studied here, which otherwise exhibits little observable necking.

In this study, it was desirable to stop mechanical tests shortly prior to failure and observe damage development. However, the moment of interrupting the test is hard to determine for a brittle material. This problem was solved by using a double-notched geometry. When under load, both notches experience the same stress state.

Eventually, a critical defect causes one of them to fail, while the other one is abruptly unloaded.

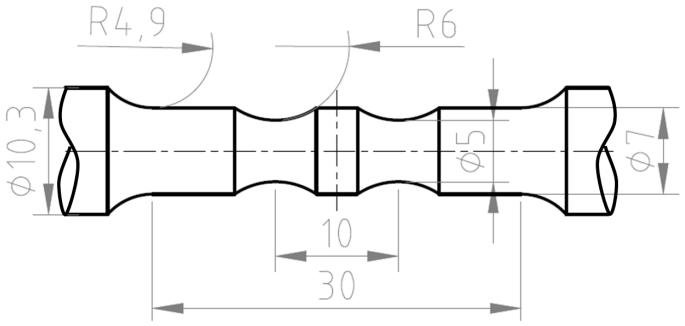

(a) NT6.

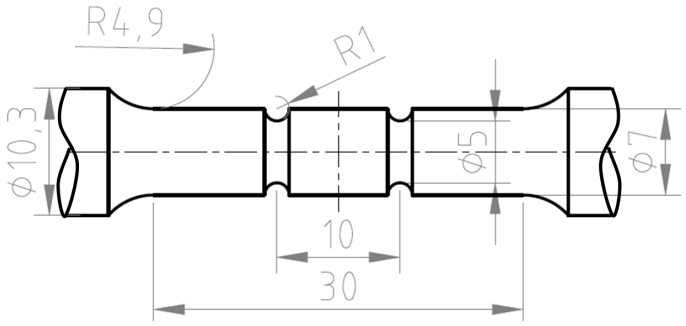

(b) NT1.

Figure 5.1: Specimen geometry. Dimensions in mm.

5.2.2 Tensile tests

The double-notched specimens described above were loaded in tension until failure on an electromechanical tensile rig with displacement control. All tests were carried out at room temperature. The cross head speed was 0.2 mm/s and 2.0 mm/s for NT1 and 0.2 mm/s for NT6 specimens. The initial grip distance was 39.6 mm for all tests. At least two specimens were tested for each combination of geometry and loading rate.

The testing rig was equipped with a video acquisition setup. Photographs were recorded during the tests at a rate of at least two frames per second. From the obtained images, approximately fifteen were selected for each specimen, in order to capture the characteristic moments of the entire test. From these photographs, several local displacements were measured using an open-source image analysis software Fiji [134], in locations shown in Figure 5.2. The approximate resolution of the photographs was 50 pixel/mm. The following measurements were taken:

- axial displacement between point markers on the external sides of the notches ($\Delta L = L - L_0$)
- notch opening displacement ($NOD = (a - a_0)/2$)
- radial reduction ($\Delta R = R_0 - R$)

Notch opening displacement was calculated as a mean of four measurements (on both sides of the two notches). Similarly, radial reduction values were averaged over both notches. The local character of these measurements is particularly important in case of notched specimens, where cross head displacement provides purely macroscopic information on the deformation process.

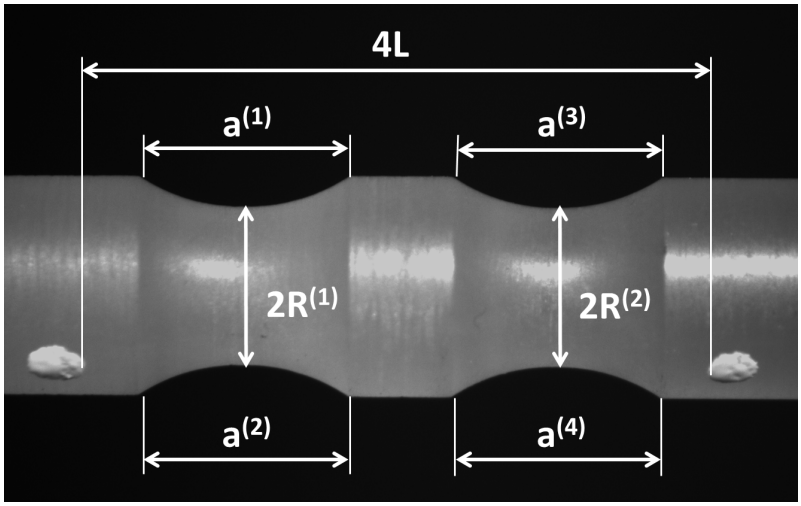

Figure 5.2: Macroscopic measurements.

5.2.3 Scanning Electron Microscopy - Fractography

Scanning Electron Microscopy was used to observe the fracture surfaces of the broken notches of four specimens: NT6-1, NT6-2, NT1-1 and NT1-2. The observations were carried out on a FEI Nova NanoSEM 450, at 5 kV voltage and 50 pA current. A 9 nm Au/Pd coating was applied to improve conductivity. The objective was to study the morphology of the fracture surfaces and the location of the fracture initiation sites. Furthermore, the images were used to extract information about microscopic voids: their location, number and size.

Approximately 25 % of each specimen's fracture surface was mapped at a 250× magnification. This ensured sufficient resolution to identify the voids. Up to fifty individual scans were digitally merged for each specimen using the Fiji stitching tool [125]. Voids were then counted manually and their spatial coordinates and maximum Feret diameters [45] were measured. Then, each void's cross-sectional

area was estimated as that of a circle with its diameter equal to the void's maximum Feret diameter.

5.2.4 Synchrotron Radiation Computed Tomography

After tensile testing, voids in the unbroken notches of the aforementioned four specimens (NT6-1, NT6-2, NT1-1 and NT1-2) were observed using Synchrotron Radiation Computed Tomography (SRCT). SRCT offers a much higher radiation intensity than laboratory micro-computed tomography, allowing fast imaging at sub-micron resolutions. It is a convenient non-destructive method of imaging microstructures in three dimensions. The scans were obtained on the ANATOMIX beamline of Synchrotron SOLEIL (France) [170]. Radiographs were taken at 2000 angular positions during a 180° rotation lasting approximately 7 min, with a 16 keV beam energy. The voxel size was 650 nm.

Each scan covered a cylinder with both height and diameter equal to 1.3 mm, resulting in a volume of 1.73 mm^3. These volumes will from now on be referred to as Tomographic Volumes of Interest (TVOI). It would have been very time-consuming to image the entire specimens at a resolution allowing void characterization. Therefore, it was necessary to choose characteristic locations. Figure 5.3 indicates which TVOIs inside the specimens were imaged. In specimens NT6-2 and NT1-2, two radial paths were covered in the net section, spanning the complete diameter. This was done to assess if void distribution was close to axisymmetric. In the other two specimens, a radial path was followed both at the net section and outside the notched region, in order to evaluate void growth in the notch. For NT6-1, only part of the radial path outside the notch was covered, but an additional TVOI was obtained along specimen axis, in order to extract information on the axial void distribution.

An image analysis segmentation procedure was applied to the tomography volumes. Voids were recognized as local minima of the greyscale distribution [84]. Figure 5.4 shows an example of the original tomography slice and the resultant segmentation. The algorithm could erroneously identify voids on the surface of the specimen, therefore the edge was excluded from the analysis. After carrying out the segmentation, void position, volume and equivalent ellipsoid dimensions were calculated.

5.2.5 Volumes and Surfaces of Interest

To describe void volume fraction distribution inside the tomography volumes, it is necessary to define a Statistical Volume of Interest (SVOI), over which a local void volume fraction is calculated. It needs to be small enough to ensure homogeneity

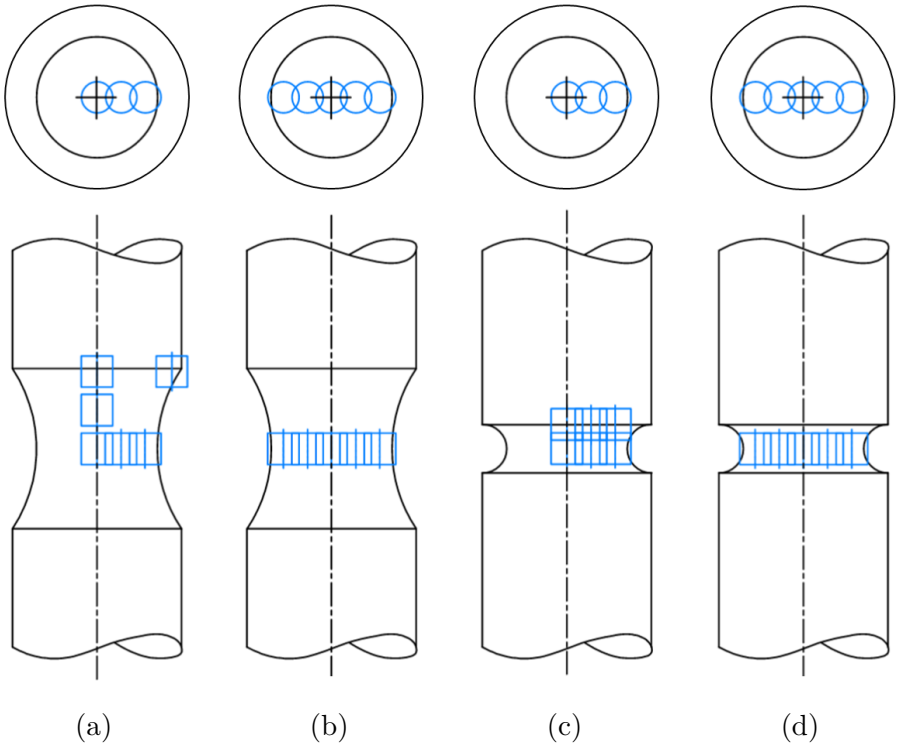

Figure 5.3: SRCT: Positions of the Tomographic Volumes Of Interest (TVOI) for the scanned specimens: **a)** NT6-1, **b)** NT6-2, **c)** NT1-1, **d)** NT1-2.

of void volume fraction inside of it, but large enough to contain multiple voids. The choice of SVOI is therefore microstructure-dependent. In a similar analysis conducted on polyamide 6, it was defined as a (50 µm × 50 µm × 40 µm) cuboid [84]. For the work presented here, it was decided to use a cubic SVOI. A study was conducted to evaluate the influence of SVOI size on the void volume fraction measurement. Figure 5.5 shows a representative example of the calculated void volume fraction as a function of SVOI edge length. For small SVOI sizes, void fraction shows strong oscillations. It stabilizes when the edge length reaches 200 µm and does not change significantly, as the size of SVOI is further increased. Given these results, an edge length of 250 µm was chosen for the cubic SVOI used in the study presented here.

Each SVOI is provided with several statistics: number of voids, coordinates of individual voids, their volume and equivalent ellipsoid dimensions. To determine the void volume fraction at a given location, a SVOI with a barycentre at that point is considered. Void volume fraction is calculated as the summed volume of all voids inside the SVOI divided by the volume of the SVOI.

Figure 5.6 illustrates how the concept of SVOI is used to evaluate void volume

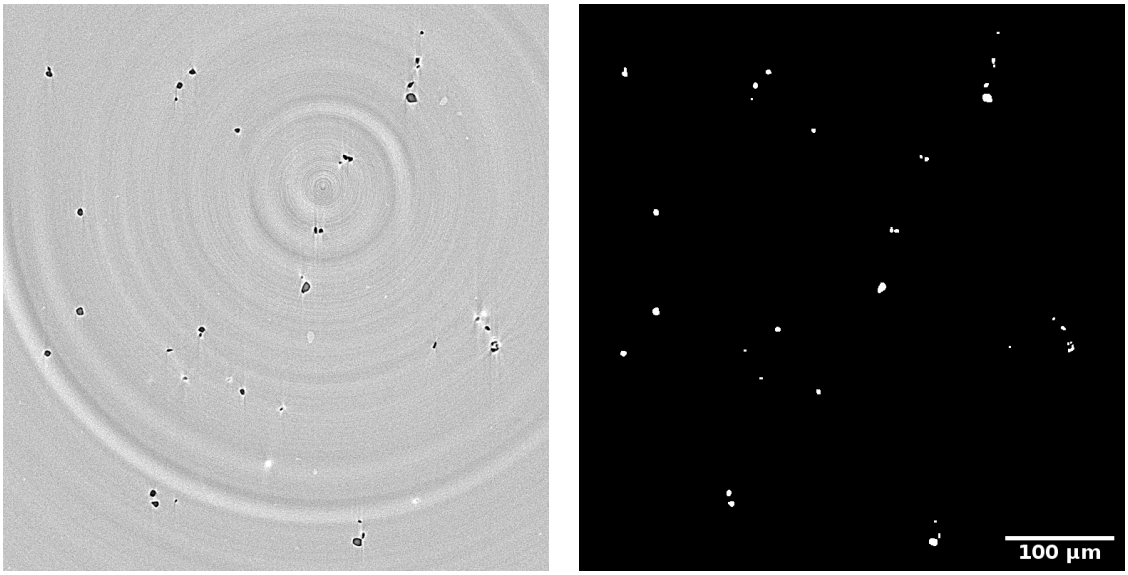

(a) (b)

Figure 5.4: Detail of a tomography volume slice **a)** before and **b)** after void segmentation.

fraction distribution along a radial path in the plane of the net section of a specimen. First, it is necessary to obtain three TVOIs spanning the distance from the axis to the edge of the specimen. Then, adjacent SVOIs are stacked, with their barycentres located along the radial path. The void volume fraction along the path is then measured from these SVOIs.

By analogy to the SVOI concept, a Statistical Surface of Interest (SSOI) was introduced for the SEM results. In order to simplify the comparison with SRCT results, it was decided to use a square of (250 µm × 250 µm). Figure 5.7 illustrates how void area fraction is sampled along several radial paths. A sequence of adjacent SSOIs is constructed along a given path. For each SSOI, the number of voids is known. Histograms are available for the maximum Feret diameter of the voids. Depending on the size of the scanned part of the fracture surface, several radial paths can be sampled. In this case, three radial paths are represented.

5.2.6 Finite element modelling

Finite element analysis is required to compute the local stress tensor in the specimens. The experimental results were used to calibrate a numerical model of the material. Taking advantage of symmetry, only a half of one notch was meshed. Eight-node quadrilateral axisymmetric elements (CAX8) were used. The mesh was most refined in the notch, with element size of approximately 50 µm. A displacement

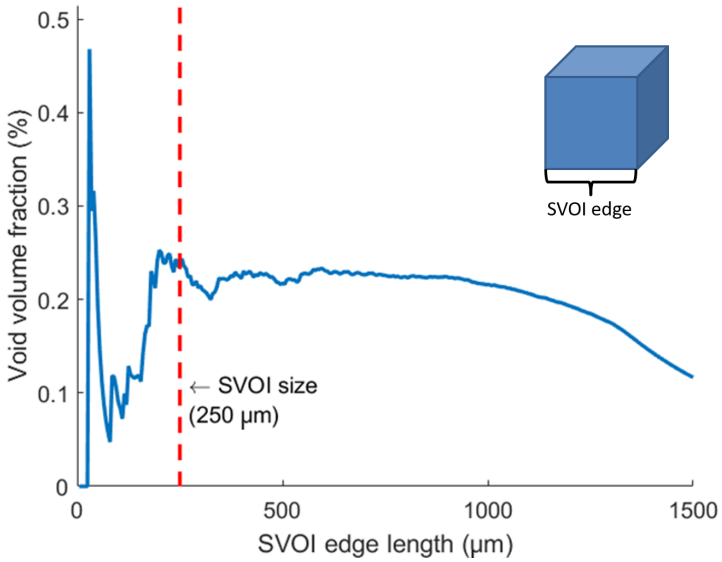

Figure 5.5: Void volume fraction as a function of SVOI size in a representative TVOI (Specimen NT6-2).

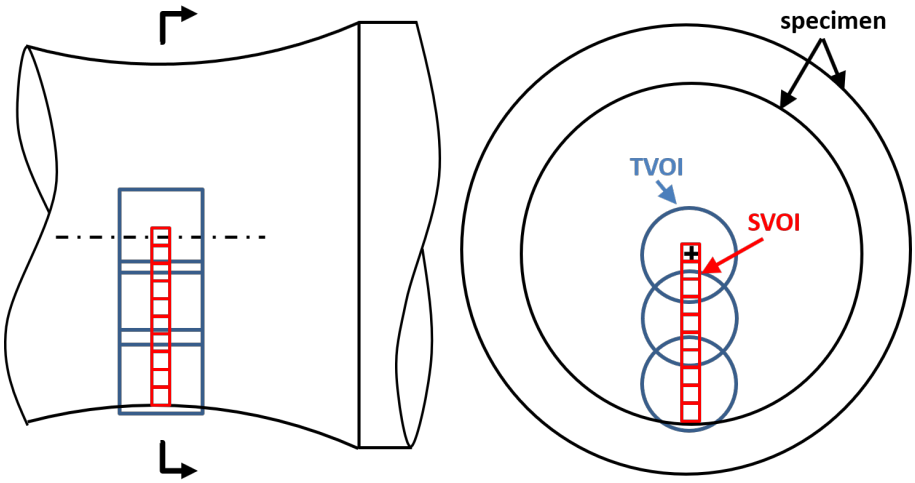

Figure 5.6: SRCT: volumes of interest in the notched region of the specimen. Black line represents the edge of the specimen, each blue cylinder is a Tomographic Volume of Interest (TVOI) corresponding to a single tomography volume and each red cube is a Statistical Volume of Interest (SVOI).

boundary condition was applied at the top edge of the mesh. Its value was based on the displacement ΔL measured from the tensile tests. The simulations were stopped when ΔL reached the value at which the simulated specimens failed in the tests.

The constitutive law used was a modified Gurson-Tvergaard-Needleman (GTN)

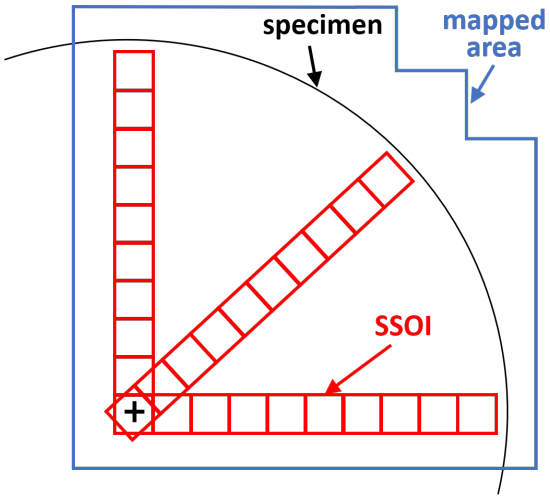

Figure 5.7: SEM: illustration of the process of calculating the radial distribution of void volume fraction on the fracture surface. Statistical Surfaces of Interest (SSOI) represented in red are squares with a 250 µm edge. The mapped part of the fracture surface is outlined in blue. The edge of the specimen is marked with a black line.

model. It consists of the original micromechanical approach of Gurson [50], extended based on phenomenological considerations by Tvergaard [159] and Needleman [160]. It is capable of taking into account time-dependent deformation, as well as volume variation caused by void growth and nucleation. Void volume fraction being an internal variable of the model, its distribution can be compared to that measured experimentally. In the work presented, this modelling approach is applied to a thermosetting polymer. Only the principal equations of the constitutive law are recalled here. A more detailed description can be found elsewhere, e.g. in Laiarinandrasana et al. [83].

The GTN porous potential is governed by the following equation, implicitly defining an effective scalar stress: σ^* [7]:

$$\Phi(\boldsymbol{\sigma}, \sigma^*, f) = \frac{\sigma_{eq}^2}{\sigma^{*2}} + 2q_1 f \cosh\left(\frac{q_2 \mathrm{tr}(\boldsymbol{\sigma})}{2\sigma^*}\right) - (1 + q_1^2 f^2) = 0, \tag{5.1}$$

where σ_{eq} is the von Mises stress, f is the void volume fraction, while q_1 and q_2 are constant material coefficients. The yield surface is defined as

$$\varphi = \sigma^* - \mathcal{R}, \tag{5.2}$$

where R is the flow stress modelled through

$$\mathcal{R} = \mathcal{R}_0 + Q(1 - \mathrm{e}^{-bp}), \tag{5.3}$$

with material coefficients $\mathcal{R}_0$, Q and b, and p being the cumulative plastic strain. The viscoplastic strain tensor is then written as

$$\dot{\boldsymbol{\varepsilon}}_v = (1-f)\dot{p}\frac{\partial \varphi}{\partial \boldsymbol{\sigma}}. \tag{5.4}$$

The cumulative plastic strain is governed by Norton law:

$$\dot{p} = \dot{\varepsilon}_0 \left\langle \frac{\varphi}{K} \right\rangle^n, \tag{5.5}$$

where $\dot{\varepsilon}_0 = 1\,\mathrm{s}^{-1}$ and K and n are material coefficients. Finally, the evolution of void volume fraction is obtained from the equation

$$\dot{f} = (1-f)\mathrm{tr}(\dot{\boldsymbol{\varepsilon}}_v). \tag{5.6}$$

Altogether, the model requires determining the values of nine material coefficients: elastic coefficients E and ν, hardening parameters R_0, Q and b, void interaction parameters q_1 and q_2 and Norton parameters K and n.

5.3 Results and Discussion

5.3.1 Data at the macroscopic scale from the tensile tests

As anticipated, all specimens failed in the net section of one of the notches. In NT6 specimens, the notch which would break showed an increasingly larger NOD shortly prior to failure than the second notch. The failure of NT1 specimens was more brittle, with less discernible radial reduction and little difference between the two notches. This can be verified from Figure 5.8, showing NOD as a function of $\Delta L/L_0$ for the four studied specimens (NT6-1, NT6-2, NT1-1 and NT1-2). The two types of dashed lines correspond to the two notches. There are two lines for each notch, each one representing a single measurement, as explained in Section 5.2.2. The solid bold line is the average of all four measurements. It can be seen that while for NT6 a higher NOD allows a prediction that the notch will break, there is no such correlation for NT1.

Figure 5.9a shows the average values of NOD with respect to $\Delta L/L_0$ for all tested specimens. The curves show a dependence on notch root radius and deformation rate. A good linear correlation between $\Delta L/L_0$ and NOD is an indication that the deformation of the specimen takes place predominantly within the notched region. It was therefore assumed that no void growth occurred outside the notch. In the analysis of the tomography data, the void volume fraction outside the notch is treated as equivalent to the initial one.

Re-necking is a phenomenon in which necking appears in the net section of an initially notched specimen. It has been described for semi-crystalline materials [83] [23]. For the epoxy studied, re-necking was observed in the NT6 specimens, manifesting through a strong increase in radial reduction, shown in Figure 5.9b in function of the normalized displacement. In semi-crystalline polymers, this increase is followed by a plateau, which was not present in epoxy. For the NT1 epoxy specimens, no re-necking was observed and the radial reduction curve was approximately linear.

Figure 5.10 shows the net stress as a function of notch opening displacement. Net stress is defined as load divided by the net section area. Strain softening was observed in NT6 specimens near the end of the tests. This, together with an increased rate of radial reduction mentioned above, points to a more intensive void growth process at this stage. It is also observed that a decrease in notch root radius (and therefore an increased stress triaxiality ratio) leads to a higher maximum value of net stress, as observed previously for semi-crystalline polymers [83].

An unexpected strain rate effect was observed for NT1 specimens, where a higher loading speed led to a slight stiffness reduction. This could be an effect of the significant deformation gradient in the net section of the specimens. The maximum net stress value was not affected significantly by loading speed. It is assumed that strain rate does not influence damage development and therefore void volume fraction can be treated as equivalent between NT1 specimens loaded at different speeds.

5.3.2 Data at the microscopic scale

SEM

Figure 5.11 shows the general view of representative fracture surfaces for the NT1 and NT6 geometries. For all specimens, the initiation zone was surrounded by "rivers" (striations), forming a fan-like pattern propagating through the whole fracture surface. No extended fibrils were observed, pointing to a predominantly brittle failure. Numerous dimples could be seen on the fracture surfaces, with dimensions in the order of several microns. These corresponded to voids cut in half due to specimen failure, as confirmed by their symmetric presence on both sides of the fracture surfaces.

A closer observation of the failure initiation sites revealed several types of critical defects. In a single case (Specimen NT1-2), the failure initiated at an unidentified quasi-spherical inclusion, shown in Figure 5.12a. Most commonly, failure initiated at a cluster of voids, such as shown in Figure 5.12b. In many cases, the voids showed signs of coalescence and their dimensions were on average larger than those

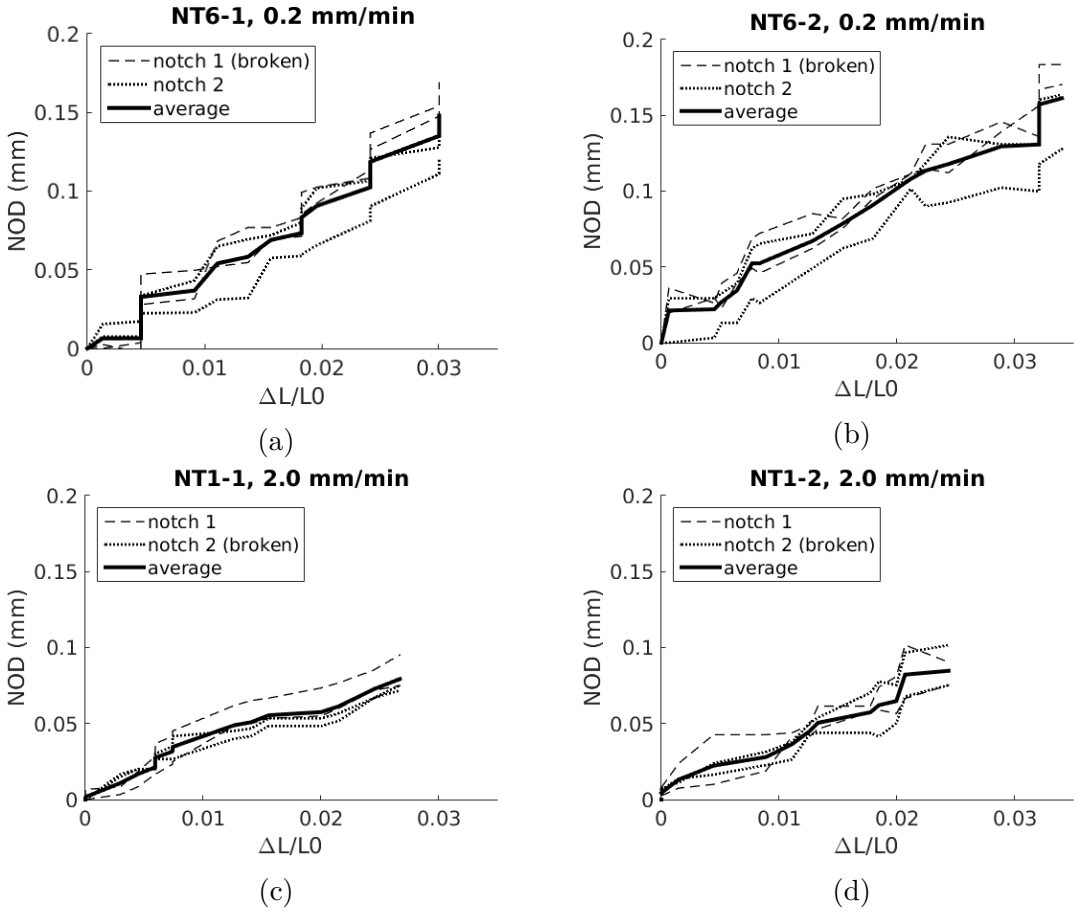

Figure 5.8: Notch opening displacement (NOD) measured from photographs taken in situ. NOD was calculated from the measurements of $a^{(i)}, i = 1, 2, 3, 4$ (see Figure 5.2). The dashed lines correspond to the measurements on either side of one notch, and the dotted lines to those on the other one. The solid line is the average of the four measurements. For NT6, larger deformation was measured in the failing notch, but no such correlation was observed in NT1. **a)** Specimen NT6-1, **b)** Specimen NT6-2, **c)** Specimen NT1-1, **d)** Specimen NT1-2.

measured in tomography observations. This points to significant void growth shortly before failure. Another observed type of a critical defect was a cluster of voids with embedded particles (Figure 5.12c). Energy-dispersive X-ray spectroscopy showed that the spectrum of the particles was very close to that of epoxy, suggesting that they were a result of incomplete polymerization. Generally, critical defects can be described as having an oblate shape, with a diameter of approximately 50 µm and a 5 µm height.

Figure 5.13 shows the location of failure initiation sites for all tested specimens. For NT6 specimens, the initiation sites were consistently located near the specimen

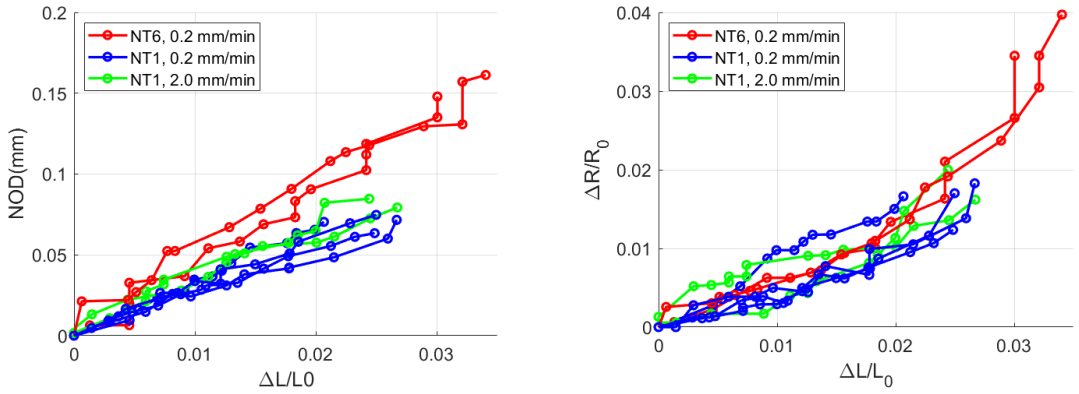

Figure 5.9: Macroscopic measurements: **a)** Notch opening displacement as function of normalized measured displacement. **b)** Radial contraction as function of normalized measured displacement.

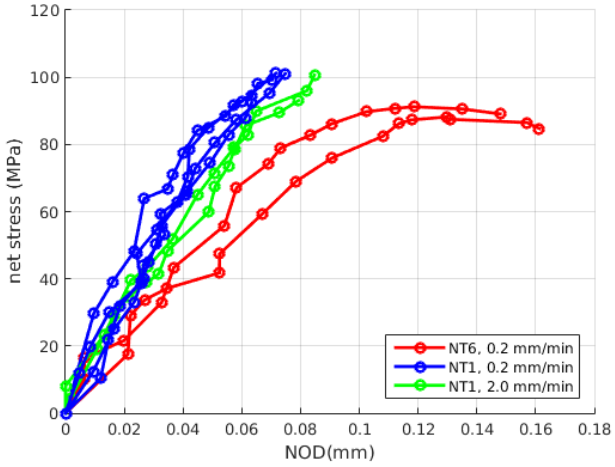

Figure 5.10: Net stress in function of notch opening for NT6 and NT1 specimens.

axis. In turn, the failure of all NT1 specimens initiated significantly off-axis, at approximately 80 % of the maximum net section radius. This shows that notch root radius strongly influences damage development in the specimens. A similar influence of notch geometry was previously observed for semi-crystalline polymers [22].

The stitched SEM images were used to characterize the radial void distribution on the fracture surfaces. Several hundred voids were identified on each mapped specimen and classified as detailed in Section 5.2.3. The measured Feret diameter of the voids was typically between 1 µm and 20 µm.

Figure 5.14 shows the void area fraction with respect to the normalized radius

in NT6 specimens, measured along three radial paths. The radius was normalized by the radius of the gauge section ($R_{max} = 3.5\,\mathrm{mm}$). This was done to account for the fact that voids formed during the curing process, before the notches were machined. The void fractions calculated in the SVOIs are marked with open circles and those on the same radial path are connected by a dashed line. The thicker solid curve is a manually fitted trend line, highlighting the observed tendencies, together with the associated large scatter band. For both specimens, void fraction reached its maximum near the axis of the specimen, in the vicinity of the failure initiation sites.

For the NT1 specimens, void distribution shown in Figure 5.15 was distinctly different than for NT6. Highest void fraction was mostly present near the edge of the specimen, at around 80 % of the net section radius, or approximately $0.6R_{max}$. Analogously to the NT6 geometry, the highest void fraction was located close to the failure initiation site. This provides proof of fast void growth in the last stage before specimen failure.

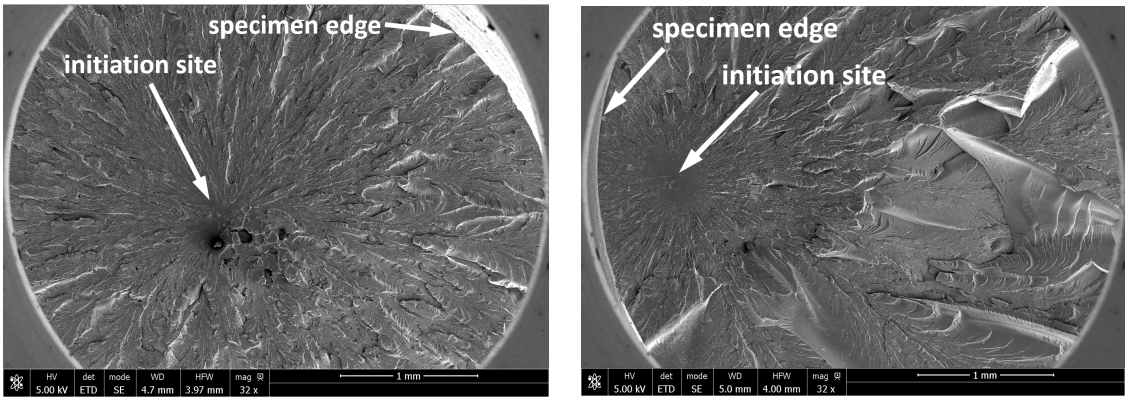

(a) (b)

Figure 5.11: SEM: general view of the fracture surfaces showing the different site of initiation dependent on the geometry. **a)** Specimen NT6-2, **b)** Specimen NT1-1.

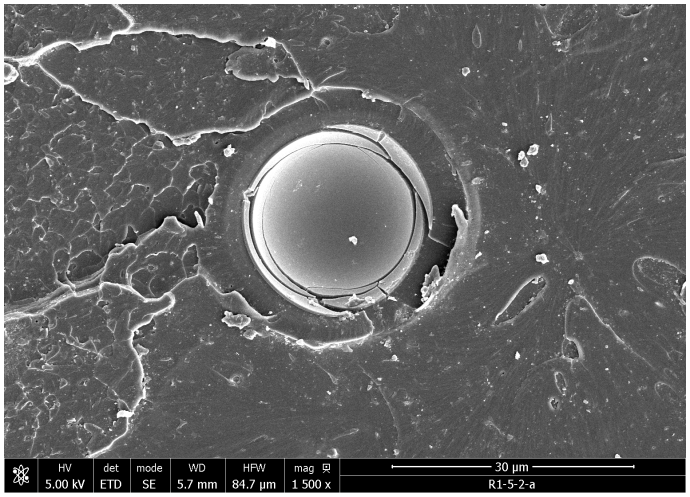

(a)

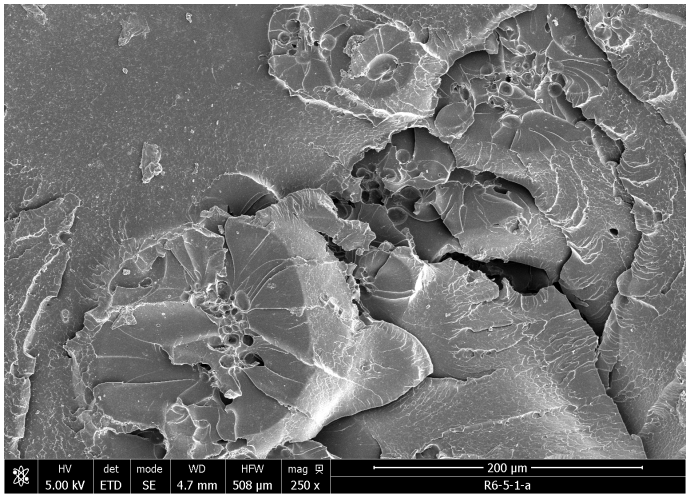

(b)

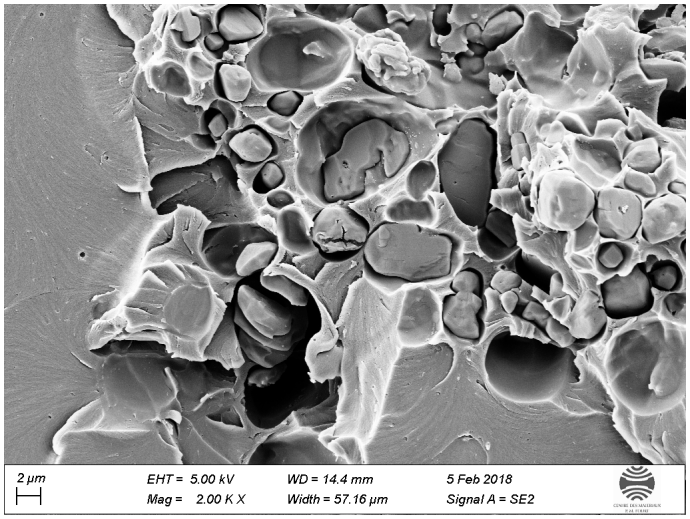

(c)

Figure 5.12: SEM images of fracture initiation sites: **a)** unidentified inclusion (Specimen NT1-2), **b)** void cluster (Specimen NT6-1), **c)** cluster of voids with particles inside (Specimen NT1-3).

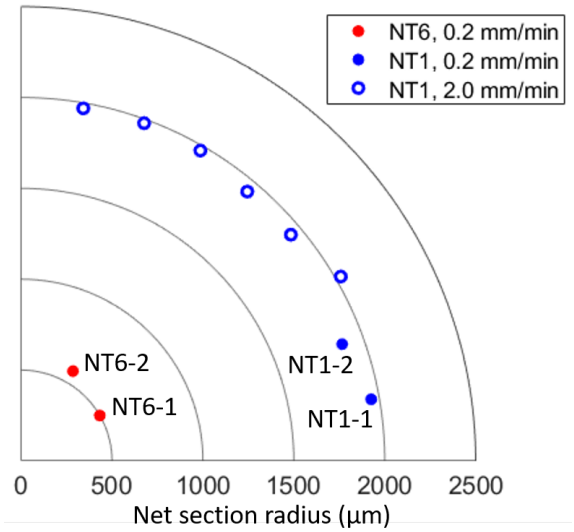

Figure 5.13: Radial positions of the failure initiation loci. Each data point corresponds to one specimen. Indicated with their references are the specimens for which SEM and SRCT results are presented.

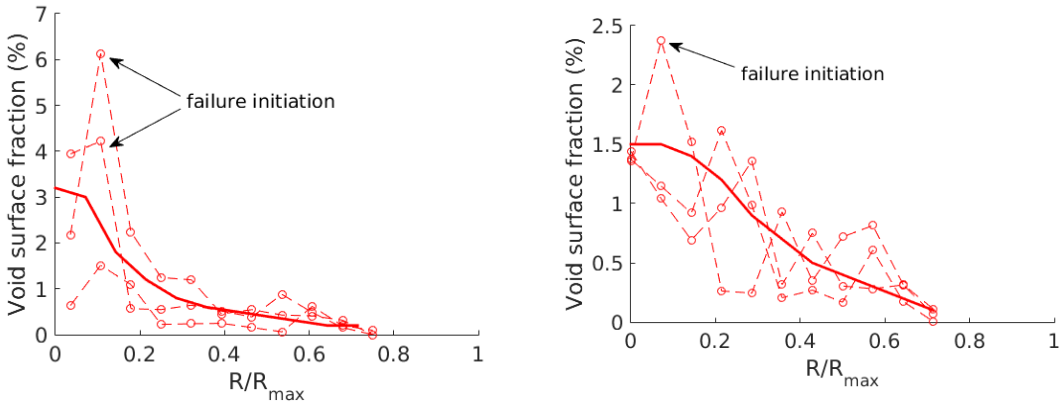

Figure 5.14: SEM: radial void fraction distribution in the net section measured after failure. **a)** Specimen NT6-1, **b)** Specimen NT6-2. N.B. the y-axis range is different in the two plots to simplify the comparison of void growth tendencies between the specimens.

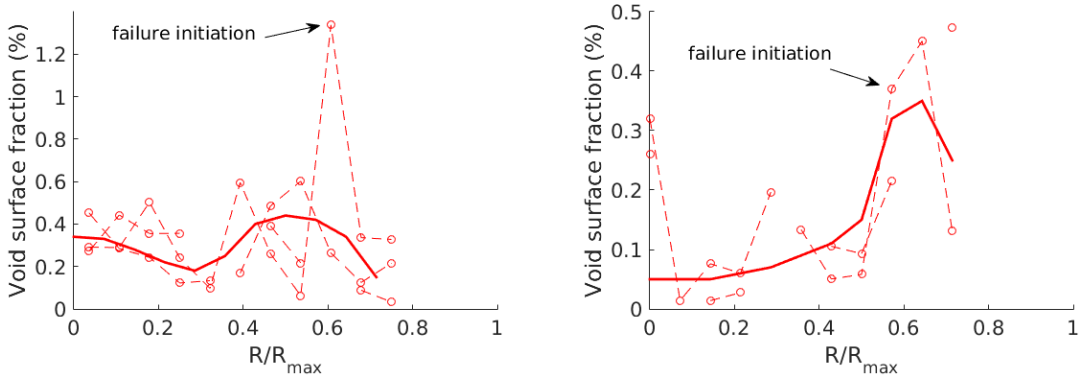

(a) (b)

Figure 5.15: SEM: radial void fraction distribution. **a)** Specimen NT1-1, **b)** Specimen NT1-2. N.B. the y-axis range is different in the two plots to simplify the comparison of void growth tendencies between the specimens.

SRCT

Similarly to SEM observations, SRCT revealed a presence of numerous microscale level voids inside the epoxy specimens. On average, almost 12 000 voids were identified inside a single TVOI. Observed void dimensions were mostly in the order of 1 µm to 10 µm and their shapes were predominantly close to spherical. Clusters of voids were commonly observed. Figure 5.16 shows an example of an SVOI with voids visualized as particles.

The SRCT data paired with SEM results allow plotting the radial distribution of void volume fraction at three consecutive stages:

1. *initial state*, corresponding to the SRCT results outside the notch, as discussed in Section 5.3.1
2. *in the net section shortly before failure* - SRCT at the notch
3. *after failure*, obtained through SEM fractography

Figure 5.17 compares the evolution of void volume fraction (in blue) and void number (in red) for a specific, but representative, case of NT6-1. A shift can be observed from the dashed blue line (stage 1) to the solid blue line (stage 2). This shift does not appear for the red lines. It can be concluded that there is no void nucleation between the two recorded states and the increase in void volume fraction is uniquely due to the growth of pre-existing voids.

For specimens NT6-2 and NT1-2, no tomography data were gathered outside the notch due to limited synchrotron beam time and so only the stages 2 and 3 of the void evolution are available. Figures 5.18 and 5.19 show the evolution of radial void fraction through these three stages in the four studied specimens. Open square markers indicate initial void fraction values measured from the SRCT volumes. Open circles correspond to the SRCT measurements in the net section. Fitting lines are added for both the initial (dashed blue line) and the intermediate state (solid blue). For SEM, discussed in more detail in the previous section, the individual experimental points are omitted this time and only the fitting line is shown. The coordinates of the failure initiation sites are marked with arrows. Void fractions measured via SEM are much higher than those from SRCT. This can be explained by several factors, such as void growth in the broken notch shortly before failure and the closing of voids in the unbroken notches after unloading. Finally, the elliptical form of many voids observed in fractography together with the area measurement based on the maximum Feret diameter can lead to an overestimation of a void's cross-sectional area. To make the comparison between SEM and SRCT easier, the SEM results are shown on a separate scale (right hand y-axis). Below, an interpretation of the results is presented for each specimen.

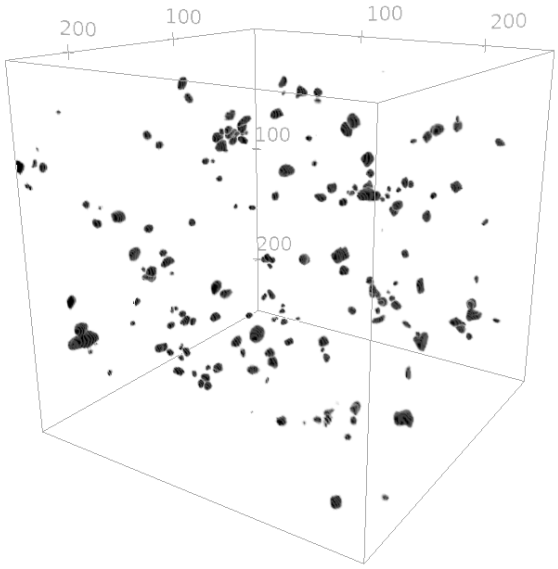

Figure 5.16: Example of three-dimensional void distribution inside an SVOI. The SVOI is a cube with a 250 µm edge.

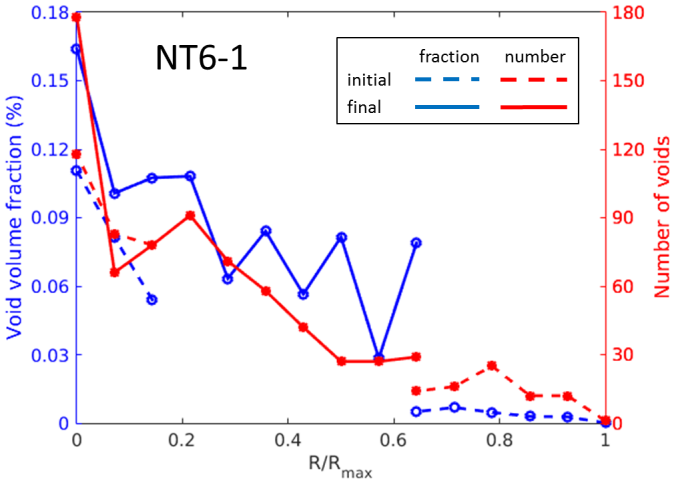

Figure 5.17: SRCT: comparison of void volume fraction vs void number in the initial stage and in the notch. The number of voids does not differ significantly between the two states, while the void volume fraction is clearly higher in the notch, indicating void growth.

Specimen NT6-1 (Figure 5.18a) One radial path was considered both at the net section and outside the notch. No TVOIs were obtained outside the notch for $0.2 \leq R/R_{max} \leq 0.6$. At both stages, a clear gradient of void volume fraction is present, with highest values observed near the axis of the specimen. This gradient

is principally due to a higher number of voids inside some SVOIs and not their larger dimensions. At the notch, the void fraction is consistently higher at all radial coordinates in comparison with the initial state. This increase is due the larger void volumes at the notch, while the difference in the number of voids per SVOI is minor.This indicates that the main responsible mechanism is void growth and not nucleation. SEM fractography results show a similar curve to SRCT, with highest void fraction near the specimen axis, in particular around the failure initiation site.

Specimen NT6-2 (Figure 5.18b) As mentioned previously, only stages 2 and 3 of void evolution are available for this specimen. At the notch, two radial lines were mapped using SRCT data, spanning the whole diameter of the specimen. The radial void fraction gradient is visible in this specimen too, although with a plateau near specimen axis, not observed for NT6-1. This is explained by a more uniform distribution of the voids inside the SVOIs. SEM fractography shows a similar void fraction evolution as in NT6-1: maximum void area fraction is observed near the axis of the specimen, as was also observed in semi-crystalline polymers [22].

Specimen NT1-1 (Figure 5.19a) Initial void distribution is not uniform. Void fraction is highest near the specimen axis, with a similar gradient to that of Specimen NT6-1. SRCT results in the net section show two areas with significant difference from the initial state. Firstly, the void fraction near the specimen axis is higher. The number of voids is also significantly higher there, so this difference is regarded as being caused by the initial porosity scatter. A second area of increased void volume fraction is located close to the net section edge ($0.4 \leq R/R_{max} \leq 0.7$). In that case, the increased porosity results from a higher average void volume, indicating void growth. Void fraction measured from the SEM images is higher than that from SRCT, although the difference between the two is lower than in the NT6 specimens. This indicates a lower intensity of the void growth process, which is consistent with the lower measured radial reduction, as discussed in Section 5.3.1. As mentioned in Section 5.3.2, fracture surface observations revealed the highest void fraction at approximately $0.6R_{max}$. This shows that the smaller notch root radius causes the void growth to occur predominantly away from the axis of the specimen, as also observed for semi-crystalline polymers [22].

Specimen NT1-2 (Figure 5.19b) No initial void fraction data were collected for this specimen. Both for the net section SRCT and SEM fractography results, the void fraction values are the lowest recorded for all specimens. Compared to the other specimens, the SRCT scans show fewer voids. The homogeneous void distribution at the net section is probably due to a uniform initial distribution in that region. The passage from notch SRCT to SEM shows that most void growth takes place at a similar location as for the Specimen NT1-1 discussed above

$(0.4 \leq R/R_{max} \leq 0.7)$. In this case, failure initiated at an unidentified inclusion, as discussed in Section 5.3.2.

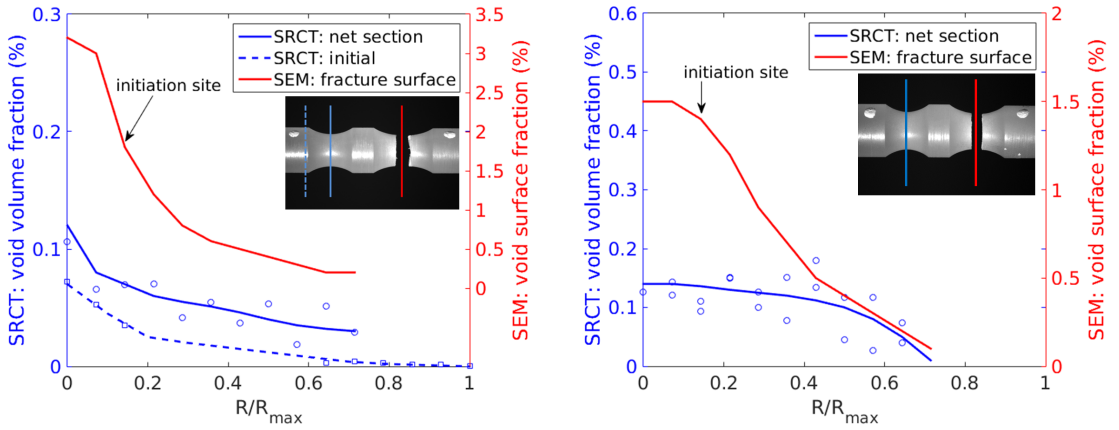

Figure 5.18: NT6 radial void volume fraction evolution. **a)** Specimen NT6-1, **b)** Specimen NT6-2. N.B. the y-axis range is different in the two plots to simplify the comparison of void growth tendencies between the specimens.

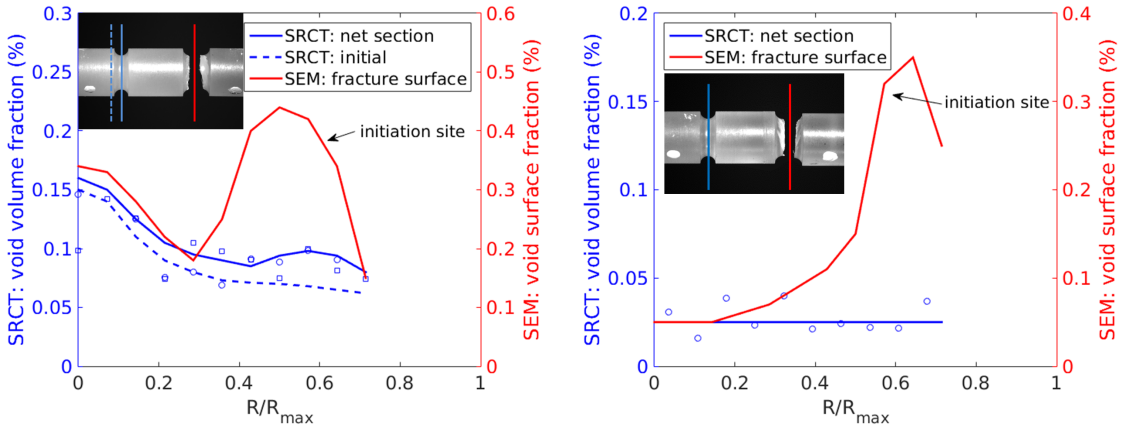

Figure 5.19: NT1 radial void volume fraction evolution. **a)** Specimen NT1-1, **b)** Specimen NT1-2. N.B. the y-axis range is different in the two plots to simplify the comparison of void growth tendencies between the specimens.

5.3.3 Finite element modelling

Inverse optimization All finite element calculations were performed using an in-house finite element code Z-Set [6]. A built-in routine was used to calibrate the model coefficients using the inverse optimization method. Initial void volume fraction was set to be homogeneous at 0.05 %, in the order of magnitude observed experimentally as seen in Figures 5.18 and 5.19. The values of E and ν were determined experimentally at 3400 MPa and 0.42, respectively. The values of $q_1 = 1.0$ and $n = 2.0$ were fixed arbitrarily in advance. The optimization process took into account both macroscopic and microscopic data. At the macroscopic scale, optimization on load with respect to NOD (not the cross-head displacement) gave several sets of possible coefficients. The experimental points were sampled from two NT6 and from four NT1 specimens. When comparing the location of the maximum void volume fraction locally, the best corresponding set of material parameters was selected. It should be pointed out that in this procedure, the initial void volume fraction was considered to be homogeneous. Therefore, specimens with an approximately uniform initial void volume fraction were used for the comparison, i.e. NT6-2 and NT1-2. The optimized values of the GTN coefficients are presented in Table 5.1.

Table 5.1: Optimized coefficients of the GTN model.

E	ν	$\mathcal{R}_0$	Q	b	q_1	q_2	K	n
3400 MPa	0.42 -	15 MPa	58 MPa	500 -	1.0 -	1.6 -	440 MPa	2.0 -

The calibrated numerical model shows a good match for both the macroscopic and microscopic curves. The comparison of numerical and experimental curves of net stress vs NOD is presented in Figure 5.20. The simulation captures successfully the higher stiffness of NT1, as well as the stress softening in NT6. The simulated radial void volume fraction in the net section for an initially uniform distribution of 0.05 % is plotted in Figure 5.21. Void volume fraction evolution shows a good qualitative agreement with the experiments, with most growth at the specimen axis for NT6 and near the net section edge for NT1.

Non-uniform initial void volume fraction The initial void volume fraction observed experimentally in specimens NT6-1 and NT1-1 was not uniform. Therefore, a simulation was carried out with a linear radial gradient of void fraction changing from 0.10 % at the axis of the specimen to 0.05 % at the edge of the net section. For this case, the simulated void volume fraction in the net section at failure is shown in Figure 5.22. Fastest void growth takes place in the same regions as for the

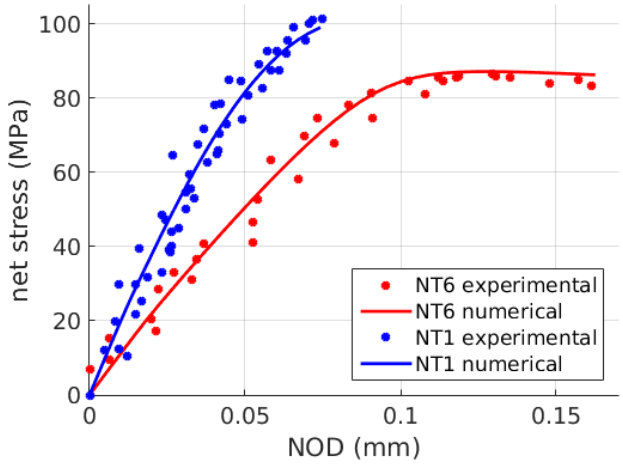

Figure 5.20: FEM: Net stress as a function of notch opening displacement for NT1 and NT6 geometries. Displacement speed: 0.2 mm/min. Comparison with experimental results.

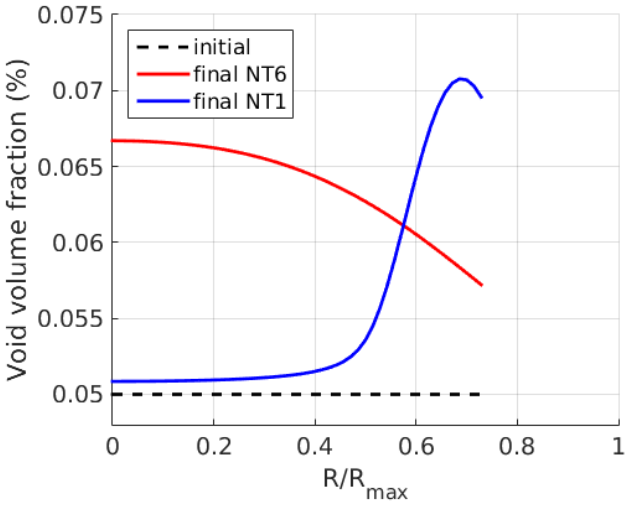

Figure 5.21: FEM: void volume fraction in the net section of an NT1 and an NT6 specimen at failure. Uniform initial void fraction of 0.05 %.

uniform initial porosity case. However, the maximum value of void volume fraction is significantly higher for NT6, since the area of maximum void growth is also that of the maximum initial void fraction. This agrees with the experimental results, where NT6 specimens showed higher void fractions overall than NT1. The results show a good agreement with the experimental void distribution plotted in Figure 5.18a and Figure 5.19a. It is worth noting that for NT1-1, void volume fraction experiences the fastest growth near the notch root radius, while the maximum void volume fraction

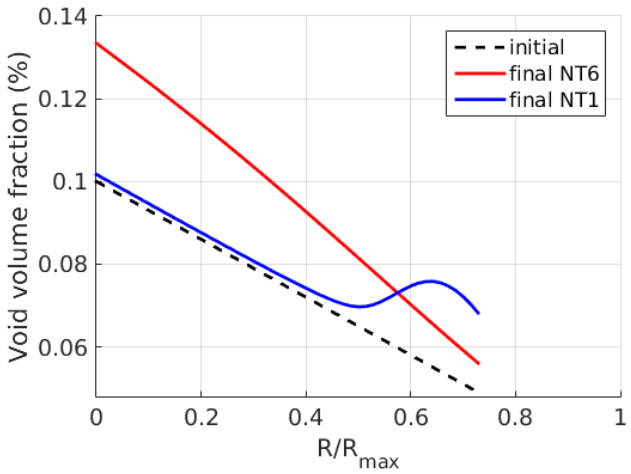

Figure 5.22: FEM: void fraction evolution in the net section of an NT1 and an NT6 specimen, given an initial porosity gradient. $R_{max} = 3.5\,\text{mm}$.

is located close to the specimen axis. This effect is captured numerically.

Stress distribution The GTN model based on the mechanics of porous media allows computing the stress tensor at the local scale, homogenizing the epoxy and the voids into a single continuum. Figures 5.23 and 5.24 show the computed contour maps of hydrostatic pressure and the maximum principal stress in the NT6 and NT1 specimens, respectively, obtained for a uniform initial void volume fraction of 0.05%. For a given specimen geometry, the location of the maximum hydrostatic pressure is the same as that of the maximum principal stress. However, there are differences between the two geometries. For NT6, the maximum values of stress are present at the centre of the specimen. For NT1, the maximum is located in the proximity of the net section edge. The maximum principal stress is always greater than hydrostatic pressure, which agrees with the fact that the maximum principal stress is roughly equal to the sum of hydrostatic pressure and the shear stress represented through the equivalent von Mises stress [15]. It should be noted that the hydrostatic pressure is the stress related to the volumetric strain which is affected by void growth.

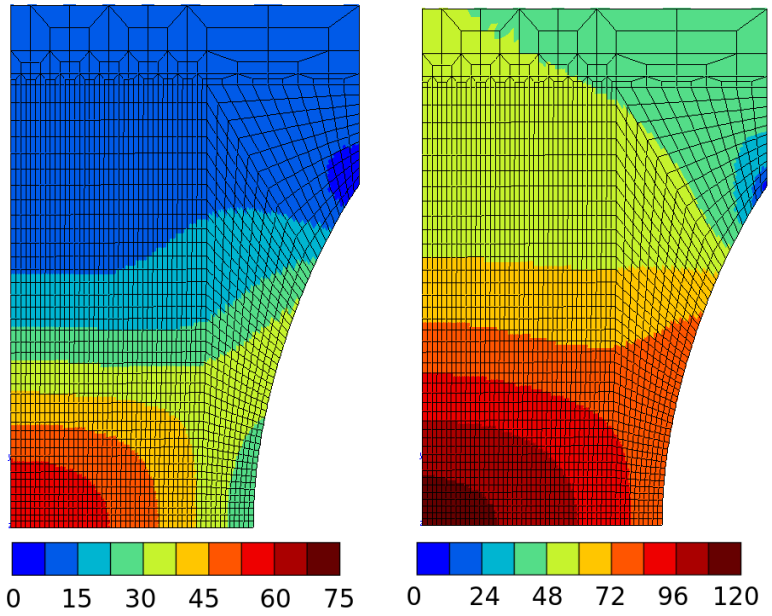

(a) (b)

Figure 5.23: FEM: stress contour map (MPa) at failure in the NT6 specimen. a) hydrostatic pressure, b) maximum principal stress.

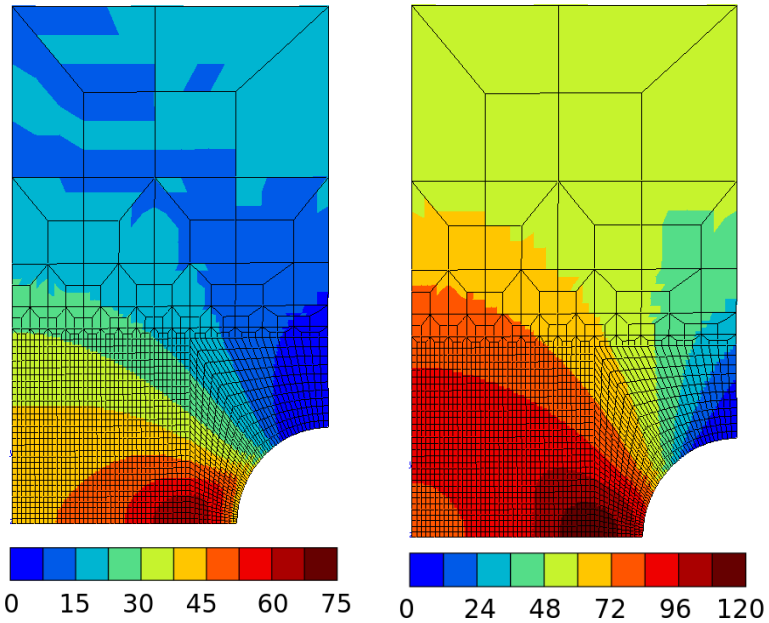

(a) (b)

Figure 5.24: FEM: stress contour map (MPa) at failure in the NT1 specimen. a) hydrostatic pressure, b) maximum principal stress.

Failure criterion As mentioned earlier, radial void distribution in the net section of specimen NT1-1 is of particular interest. While the fastest void growth takes place close to the edge of the specimen, maximum void volume fraction at failure is recorded at the axis of the specimen. This highlights that unlike for semi-crystalline polymers, a critical value of void fraction cannot be used as a failure criterion. For brittle materials, such as the epoxy studied, a more appropriate criterion would be based on the existence of a critical defect in a region where the stress is greater than or equal to a critical value. The failure criterion can be further investigated by looking at the radial distribution of the maximum principal stress in the net section shown in Figure 5.25, together with the locations of the critical defects as shown in Figure 5.13. It can be seen that the initial void distribution has a minor influence on the predicted stress magnitude and distribution. The shaded regions in the figure indicate the range of radial coordinates of the critical defects that triggered the brittle failure. It can then be concluded that the critical maximum principal stress is approximately 110 MPa.

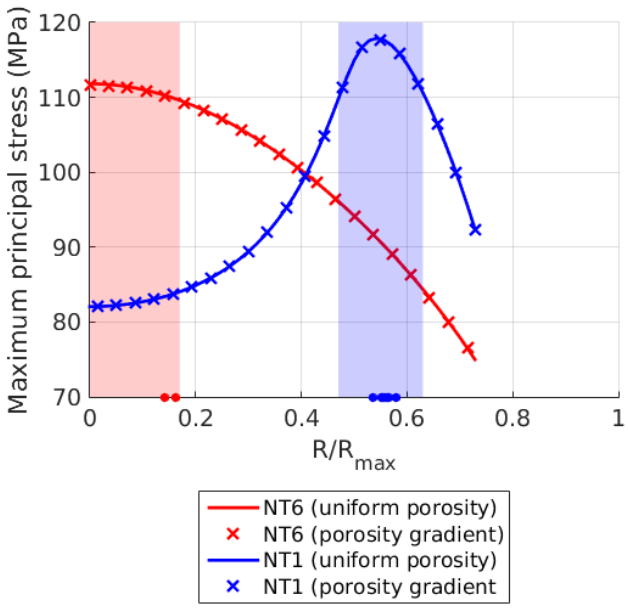

Figure 5.25: FEM: main principal stress in the net section at failure. The dot markers correspond to experimentally observed failure initiation sites for NT6 (red) and NT1 (blue). The shaded areas indicate regions where a critical defect can coincide with a critical stress for the respective geometries, leading to failure.

5.4 Conclusions

The study presented in this article aimed at quantifying void growth inside a thermosetting epoxy resin and improving the understanding of the damage processes taking place. To this end, double-notched round bars with two different notch root radii were manufactured and tested in tension. Afterwards, the fracture surfaces were observed via SEM, while the unbroken notches were scanned using SRCT. The combination of both techniques allowed the assessment of void growth at different stages of damage. Void position and size were measured and a Statistical Volume of Interest (SVOI) was defined to evaluate void volume fraction distribution. An initially non-uniform void distribution was observed in most cases. The comparison of consecutive stages of damage development allowed areas exhibiting most void growth to be identified. For NT6 specimens, those were near the specimen axis, whereas for NT1 they were located at approximately 80 % of the maximum net section radius. The failure originated at a critical defect: a cluster of voids, a cluster of particles and in one case at an unidentified inclusion. The dependence of failure initiation location on notch root radius highlights the sensitivity of the material to multiaxial stress states.

The experimental observations at the macro- and the microscale were used to calibrate a numerical model of the epoxy, using a Gurson-Tvergaard-Needleman (GTN) constitutive law. The simulations predicted the highest values of the maximum principal stress in the areas where failure initiation was observed experimentally. The GTN model was shown to be an appropriate choice for modelling an amorphous polymer, being able to handle low initial void fractions ($\approx$ 0.1%) and non-uniform void distributions. A critical void fraction was determined not to be a suitable failure criterion for a thermosetting polymer. A different criterion was proposed, based on a combination of a critical value of the maximum principal stress and the presence of a critical defect.

The results presented highlight the significance of multiaxial stresses in the failure of polymeric materials. The finite element model can be applied to model epoxy matrices, commonly used in high-performance fibre-reinforced composites. This would improve the understanding of the mechanical response of these materials at the microscale, where the polymer can be subjected to a highly multiaxial stress state. Furthermore, by quantifying the probability of a critical defect presence in the material, a stochastic model can be built, accounting for the scatter of failure initiation sites and net stress in the notched specimens.

Chapter 6

Effect of macroscopic voids and through-thickness compression on the tensile strength of a carbon-epoxy composite

Chapitre 6. Effet des cavités macroscopiques et de la compression à travers l'épaisseur sur la résistance en traction d'un composite carbone-époxy

Les dimensions importantes ainsi que le risque posé par les applications industrielles qui utilisent des hautes pressions présentent un défi dans l'étude de la rupture des réservoirs à fibres de carbone. Ainsi, tout phénomène susceptible de dégrader les propriétés, notamment à rupture, d'un réservoir, doit être analysé. Le phénomène de porosité fait partie de ces phénomènes. Toutefois, au préalable d'une prise en compte sur une structure, l'analyse sur le matériau lui-même doit être faite. Ici, il s'agit donc d'étudier le phénomène de porosité présent au sein d'un composite unidirectionnel.

Une étude expérimentale sur la résistance d'un matériau composite à différents taux de porosité est présentée. Le matériau est sollicité en traction longitudinale et en compression dans le sens de l'épaisseur. Cette sollicitation biaxiale imite l'état de contraintes présent dans un réservoir composite à parois épaisses.

Les essais mécaniques ont été menés sur des éprouvettes d'un stratifié à plis croisés, avec une séquence d'empilement $[0/90_2/0]_{2S}$. Le point important à souligner ici est que ces séquences d'empilement ont été élaborées, en autoclave, de telle sorte que l'on impose la porosité : d'abord, un composite à un taux de porosité faible a été obtenu en suivant un cycle de durcissement recommandé, ensuite, un composite à taux de porosité élevé a été obtenu en réduisant la pression de durcissement.

La première sollicitation considérée est la traction uniaxiale. Pour le composite à taux de porosité élevé, les résultats montrent une réduction du module d'Young, ainsi que de la contrainte à rupture d'environ 5 %. En même temps, la déformation à rupture reste pratiquement identique pour les deux matériaux. On en conclut que la résistance en traction d'un composite carbone-époxy est peu sensible au taux de porosité.

Les essais biaxiaux (traction plus compression dans le sens de l'épaisseur) ont été réalisés sur une machine de traction standard, à l'aide d'un système de compression spécialement conçu et fabriqué. La compression a été appliquée localement par des indenteurs cylindriques en acier. Trois niveaux différents de compression ont été testés pour les deux types de matériau.

Toutes les éprouvettes se sont cassées entre les indenteurs et leur surface de rupture était typique d'une rupture en traction dominée par les fibres. L'état de contraintes locale au moment de rupture a été calculé par la méthode d'éléments finis. Les sollicitations externes dans la simulation correspondaient à leur valeur moyenne mesurée expérimentalement. En vue d'expliquer le mode de défaillance en traction, la valeur de la contrainte longitudinale dans les plis à 0 degrés est particulièrement intéressante. Pour des valeurs faibles de la compression, les valeurs de la contrainte à rupture longitudinale sont peu différentes de celles calculées pour les essais en traction. Cependant, pour des valeurs de compression plus élevées, une réduction de cette valeur à rupture est observée. En plus, la présence des porosités cause une réduction de la résistance du matériau pour tous les niveaux de compression. Ces résultats montrent qu'un critère de rupture uniaxial est susceptible de surestimer la résistance en traction d'une structure sollicitée en même temps en compression dans le sens de l'épaisseur, tel comme est le cas dans un réservoir à parois épaisses.

6.1 Introduction

The large dimensions and safety risk posed by high pressure present a significant challenge in testing composite pressure vessels and monitoring damage development taking place at the microscale. Tests on smaller representative specimens allow studying the damage phenomena in composites in more detail. In the last phase before tensile failure of CFRPs, damage becomes localized through a formation of fibre break clusters, as discussed in Section 1.2.3. Therefore, failure of a larger composite structure can be predicted by analyzing the critical stress state, understood as the local stress state that leads to damage localization and structural failure. Figure 6.1 shows the computed stress state in the thick-walled cylinder that was analyzed in Chapter 4. The details of the finite element simulation are presented in Appendix B. From the stress state, it can be concluded that the burst pressure is controlled by the strength of the first (innermost) hoop ply. The stress state in that ply is multiaxial, with the first and second highest stress component being longitudinal tension and through-thickness compression, respectively. As demonstrated in Chapter 4, composite pressure vessels may contain a high void content. This leads to the conclusion that *the failure of a pressure vessel takes place under a combination of longitudinal tension and through-thickness compression, in a material with a significant number of macroscopic voids*. Biaxial tests are necessary to generate these conditions in representative specimens.

Testing of fibre-reinforced composites under multiaxial stress conditions and predicting their strength is still an open problem and the existing failure theories often struggle to provide reliable predictions [62] [152]. Multiaxial stresses, similar to those described above, have received some attention in the literature. Several authors have studied the influence of hydrostatic pressure on the longitudinal tensile strength of CFRPs. Parry and Wronski [116] observed a decrease in tensile strength for an increase in hydrostatic pressure. Zinoviev et al. [180] observed a non-linear relationship, with the hydrostatic pressure causing initially an increase in tensile strength, and then a decrease for higher hydrostatic pressure values. However, when fibre breakage was the dominant failure mode, a relationship similar to that of Parry and Wronski was observed. Hine et al. reported a decrease in tensile strength with hydrostatic pressure for both carbon and glass fibres [61]. Other authors observed a similar trend for aramid [179] and glass fibres [117] [143].

A second group of existing studies analyzes the longitudinal tensile strength in the presence of transverse compression. Gan et al. [47] proposed a biaxial test method, consisting of locally applying through-thickness compression to specimens subsequently loaded to failure in tension. The results showed a decrease in tensile strength under these conditions. The same tendency was observed by Goto et al. [48], who carried out biaxial tests on a custom-designed setup compatible with a standard tensile rig. Rev et al. observed a decrease in the ultimate strain of a unidirectional

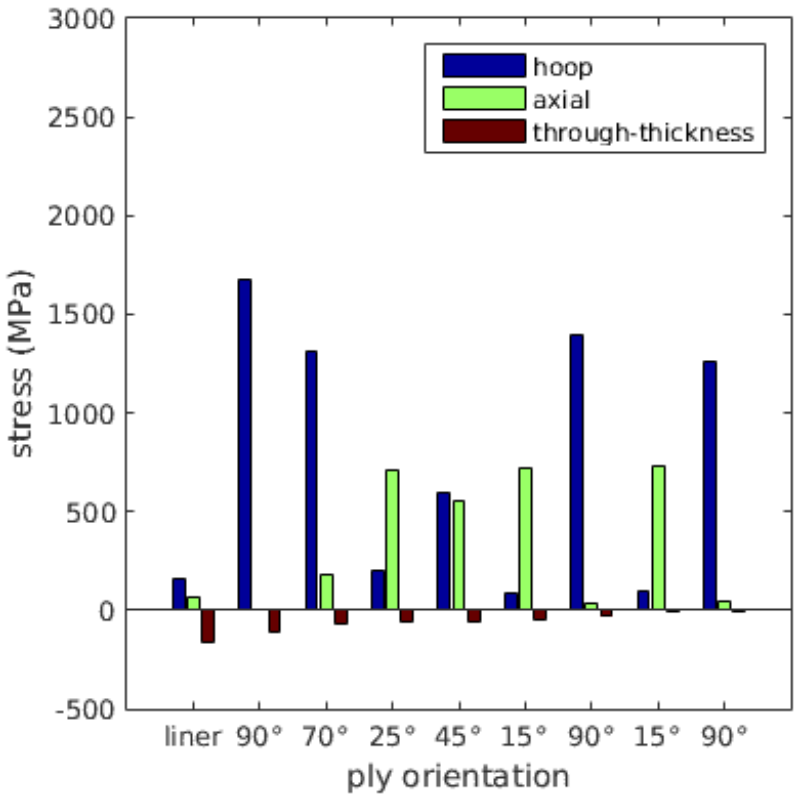

Figure 6.1: Computed stress components in the thick-walled pressure vessel analyzed in Chapter 4, obtained through finite element analysis.

CFRP in the presence of transverse compression [130].

Little is known on the effect of voids under conditions similar to those described above. In this chapter, an experimental study is presented, with the objective of evaluating the tensile strength of a carbon fibre-reinforced composite subjected to through-thickness compression and containing a significant amount of macroscopic voids. First, the material manufacturing procedure is described. Curing cycle is controlled to modify void volume fraction. A material with a high void content is obtained. By testing it and comparing the results with a reference low voidage material, the effect of voids on the mechanical properties can be evaluated. Two loading cases are considered: 1) in-plane tension and 2) in-plane tension with out-of-plane compression. The latter case is chosen to mimic more closely the stress state in a thick-walled cylinder. A custom experimental setup is designed for testing of composites under biaxial conditions. The test method proposed by Gan et al. [47] is used to study the effect of through-thickness compression on the tensile strength of carbon-reinforced composites.

6.2 Material manufacturing - void content control

The material used in this study is an aerospace-grade unidirectional carbon-epoxy prepreg tape HexPly 6376C-HTS(12K)-5-35%. Square 300 mm × 300 mm plates with a stacking sequence $[0/90_2/0]_{2S}$ are prepared through manual layup. After being placed on the stack, each ply is manually rolled to avoid excessive air entrapment between plies. The cross-ply geometry is chosen to avoid failure through fibre splitting under transverse compression. Constraining the transverse displacement has been shown to change the failure mode to fibre-dominated and thus significantly increase the through-thickness compressive strength of carbon fibre composites [35] [114].

The laminates are autoclave-cured, with an aluminium caul plate placed on top. To study the influence of voids on the strength of carbon fibre-reinforced composites, specimens with different levels of void volume fraction are manufactured. This is achieved by modifying curing cycle parameters. Low curing overpressure is known to result in an increased void content in composites [147] [113] [76] [146]. The first batch of plates is processed using the curing cycle recommended by the prepreg supplier, resulting in a material with a low void content. The nominal parameters of the cycle are shown in Figure 6.2. A temperature of 175 °C is held for 150 min, before starting the cool-down phase. Additionally, a 7 bar overpressure and vacuum are applied. The laminates produced with this cycle are referred to as low voidage or reference laminates. A second batch of plates is manufactured with a modified curing cycle, in order to obtain a high voidage material. The duration of curing and the temperature profile remain the same as in the nominal cycle. Vacuum is maintained through the whole cycle, but no overpressure is applied.

Rectangular specimens of dimensions 250 mm × 10 mm are cut out from the plates using a water-cooled diamond wheel cutter. The specimens are obtained at least 25 mm from the plate edge. The average measured thickness is 2.14 mm for the reference plates and 2.20 mm for the high voidage plates. Glass-epoxy end tabs of 60 mm length are used to reduce stress concentrations at the grips of the tensile machine.

Figure 6.3 shows a detail of a microtomography scan from a low and a high voidage specimen. In the former, no cavities are observed. In the high voidage specimen, numerous voids are visible, especially in the central ply, perpendicular to the figure plane. The dominant feature observed in the specimen is the macroscopic voids of an approximately ellipsoidal shape, with the major axis of the ellipsoid oriented in the fibre direction. The voids are qualitatively similar to those in a composite pressure vessel, analyzed in Chapter 4. Therefore, the high voidage specimens can be treated as representative of the composite material in a pressure vessel.

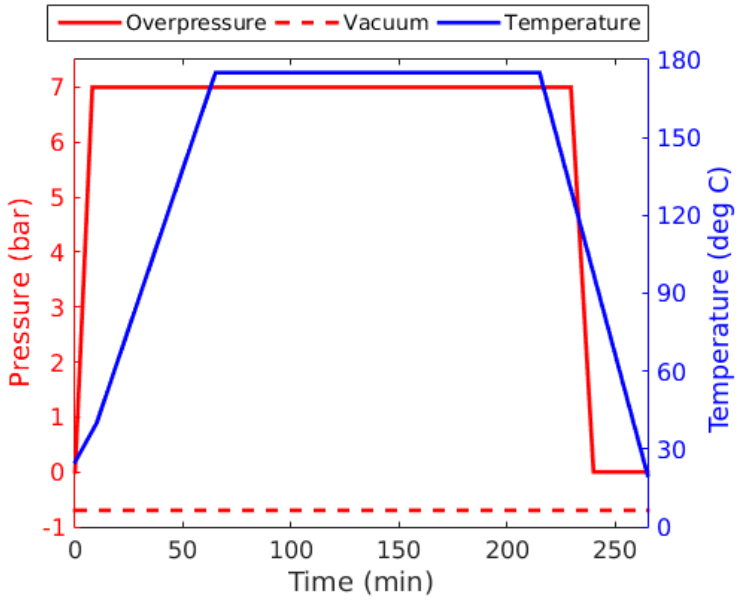

Figure 6.2: The nominal autoclave curing cycle to manufacture the reference material with a low void content. To obtain a high void content material, the cycle is modified: no overpressure is applied, while the temperature and vacuum remain unchanged.

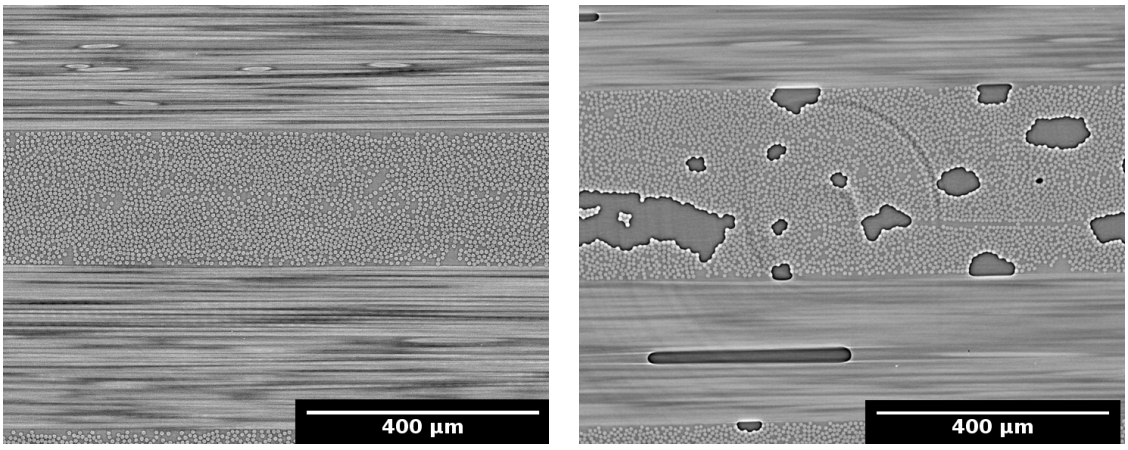

(a) Low voidage specimen.

(b) High voidage specimen.

Figure 6.3: SRCT: low and high voidage specimen. Two orientations of the composite are clearly visible.

Void content in selected specimens is evaluated using optical microscopy. A 30 mm length of the specimens' lateral edge is photographed at a 200× magnification using a digital microscope. The images are then processed in Fiji software. The micrographs are transformed into 8-bit grayscale and individual

images are stitched together. Next, void segmentation is carried out by global grayscale thresholding, using the same method as discussed in Section 4.2.1.

Void fraction is measured only in the plies oriented perpendicular to the image plane, to reduce the sectional bias [51]. At the observed resolution, very few voids are visible in the specimens produced with the reference curing cycle. This confirms that high curing pressure allows evacuating most of the air that would otherwise get trapped inside the laminate. In turn, the high voidage specimens contain numerous large voids. The measured void area fraction can vary significantly between specimens, but it is generally in the order of 5 %.

6.3 Mechanical testing: in-plane tension

The first studied loading case is uniaxial tension. Low and high voidage specimens are loaded until failure on an electromechanical tensile rig at a constant cross-head spead of 1 mm/min. Twelve specimens are tested for each case. Strain is measured for all specimens using a video extensometer. To allow optical microscopy observation of damage development at the meso- and microscale, selected specimens have their lateral free edge polished. The details of damage development in the low and high voidage specimens are presented in Appendix C.

All tested specimens failed in a catastrophic manner. After excluding the specimens which failed near the tensile machine grips, seven low and nine high voidage specimens are used in the result analysis. The test results are summarized in Table 6.1. The mean value and uncertainty are provided for each measured property. The stress-strain curves of both types of specimens are shown in Figure 6.4. The curves are approximately linear, with some stiffening. This behaviour, caused by the reorientation of crystallites in carbon fibres and initial fibre misalignment, has been well described in the literature [39] [163] [70] [142]. To quantify the stiffening, two values of tensile modulus are calculated: initial and final secant modulus. The initial modulus is calculated according to ISO 527-5, for a deformation range between 0.05% and 0.25%. The final secant modulus is calculated by dividing the specimen strength by its final strain.

The strength of the high voidage material is approximately 5% lower, while the ultimate strain of the two materials is virtually identical. The difference in strength and modulus can be partially explained by a lower effective fibre volume fraction of the high voidage specimens, due to the presence of voids in the measured cross section.

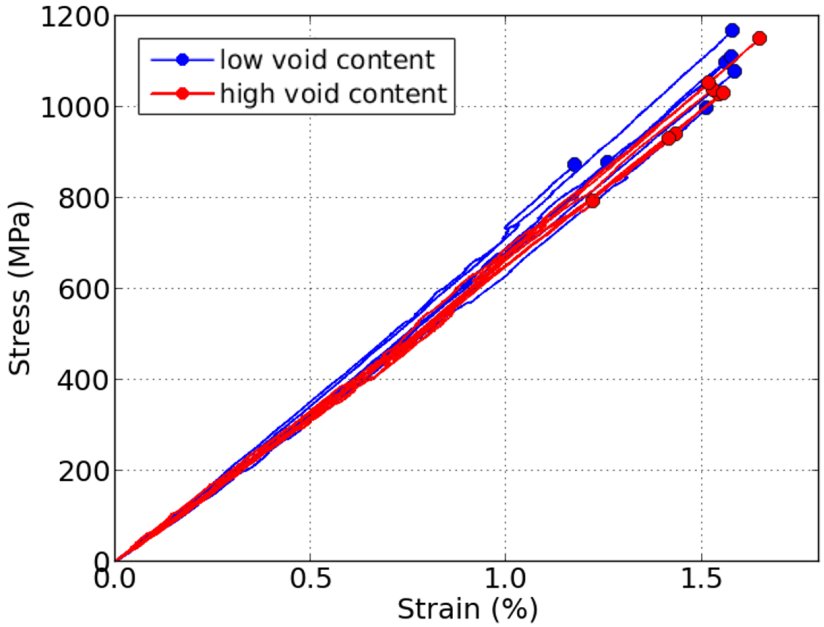

Figure 6.4: Stress-strain curves of tensile tests on the low and high voidage specimens.

	low voidage		high voidage	
	mean	$\pm u_{95}$	mean	$\pm u_{95}$
strength (MPa)	1028	108	995	89
strain (%)	1.47	0.13	1.48	0.11
initial modulus (MPa)	63989	2961	62853	2215
secant modulus (MPa)	70295	2769	66954	1500

Table 6.1: Tensile test results. The results are obtained for 7 low and 8 high void content specimens. The uncertainty u_{95} is given with a 95% confidence interval according to the Student's t-distribution [71].

6.4 Biaxial mechanical testing: in-plane tension and through-thickness compression

6.4.1 Development of the experimental setup

The second loading case is longitudinal tension with through-thickness compression, mimicking the critical stress state in a thick-walled pressure vessel. The testing

procedure is analogous to that of Gan et al. [47]. Rectangular 250 mm × 10 mm specimens are used, identical as in the tensile tests described previously. Figure 6.5 shows the principle of the testing method. A compressive through-thickness load is first applied locally by cylindrical steel indenters with a 10 mm radius. Afterwards, the specimen is loaded in tension. While using flat indenters would allow introducing the desired stress state over a larger region of a specimen, proper alignment and edge effects become a problem for such geometry.

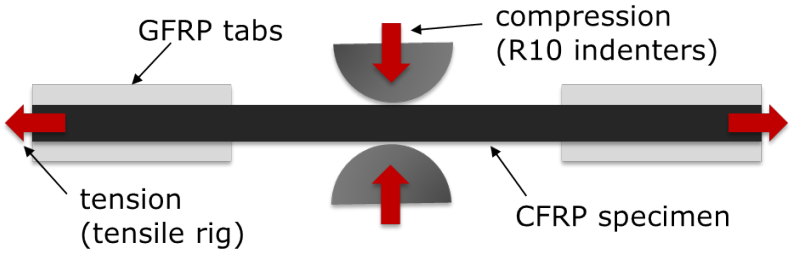

Figure 6.5: Schematic reperesentation of the biaxial test.

Instead of using a biaxial testing rig, a custom experimental setup was designed, allowing the tests to be carried out on a standard uniaxial tensile machine. Through-thickness compression is applied by means of a custom-designed and manufactured setup, using a motorcycle four-piston opposed brake calliper. In this design, two pairs of pistons face each other on the opposing sides of the calliper cavity. Pressure is applied by pumping brake fluid into the calliper, pushing the pistons towards each other. A steel fixture shown in Figure 6.6 was manufactured to transfer the load from the pistons onto the specimen. The fixture consists of two opposing blocks, connected by two guiding rods sliding on linear bearings, ensuring good alignment. The cylindrical indenters are glued to the fixture with an epoxy adhesive.

The compression setup is suspended on a uniaxial tensile machine as shown in Figure 6.7, using four cables passing through pulley blocks. The cables are connected on one side to the calliper and on the other one to counterweights. The combined weight of the counterweights is equal to that of the compression setup. This avoids passing additional loads to the specimen and allows the setup to easily follow the axial displacement of a loaded specimen. To conduct a biaxial test, a specimen is first placed between the indenters. A simple screw-adjustable jig is used to control the initial position of the specimen with respect to the indenters. The bottom end of the specimen is fixed in the bottom grip of the tensile rig, while the top end is left free. Next, the indenters are clamped on the specimen by applying pressure through a hydraulic hand pump, until approximately 15 bar to 25 bar. At that point, the correct alignment of the specimen is checked. The pressure is then raised to the prescribed value by an electric spindle screw pump at a loading rate

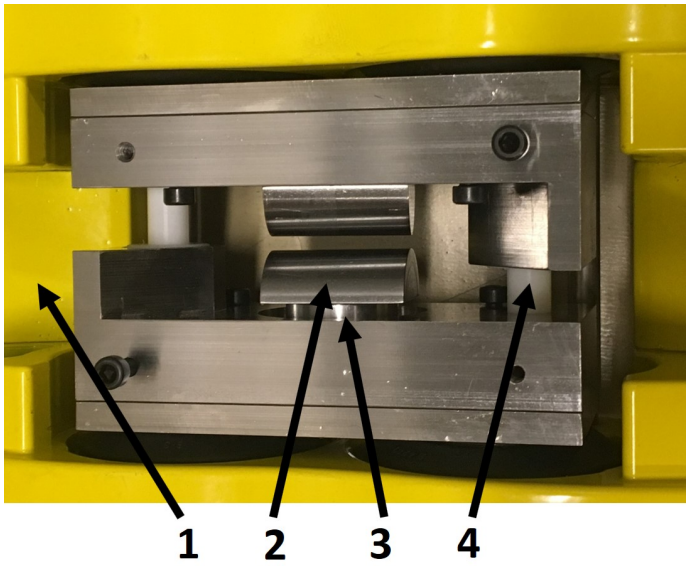

Figure 6.6: Custom-built hydraulic compression system. **1)** Brake calliper housing, **2)** R10 indenter, **3)** load cell, **4)** guiding rod.

of 45 bar/min. After reaching the prescribed level, the pressure is controlled by an electronic feedback loop. Once the pressure level stabilizes, the top end of the specimen is fixed in the tensile machine grip. Finally, the specimen is loaded in tension until failure, at a constant cross-head speed of 1 mm/min.

For both types of material, three applied compression values are tested: 25, 50 and 100 bar. The lateral edge of the specimen between the indenters is photographed at 2 frames per second during a test. From these photographs, the indenter displacement is calculated using in-house image processing software, by cross-correlation analysis of two point markers placed on the indenters. Since the stiffness of steel is much higher than transverse stiffness of the composite, it is assumed that the indenters do not deform. Then, once the indenters come in contact with the specimen, marker displacement can be treated as equivalent to specimen surface displacement. Additionally, a white paint speckle pattern is applied on the lateral edge of selected specimens to study specimen deformation using digital image correlation (DIC). The images are processed in VIC-2D software.

6.4.2 Stress computation by finite element analysis

Ply stresses cannot be evaluated from the macroscopic data and are therefore computed using finite element analysis. The biaxial tests on low and high voidage specimens are simulated using the in-house finite element code Z-Set [6]. The steel

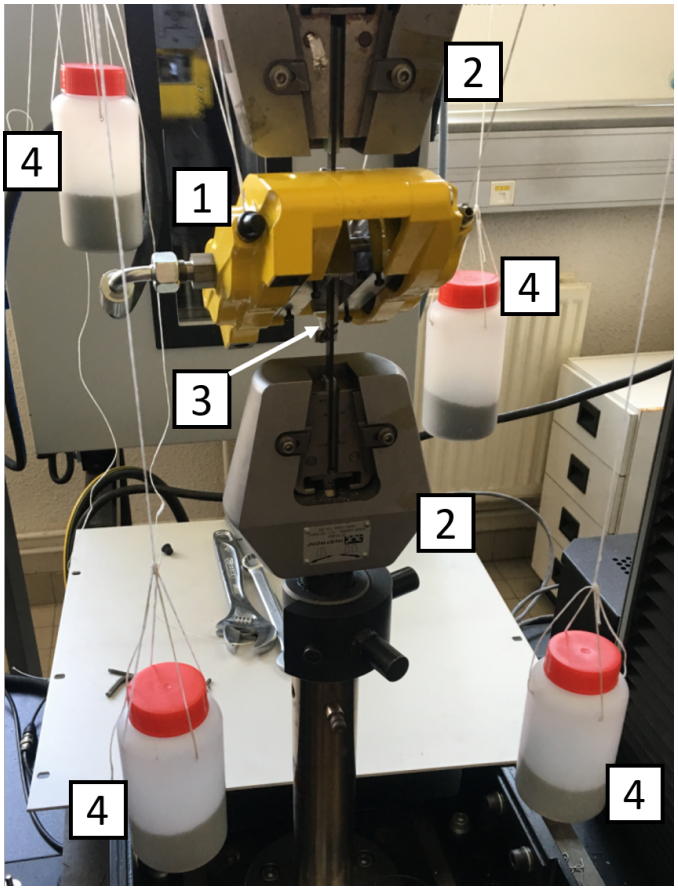

Figure 6.7: Biaxial testing system: compression setup with counterweights mounted on the tensile machine. The calliper is tilted to allow video observation of the lateral edge of the tested specimen. Label: 1) calliper, 2) tensile machine grips, 3) specimen, 4) counterweights.

indenters are modelled using a linear elastic isotropic behaviour, with a Young's modulus $E = 200\,\text{GPa}$ and a Poisson's ratio $\nu = 0.3$. The unidirectional plies of the laminate are modelled as linear elastic transversely isotropic.

The elastic constants of a unidirectional low and high-voidage ply are obtained by homogenizing the constituent properties using the generalized self-consistent scheme, presented later in the thesis (Section 7.2.1). The properties of the constituents are given in Table 6.2. Table 6.3 summarizes the obtained resultant properties of a unidirectional ply. The properties are obtained for a fibre volume fraction of 58% for the low-voidage composite. For the high-voidage specimens, a void content of 5% is assumed. The thickness of the meshed specimen is set to 2 mm for both types of material. To keep the same fibre-to-matrix volume fraction in the high-voidage specimens as in the low-voidage ones, a fibre volume fraction of 61% is used. Some caution is required when interpreting the results obtained with this

homogenized material model for the high-voidage specimens. Since the compression is applied locally and void cross-sections can locally have dimensions in the order of magnitude of ply thickness, the homogenized material assumption may lead to unrealistic predictions.

Fibres: Tenax HTS45		**Resin: HexPly 6376**	
E_{11}	240 GPa	E	3.6 GPa
E_{22}*	8 GPa		
$\nu_{12} = \nu_{13}$*	0.26	ν*	0.35
ν_{23}*	0.3		
$G_{12} = G_{13}$*	27.3 GPa	G*	1.4 GPa

Table 6.2: Elastic coefficients of the fibres and matrix used to derive the homogenized properties of a unidirectional ply. Properties, for which no data were available, are marked with an asterisk. For those, values from comparable materials were used instead.

	V_f	E_{11}	E_{22}=E_{33}	ν_{12}=ν_{13}	ν_{23}	G_{12}=G_{13}	G_{23}
Low voidage (0%)	0.58	140.7	5.9	0.30	0.41	4.4	2.1
High voidage (5%)	0.61	140.4	5.3	0.29	0.40	4.2	1.9
	-	GPa	GPa	-	-	GPa	GPa

Table 6.3: Properties of a UD composite used in the finite element simulation of the biaxial tests.

The indenter-to-specimen contact is modelled using a frictionless formulation. 8-node linear three-dimensional elements (C3D8) are used. The mesh and applied boundary conditions are shown in Figure 6.8. One-eighth of the geometry is meshed, taking advantage of the three symmetry planes. A convergence study is carried out to determine the appropriate element size. The specimen mesh is refined under the indenters and near the lateral free edge, where high stress gradients are present. A minimum element size of 0.05 mm under the indenter was found to be sufficient, with little difference from 0.01 mm. A downward (direction $-\vec{x_3}$) displacement boundary condition is applied on the top surface of the indenter. After reaching the desired load level, a displacement is applied at the end of the specimen in the $\vec{x_1}$ direction.

6.4.3 Results

Mechanical testing All tested specimens broke between the indenters and the fracture surface was mostly flat and perpendicular to the specimen axis,

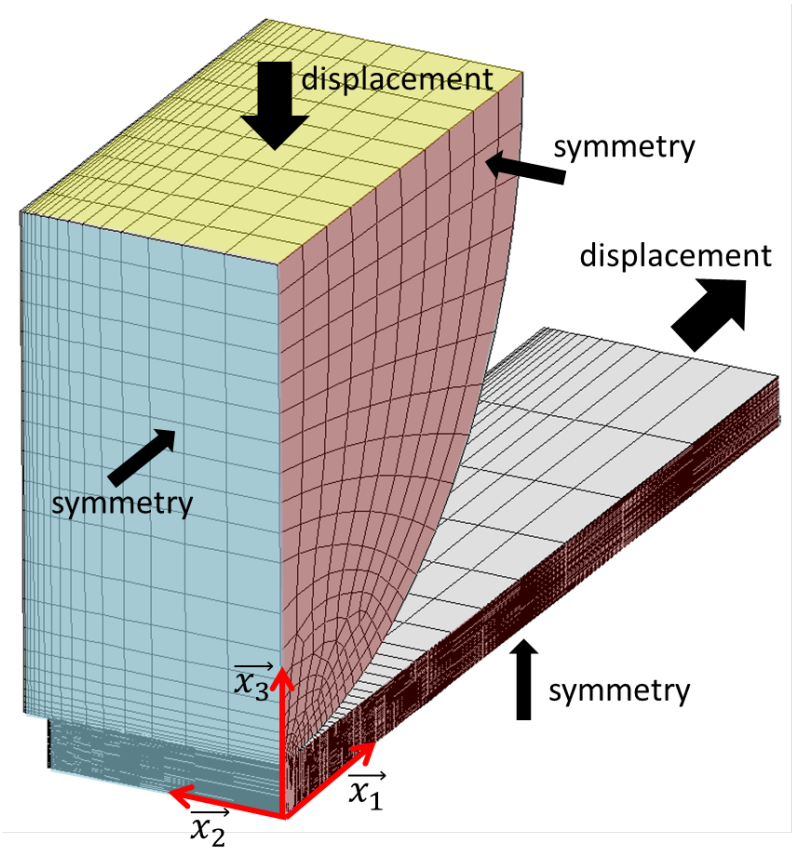

Figure 6.8: The mesh used for the finite element simulation of the biaxial test and the applied boundary conditions. Symmetry boundary conditions are applied in three direction, so only one-eighth of the problem needs to be meshed.

indicating fibre-breakage-dominated tensile failure. The failure mode did not change, independent of the applied tension-to-compression ratio. Indeed, certain specimens broke uniquely due to the locally applied compression. Figure 6.9 shows an example of a typical low voidage specimen after failure. For the high voidage specimens, the failure mode was the same, but more fibre pull-out could be observed. DIC observations of the free edge confirm that applying compression by cylindrical indenters causes locally a significant deformation along specimen axis. Figure 6.10 shows the computed longitudinal strain (ε_{11}) contours in a low voidage specimen at an applied pressure of 34 bar.

Figure 6.11 summarizes the applied external load values at failure for the low and high voidage specimens, marked with blue and red points, respectively. Uniaxial tensile test results are also shown for reference (points located on the y-axis). The low voidage specimens were tested at three levels of compression: 25, 50 and 100 bar. The high voidage specimens were tested at 25 and 50 bar. The high voidage

specimens failed before reaching the pressure of 100 bar, on average at 84.8 bar. These specimens are represented by points located on the x-axis. As demonstrated by the DIC results discussed above, local compression generates a complex strain and stress state that cannot be measured directly. The values of stress at ply level can be recovered by finite element analysis using the material properties of the composite. The result of this analysis are discussed in the next section. Nonetheless, already by analyzing the loads at failure, it is visible that the presence of voids reduces significantly the composite strength under the studied biaxial conditions and leads to an increased scatter in the experimental results. This might be a result of the highly localized stress state. Since the critical conditions are present in a small region of the specimen, the shape, size and distribution of voids in that region can significantly influence the stress state, and therefore the strength of the composite.

Stress analysis Stresses at failure are evaluated by finite element analysis. Indenter displacement is controlled so that the external reactions are equal to the average compressive and tensile loads at failure obtained from the experiments. The numerical values of indenter reaction and displacement are compared against those measured experimentally. The two curves show a good agreement, as seen in Figure 6.12. It can be concluded that despite a large through-thickness deformation, locally reaching almost 15%, the linear elastic material behaviour is an acceptable assumption.

Figure 6.13 shows the simulated stresses at failure on the fracture plane under the indenters. The stress components are represented in the global coordinate system, as shown in Figure 6.8. Given the fibre break-dominated failure mode of the specimens, the axial stress σ_{11} in the longitudinal 0° plies at $x_1 = 0$ is of special interest. Simulation shows that compressing the composite by the cylindrical indenters leads to axial tensile deformation in the specimen, as also observed experimentally through DIC (Figure 6.10). This results in a high tensile stress σ_{11} in the 0° plies. The through-thickness compressive stress is approximately uniform in the whole specimen section between the indenters.

At the applied pressure of 25 bar, especially for the low voidage specimens, the value of σ_{11} at failure is similar or even slightly higher than that computed for the uniaxial tension case. This surprising result can be attributed to the localized character of critical stress in the biaxial test. Since only a small region of the specimen experiences the critical conditions, the strength can be higher due to the size effect. The size effect in composites manifests through a higher strength of smaller specimens, as reported in the literature [17] [63] [182] [172]. Increasing the applied compressive load to 50 bar and 100 bar significantly reduces the value of longitudinal stress σ_{11} at failure. For the low voidage material subjected to a compressive load of 100 bar, corresponding to a through-thickness stress of

approximately 1000 MPa, the value of σ_{11} at failure is lower by a factor of 2 compared to the uniaxial tension case.

As visible from the measured external load values at failure (Figure 6.11), void presence further reduces the tensile strength of the composite. At the same applied pressure, the through-thickness stress is lower for the high voidage case. This is due to the higher transverse compliance of the composite with voids, leading to a distribution of load over a larger contact area. The observations on the decrease of the stress σ_{11} at failure in the presence of through-thickness compression, discussed above for the low voidage specimens, are still valid here. In fact, the tendency is significantly stronger. In the critical plies, for a through-thickness compressive stress of approximately 900 MPa, the average σ_{11} at failure is lower by over 60% with respect to the uniaxial tensile strength.

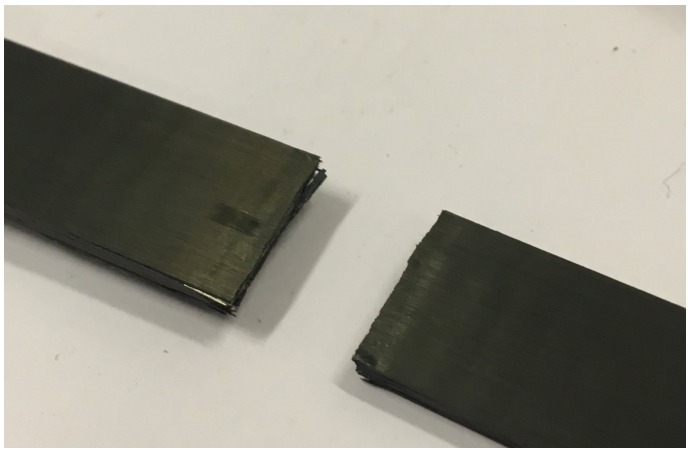

Figure 6.9: Fractured specimen broken only through compression by R10 indenters.

6.5 Conclusions

The results presented in this chapter allow evaluating the influence of voids on the strength of a composite material subjected to loading conditions similar to those present in a thick-walled pressure vessel. By controlling the curing pressure of the laminate, cross-ply carbon-epoxy specimens with a low and high void content were obtained.

The obtained material was first tested in tension. It was observed that a high void content leads to a moderate reduction in tensile strength and stiffness. Next, the material was tested in biaxial conditions: in-plane tension with out-of-plane compression. The tests were carried out on a custom-built experimental setup. The biaxial tests lead to the following qualitative conclusions:

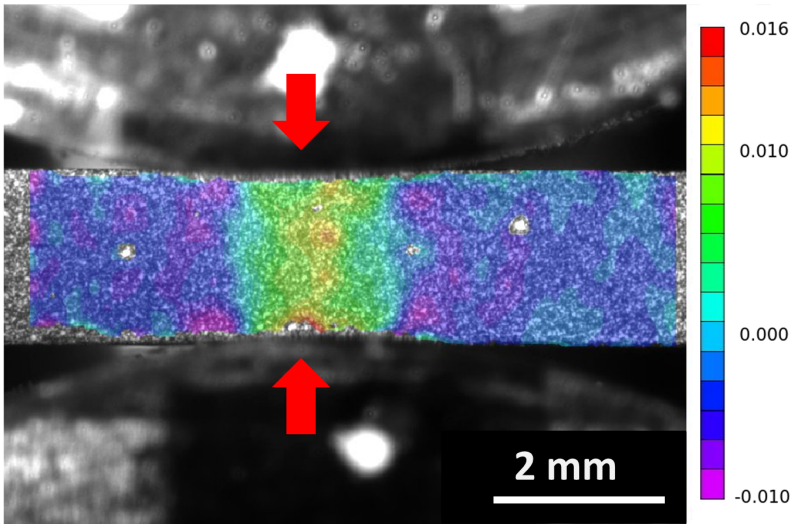

Figure 6.10: DIC: ε_{11} strain (horizontal direction) at an applied pressure of 34 bar. The cylindrical indenters are visible below and above the specimen. The red arrows indicate the loading direction.

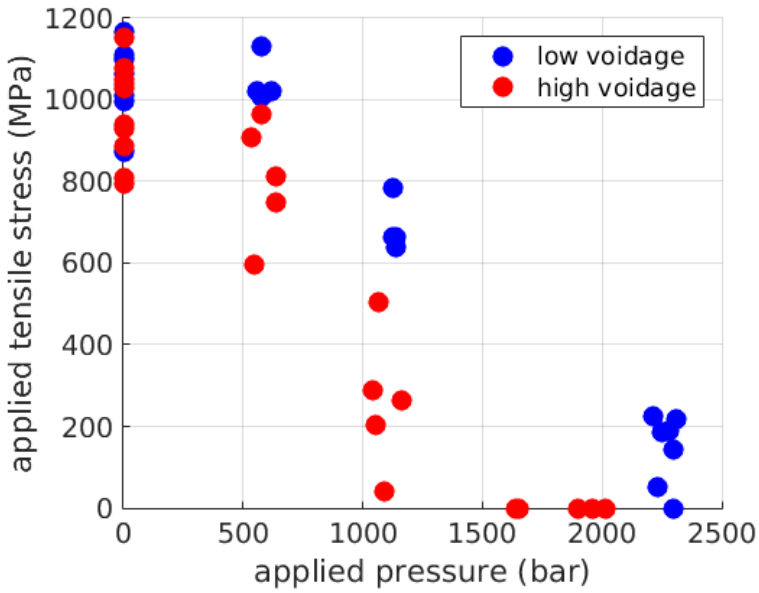

Figure 6.11: Biaxial testing: applied loads at failure.

(i) Through-thickness compression does not change the failure mode of a unidirectional composite loaded in longitudinal tension, but it reduces the tensile strength.

(ii) High void content reduces the strength of a unidirectional ply under the biaxial conditions considered in this study.

The first point is in agreement with the results from the literature discussed earlier. Figure 6.14 shows the results of several experimental studies on the effect of transverse compression on tensile strength of carbon-reinforced composites. The results of the study presented here are marked by black squares. The points correspond to the average stress in the most loaded plies for the low voidage material (Figures 6.13a, 6.13c, 6.13e). Some caution is necessary when comparing the different studies. Not all loading cases are equivalent and the fibres and resins used were not the same. Nonetheless, in all studies the longitudinal tensile strength exhibits an approximately linear decrease for growing values of transverse compression. It is not clear what mechanism is responsible for this phenomenon. Parry and Wronski [116] suggest that hydrostatic pressure prevents matrix cracking and debonding, which localizes stresses around the initial fibre breaks and allows their quick propagation in a single plane. However, the reduction in strength is also observed at higher pressures, where cracking and debonding is already supressed. Another possibility is that the reduced space between fibres leads to an increase in the overstressing around individual fibre breaks. For touching fibres, additional contact stresses would also appear.

Based on biaxial test experimental results, phenomenological ply failure criteria have been proposed by Gan et al. [47] and Goto et al. [48]. The latter was based on tests on unidirectional composites and therefore predicts a failure in transverse compression at a moderate stress (around 200 MPa). The criterion of Gan et al. is of more interest, as it takes into account the increased through-thickness compressive strength of a cross-ply laminate. The proposed criterion is:

$$\sigma_{11} - \sigma_{33} \geq \sigma_C, \tag{6.1}$$

where σ_{11} is the fibre direction tensile stress, σ_{33} is the through-thickness stress. σ_C is the critical stress, equal to the tensile strength of a UD ply. This criterion can be used to describe approximately the results presented in this chapter. This has important consequences when applied to pressure vessel analysis. For instance, if σ_{33} is equal to 7% of σ_{11} in the critical ply, as for the cylinder considered in Appendix B, the predicted burst pressure of the cylinder is reduced by 7% with respect to the uniaxial failure criterion. Furthermore, as has been demonstrated in the work presented in this chapter, the presence of voids can magnify the effect of multiaxial stresses, leading to an even further strength reduction. This could be intuitively explained by the voids leading to high concentrations of the through-thickness stress. The stress concentration values depend strongly on the local void morphology, which would explain the significant experimental scatter of the high voidage laminate strength.

The results presented in this chapter demonstrate that a uniaxial failure criterion may not be sufficient to accurately predict the burst pressure of a thick-walled pressure vessel. Furthermore, it is shown that void presence can reduce the strength

of the composite even further. It is difficult to clearly isolate these two effects at the scale of the pressure vessel, which is why experiments were performed on smaller representative specimens. Carrying out the required tests on pressure vessels would be a costly task, especially for thick-walled cylinders. Furthermore, other factors, such as the size effects or microstructure variability might mask the effect of the studied phenomena. This can be addressed by developing a numerical model of the composite, taking into account the observed phenomena, and applying it at the structural scale.

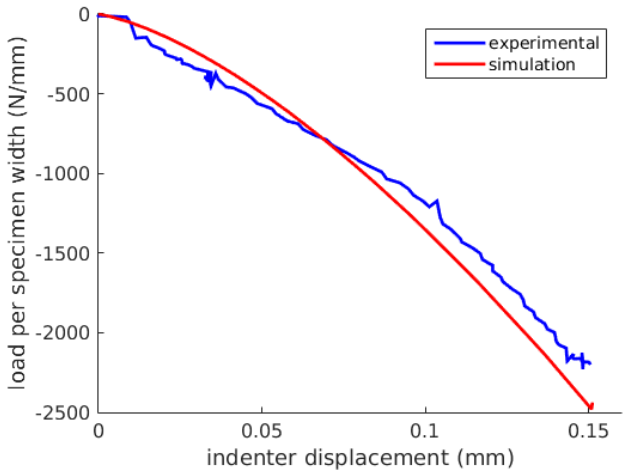

Figure 6.12: Indenter displacement as observed experimentally (blue) and simulated (red). The maximum displacement corresponds to an applied pressure of 100 bar.

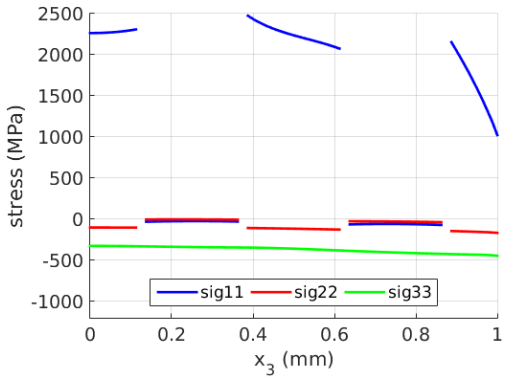

(a) Low voidage: 25 bar compression, 1032 MPa tension.

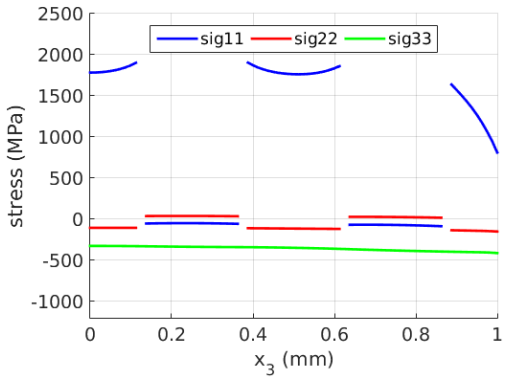

(b) High voidage: 24 bar compression, 807 MPa tension.

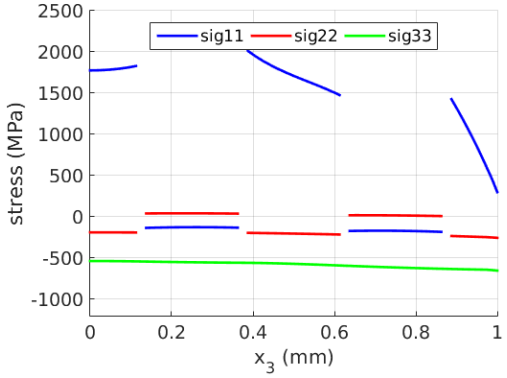

(c) Low voidage: 47 bar compression, 683 MPa tension.

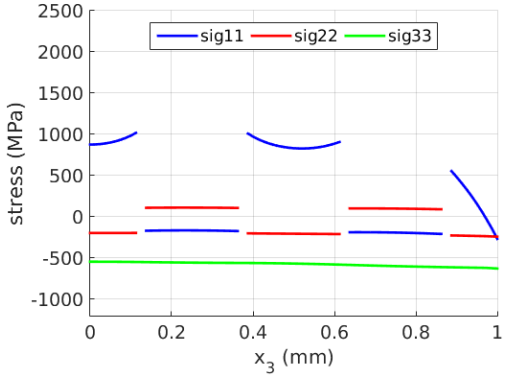

(d) High voidage: 49 bar compression, 251 MPa tension.

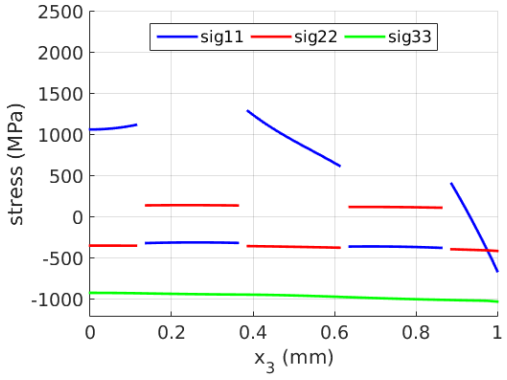

(e) Low voidage: 99 bar compression, 146 MPa tension.

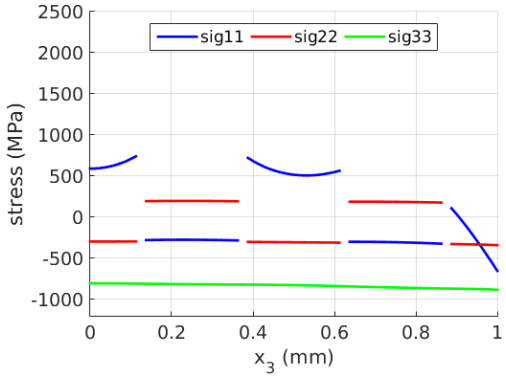

(f) High voidage: 85 bar compression, 0 MPa tension.

Figure 6.13: FEM simulation: through-thickness stress distribution inside the specimens. The combinations of applied loading correspond to average specimen strength recorded from experiment. $x_3 = 0\,\text{mm}$ corresponds to mid-thickness of the specimen, $x_3 = 1\,\text{mm}$ is located on specimen surface. The other coordinates are $x_1 = 0\,\text{mm}$ and $x_2 = 0\,\text{mm}$. The coordinate system is illustrated in Figure Figure 6.8.

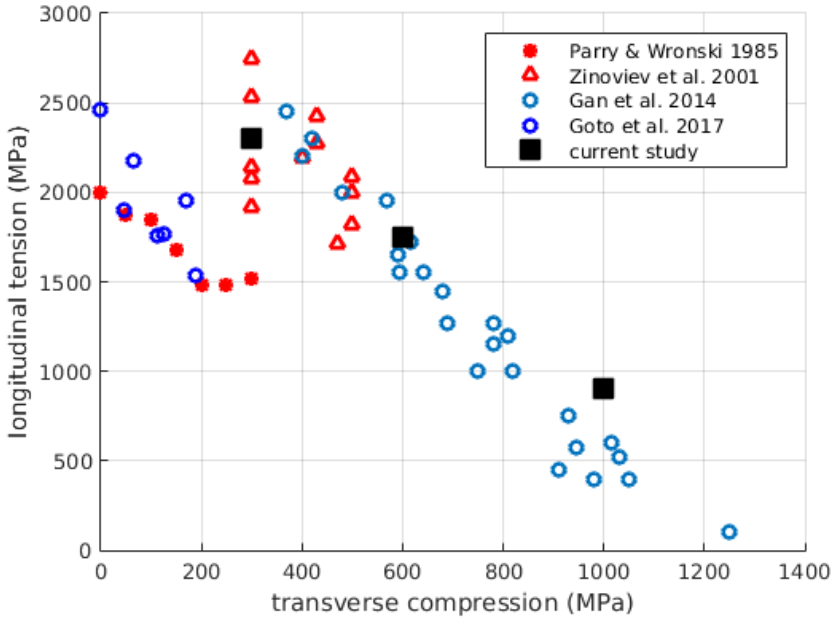

Figure 6.14: Comparison of CFRP strength under biaxial loadnig conditions gathered from the literature. Large square markers correspond to average results from the study presented here (low voidage specimens).

Chapter 7

Numerical modelling of a thick-walled composite pressure vessel

Chapitre 7. Modélisation numérique d'un réservoir composite à parois épaisses

Dans ce chapitre, on expose des simulations numériques faites dans le cadre du modèle multiéchelle de rupture des fibres développé originellement par Blassiau (MPFBM). Le modèle est enrichi afin de prendre en compte l'influence des porosités macroscopiques, ainsi que l'effet de la sollicitation biaxiale.

La première amélioration apportée au modèle MPFBM est la modélisation des porosités est leur homogénéisation dans les propriétés élastiques du composite unidirectionnel. Ceci est fait par un procédé à deux étapes dans le cadre du modèle autocohérent généralisé. Dans un premier temps, on obtient les propriétés d'un composite sans porosité. Dans la deuxième étape, les porosités sont modélisées comme étant des inclusions cylindriques infiniment longues sans rigidité, qui sont par la suite à nouveau homogénéisées dans le matériau composite. Ce modèle prévoit une réduction linéaire de la rigidité longitudinale en fonction du taux de porosité, ce qui est en bon accord avec les observations expérimentales. Une autre approche à la modélisation des porosités est aussi proposée, en incluant les porosités directement dans le maillage par éléments finis.

La deuxième amélioration apportée au modèle MPFBM est la prise en compte de la contrainte de compression transverse, au sein du critère d'évolution des ruptures de fibres. Basé sur les résultats expérimentaux, on propose un critère biaxial phénoménologique de rupture des fibres, qui est implémenté dans le modèle MPFBM.

Ensuite, plusieurs cas de sollicitations sur éprouvettes et réservoirs, avec les différents stades du modèle (originel, amélioré) sont présentées.

D'abord, on regarde le cas d'une éprouvette carbone-époxy. Deux types de sollicitation sont considérés : traction longitudinale seule, puis couplée ensuite avec une compression dans le sens de l'épaisseur. Les résultats numériques sont en bon accord avec les observation expérimentales exposées sauf pour le cas biaxial pour un taux de porosité élevé. Dans ce dernier car, le fort effet négatif des porosités n'est pas capturé. Les deux approches à la modélisation des porosités rendent des résultats très similaires.

Ensuite, on modélise un essai d'éclatement d'un réservoir composite à parois épaisses. Les mêmes modèles (originel, amélioré) que dans le cas de l'éprouvette sont utilisés. Le taux calculé de la compression dans le sens de l'épaisseur à la traction longitudinale est approximativement 20 % dans la région du composite la plus chargée. Dans ces conditions, la prise en compte du critère biaxial de rupture entraîne une réduction de la pression d'éclatement d'à peu près 13 %. Si on prend en compte également un taux de porosité de 5 %, la différence est de 18 %. Cela souligne que la présence des porosités et la sollicitation biaxiale peuvent être des facteurs importants de perte de propriété pour la résistance à rupture d'un réservoirs composite à parois épaisses.

7.1 Introduction

The multiscale model introduced in Chapter 2 provides a useful tool for analyzing damage phenomena in fibre-reinforced composites. It allows statistical strength modelling at the structural level, based on fibre strength distribution. It also takes into account the time-dependent behaviour of the composite, which has been shown to match well with experimental results on pressure vessels [27]. The experimental work presented in Chapter 6 identified two further factors influencing pressure vessel strength that have not been so far considered in the model: presence of macroscopic voids in the composite material and the effect of the through-thickness compressive stress. In this chapter, an approach is proposed to incorporate the influence of these phenomena into the existing modelling framework. First, two void modelling methods are discussed: a homogenization method using the generalized self-consistent scheme and secondly a direct meshing approach. Then, a new fibre failure criterion is proposed, based on the biaxial test results. Next, failure simulations of a unidirectional CFRP coupon are carried out, using the models proposed previously. Finally, burst simulations are performed on a model thick-walled pressure vessel, testing the modelling approaches and allowing the evaluation of the influence of the considered phenomena at the structural level.

7.2 Modelling strategies

7.2.1 Macroscopic voids: generalized self-consistent scheme

The first proposed approach for taking into account void presence is the homogenization of the elastic properties of a unidirectional composite ply with voids. Many analytical models have been proposed to predict the effective elastic properties of fibre- and particle-reinforced composites, based on the properties of the constituents. They include the Composite Cylinders Model of Hashin [52], self-consistent scheme of Budiansky and Hill [16] [60] and the Mori-Tanaka method [103], applied to composites by Benveniste [5]. For the work presented here, the properties of the homogenized material are predicted using the generalized self-consistent scheme (GSCS) proposed by Christensen and Lo [30]. While the results of Mori-Tanaka are usually close to GSCS, the latter provides better predictions of the shear modulus [28].

In order to derive the effective properties using GSCS, an auxiliary configuration is introduced, as shown in Figure 7.1. An infinitely long cylindrical fibre is surrounded by a concentric cylindrical annulus of the matrix material. The two are embedded in an effective equivalent medium with unknown properties, corresponding to those of the homogenized fibre-matrix system. The relative volume

of the fibre and matrix phase is taken to be that corresponding to the volume fraction of the homogenized medium. The effective medium is transversely isotropic and its stiffness can be therefore described by five independent elastic coefficients. Christensen [29] provides a closed-form formula for the case of isotropic constituents. Hervé and Zaoui presented a solution for multiply-coated fibre-reinforced composites with transversely isotropic constituents [58]. The last assumption is important for carbon fibres, which are strongly anisotropic [100] [95].

Analytical methods have been proposed for a two-level homogenization of a fibre-reinforced composite material with voids using the Mori-Tanaka model [44] [24] and GSCS [173]. The latter approach is used here to model macroscopic voids. The method is schematically illustrated in Figure 7.1. In the first step, the properties of the composite are calculated, by homogenizing a fibre-matrix system into a transversely isotropic medium. The relative volume of fibre to matrix corresponds to the fibre volume fraction in the modelled composite.

In the second step, we represent voids as infinitely long cylinders, aligned with the longitudinal direction of the composite. This represents the macroscopic needle-shaped voids observed experimentally, as discussed in Chapter 4. The GSCS homogenization procedure is then repeated. Voids, modelled as cylindrical inclusions with null stiffness, are embedded in a matrix with properties of the previously homogenized fibre-matrix system. This allows us to quickly estimate the elastic properties of a unidirectional composite material with an arbitrary volume fraction of macroscopic voids.

The predictions of the model are illustrated on the example of a composite reinforced with T300 carbon fibres at a 64% fibre volume fraction. The matrix is modelled as linear elastic isotropic, with $E = 3\,\mathrm{GPa}$ and $\nu = 0.4$. Figure 7.2 shows the elastic coefficients of the composite at various void volume fractions. The reduction in longitudinal tensile modulus is linear and proportional to the void fraction. This is due to the reduction in the effective fibre volume fraction, i.e. fibre volume divided by the volume of the material cross-section including voids. The transverse properties are more sensitive to void presence, with the model predicting a strongest drop in the transverse tensile modulus and transverse shear modulus. Both show a reduction of approximately 13 % for a void fraction of 5 %. The longitudinal shear modulus is also affected, with a reduction of approximately 10 %. The longitudinal and transverse Poisson's ratios, not shown in the figure, do not change significantly.

The two-step homogenization procedure introduced above provides an analytical tool for quickly predicting the elastic properties of a unidirectional composite with arbitrary fibre and void volume fraction. The computed longtitudinal properties show a good agreement with the experimental results presented in Section 6.3.

E_{11}	$E_{22} = E_{33}$	$\nu_{12} = \nu_{13}$	ν_{23}	$G_{12} = G_{13}$
230 GPa	8 GPa	0.256 -	0.300 -	27.3 GPa

Table 7.1: Elastic properties of T300 carbon fibres [100].

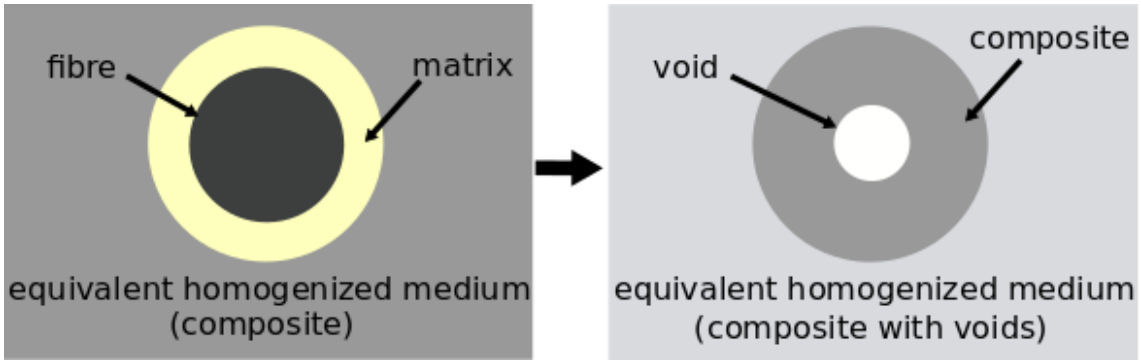

Figure 7.1: The general concept of GSCS for a two-step homogenization of a fibre-reinforced composite with cylindrical voids.

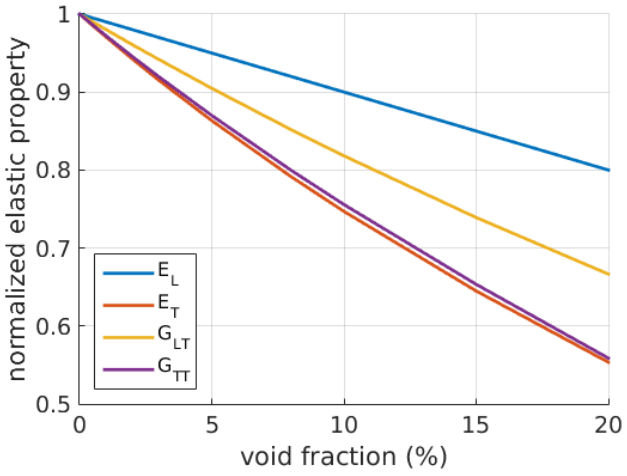

Figure 7.2: Elastic properties prediction by the two-stage GSCS homogenization. The values are normalized by the property at 0% void volume fraction. The reference values are: E_L =140.7 GPa, E_T =5.9 GPa, G_{LT} =4.4 GPa, G_{TT} =2.1 GPa.

7.2.2 Macroscopic voids: direct meshing

The GSCS method introduced above does not take into account individual void characteristics in the composite and takes porosity into account through homogenization. The second proposed approach, referred to as direct void meshing (DVM), takes void presence into account in a more explicit way. The void shape and size analysis carried out in Chapter 4 shows that most macroscopic intralaminar voids are needle-shaped and follow fibre direction. Their shape and orientation are therefore similar to those of finite elements used in the fibre break model ($8.0 \times 0.1 \times 0.1$ mm). Based on this observation, voids can be directly included in the finite element mesh, without modifying its geometry. Selected elements are treated as voids and are assigned a null stiffness matrix. The number of these void elements in the mesh is selected according to the prescribed void volume fraction and the locations are randomly assigned. The advantage of this method with respect to the homogenization approach is that it treats voids at a more local level. This is important for the simulation of damage processes, which take place locally at the microscopic level. However, assigning null stiffness to selected elements introduces non-physical stress concentrations in the finite element simulation. While relatively low due to the high aspect ratio of the finite elements, these additional stresses can lead to an early onset of fibre breakage. The direct meshing approach therefore overestimates the influence of voids and can be expected to provide a conservative strength estimate.

7.2.3 Effect of compression: biaxial failure criterion

The second factor identified as significant for pressure vessel strength is the through-thickness compressive stress. As demonstrated in Chapter 6, through-thickness stress reduces the tensile strength in the fibre direction. However, no convincing explanation has been found of the underlying reasons for this behaviour. A phenomenological biaxial ply failure criterion proposed by Gan et al. [47] (Equation 6.1) was shown to provide a good estimate of composite strength under the considered conditions. Here, it is used as a basis for a modified fibre break criterion, to provide an estimate of the effect of multiaxial stresses.

As discussed in Chapter 2, the fibre break model of Blassiau et al. uses a fibre break criterion of the form

$$\sigma_{11} \geq \sigma_C, \tag{7.1}$$

where σ_{11} is the tensile stress in the longitudinal direction and σ_C is the fibre strength, such as can be estimated experimentally by single fibre testing. This type of criterion does not capture the reduced composite strength under transverse compression, so an alternative approach is necessary. By analogy to the ply failure criterion mentioned above, the following fibre break condition is implemented in the

fibre break model:

$$\sigma_{11} - \sigma_{33} \geq \sigma_C. \tag{7.2}$$

In presence of through-thickness compression, the term σ_{33} is negative and therefore the combined value of the left hand side is increased, resulting in an increased fibre break probability. The effect is equivalent to reducing the value of σ_0 of the Weibull distribution by σ_{33}.

7.3 Numerical simulation: unidirectional coupon

7.3.1 Methods

Firstly, the numerical approaches proposed above are tested for the case of a unidirectional coupon. The geometry and material properties are the same as in the example problem discussed in Section 2.2.3. For convenience, the material properties of the unidirectional ply are presented again in Table 7.2. The failure simulation is carried out with different models in order to evaluate the influence of the proposed modifications. The considered models are:

(i) **FBM**: standard fibre break model
(ii) **GSCS**: FBM with GSCS ($V_v = 5\%$)
(iii) **DVM**: FBM with direct void meshing with ($V_v = 5\%$)
(iv) **BIAX**: FBM with biaxial failure criterion
(v) **GSCS-BIAX**: FBM with biaxial failure criterion and GSCS ($V_v = 5\%$)
(vi) **DVM-BIAX**: FBM with biaxial failure criterion and direct void meshing ($V_v = 5\%$)

For each model, two loading cases are studied: longitudinal tension (T) and longitudinal tension with through-thickness compression (TC). These loading cases are represented schematically in Figure 7.3. For the tension case, the composite is loaded in the axial direction at 0.2 MPa/second, same as for the example case in Section 2.2.3. In tension-compression, the axial load is applied in the same way. Additionally, a compressive load is applied to the top and bottom surfaces of the specimen at a loading rate of 0.04 MPa/second. This results in a compression-to-tension factor of 0.2, comparable to what can be locally encountered in thick-walled pressure vessels. The stochastic strengths for the fibre break model are generated for a gauge length of 4 mm from a Weibull distribution with $\sigma_0 = 4.32$ GPa and $m = 5.62$, for a reference gauge length $L_0 = 25$ mm.

E_{11}	E_{22}=E_{33}	$\nu_{12} = \nu_{13}$	ν_{23}	$G_{12} = G_{13}$	G_{23}
145.0 GPa	12.5 GPa	0.29 -	0.40 -	5.5 GPa	7.0 GPa

Table 7.2: Elastic properties of an undamaged UD ply for 64% fibre volume fraction.

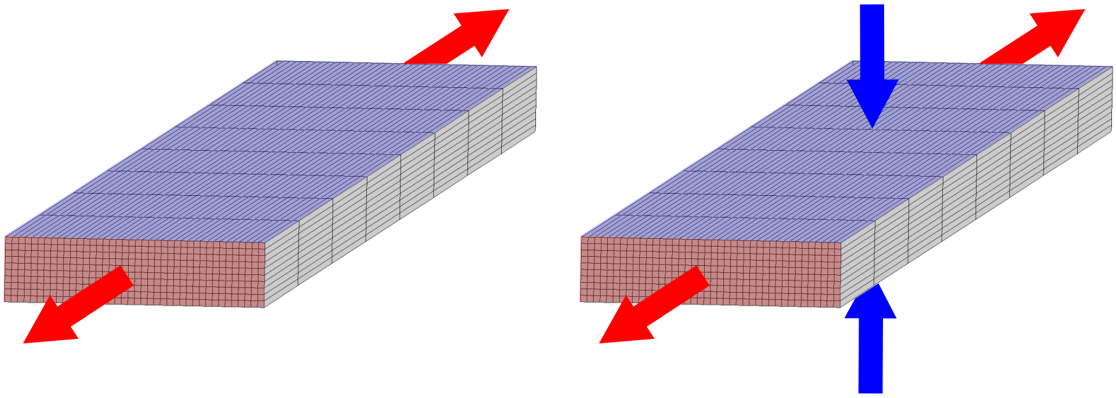

(a) Tension (T). (b) Tension-Compression (TC).

Figure 7.3: External loading cases for the unidirectional coupon simulations. The compressive stress in the TC case is equal to 20% of the longitudinal stress.

7.3.2 Results

Table 7.3 summarizes the values of strength and ultimate strain for all studied cases. Strength is further visualized in Figure 7.4. Regardless of the model used, the TC case is more critical than T. For FBM, GSCS and DVM, this is due to the additional strain in the axial direction caused by the compressive load. For the load combination used here ($\sigma_{33}/\sigma_{11} = 0.2$), the reduction in strength due to compression is in the order of 5%. This effect is therefore too small to explain the strength loss of approximately 20%, observed experimentally for this type of loading. Both methods of void modelling (GSCS and DVM) result in similar strength predictions. Void fraction of 5% leads to a strength reduction of approximately 5% in both cases.

For the tension case, the three models using the biaxial failure criterion (BIAX, GSCS-BIAX, DVM-BIAX) show only a slightly lower strength than the corresponding models with the uniaxial criterion. However, for tension-compression, they exhibit a more drastic strength reduction. For BIAX, the difference is -14% with respect to FBM. This result is close to the tendencies observed experimentally, as discussed in Chapter 6.

The addition of the biaxial failure criterion does not appear to change the influence of voids on the tensile strength in GSCS-BIAX and DVM-BIAX. This

is somewhat surprising for DVM-BIAX, where locally voids introduce concentration in the through-thickness stress σ_{33}. In fact, for both GSCS-BIAX and DVM-BIAX, the absolute reduction in strength is similar to that observed for the models without the biaxial criterion. That means that for the proposed modelling approaches there is little interaction between the two phenomena (voids and through-thickness compression) and the two effects are superposed. This does not capture the strong effect of voids under tension-compression conditions observed experimentally and further investigation is therefore necessary.

	Tension (T)		**Tension-Compression (TC)**	
	Strain(%)	Stress(MPa)	Strain(%)	Stress(MPa)
FBM	1.52	2165	1.49	2043
GSCS	1.52	2059	1.50	1955
DVM	1.50	2030	1.48	1928
BIAX	1.48	2122	1.28	1760
GSCS-BIAX	1.49	2019	1.27	1644
DVM-BIAX	1.48	2003	1.27	1652

Table 7.3: Unidirectional coupon, stress and strain at failure.

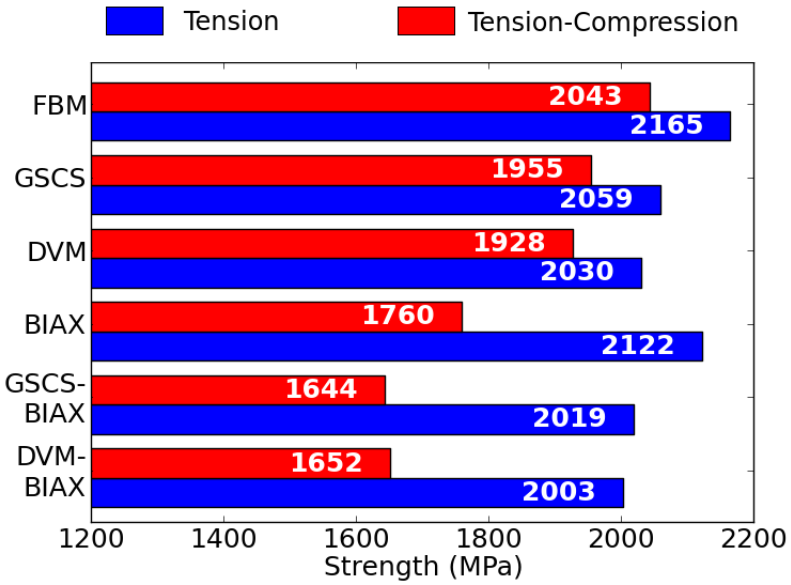

Figure 7.4: Unidirectional coupon strength for all considered models.

7.4 Numerical simulation: thick-walled composite pressure vessel

7.4.1 Methods

The second set of simulations models the burst test of a thick-walled pressure vessel. The geometry of the finite element mesh is shown in Figure 7.5. The model cylinder has an internal radius of 15 mm and the external radius of 20 mm. Two composite layers are used: a 90° ply of thickness 3.5 mm on the inner side of the cylinder followed by a 20° ply of thickness 1.5 mm. The length of the cylindrical section along the axial direction is equal to 20 mm. The domes are modelled as hemispherical, with the same ply thickness and orientations as in the cylindrical section. While this assumption does not accurately represent the geometry of real pressure vessels, this is considered an acceptable simplification. The stresses in the domes are known to be significantly lower than in the cylindrical section, so the exact representation of their geometry is not of primary importance. In the cylindrical section, linear 8-node brick elements of size 8.0 mm × 0.1 mm × 0.1 mm are used, corresponding to eight representative volume elements of the fibre break model (see Chapter 2). In total, the mesh consists of 134 400 elements. The hoop ply, where the damage model is applied, corresponds to 84 000 of those elements. For the standard fibre break model, the same elastic ply properties are used as for the simulation on a unidirectional specimen presented in Section 2.2.3. Same as in the unidirectional coupon case, fibre strengths are generated from a Weibull distribution with $\sigma_0 = 4.32\,\text{GPa}$ and $m = 5.62$. Pressure is applied to the internal surface of the pressure vessel at a loading rate of 10 bar/s. Failure of the cylinder is identified by a sudden increase in radial displacement, measured at a point on the inner surface of the cylinder. The burst simulation is carried out for the same models as in the UD coupon case:

(i) **FBM**: standard fibre break model
(ii) **GSCS**: FBM with GSCS ($V_v = \text{X}\%$)
(iii) **DVM**: FBM with direct void meshing with ($V_v = \text{X}\%$)
(iv) **BIAX**: FBM with biaxial failure criterion
(v) **GSCS-BIAX**: FBM with biaxial failure criterion and GSCS ($V_v = \text{X}\%$)
(vi) **DVM-BIAX**: FBM with biaxial failure criterion and direct void meshing ($V_v = \text{X}\%$)

7.4.2 Results

Burst pressure comparison Figure 7.6 shows a comparison of the cylinder burst pressure for different models used in the numerical study. The relative tendencies

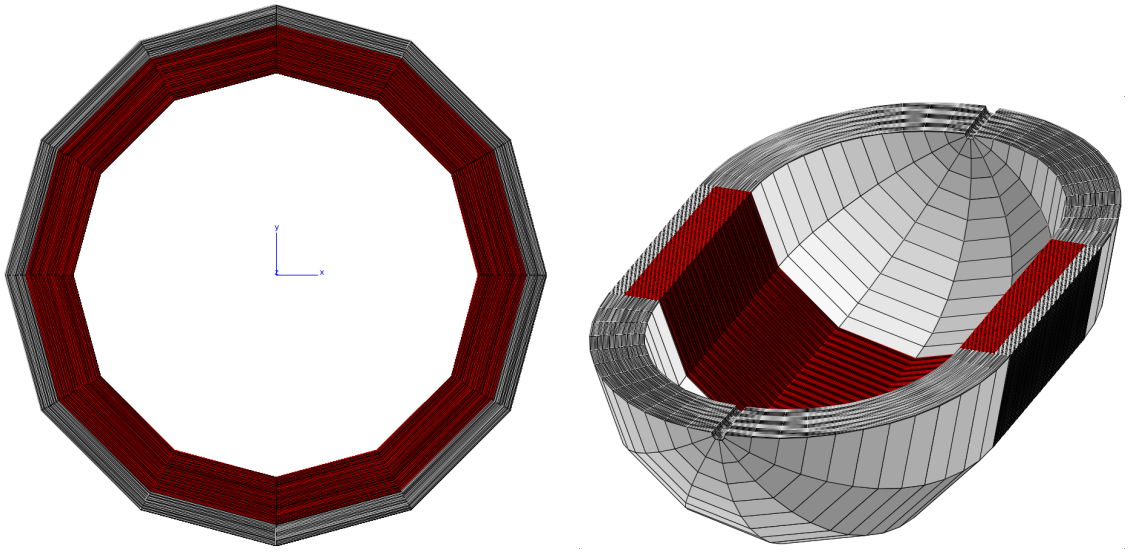

(a) Cross-section. (b) Longitudinal section.

Figure 7.5: Pressure vessel model mesh. The region of the hoop ply in which the fibre break model is applied is marked in red.

between the models are similar to those observed in the unidirectional coupon simulations. It can be seen that the pressure is highest for the standard fibre break model (FBM). Unlike in the UD coupon case, the strength reduction is more pronounced for GSCS than DVM. However, for both approaches the burst pressure reduction with respect to the reference case (FBM) is similar and equal to approximately 5%. Using the biaxial criterion significantly reduces the computed burst pressure. For BIAX, the reduction is equal to 13% with respect to FBM. Accounting for void presence removes the burst pressure further. For DVM-BIAX, the burst pressure is lower by over 17% with respect to the standard model (FBM).

Stress distribution Analyzing stress distribution in the internally pressurized cylinder provides some insights into the fibre break process evolution. The stresses are described in the local frame of the material, i.e. σ_{11} is the stress in the fibre direction and σ_{33} is the through-thickness component. Figure 7.7 shows the contours of the longitudinal and through-thickness stress in the hoop ply for an applied internal pressure of 250 bar for the standard model (FBM). This corresponds to approximately 40% of the burst pressure. At that point, few fibre breaks are present in the composite. The longitudinal stress σ_{11} in the hoop ply is non-uniform, with a strong through-thickness gradient. The highest values of σ_{11} are present near the internal wall, almost twice as high as at the external face of the ply. The through-thickness stress is also highest at the inner surface of the cylinder, with its absolute value there equal to approximately 20% of the maximum value of σ_{11}.

The analysis of the stress state provides an additional insight into why the biaxial criterion reduces the burst pressure. Since the compressive stress is highest at the internal wall, there is an increased tendency for damage localization in that region. As a result, even though the critical stress state is present in a smaller fraction of the structure with respect to the UD coupon case, the reduction in strength is similar for the pressure vessel.

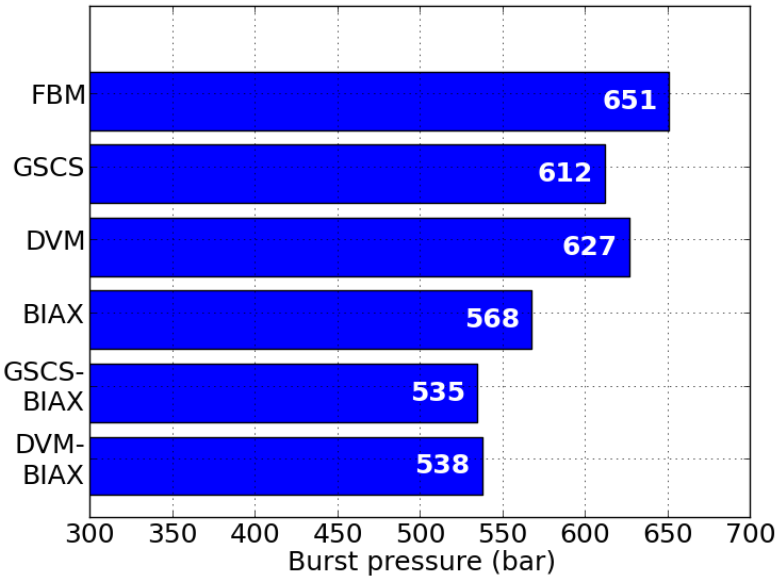

Figure 7.6: Burst pressure for all considered models.

7.5 Conclusions

Two methods of accounting for macroscopic voids have been proposed, as well as a phenomenological biaxial fibre break criterion. These modelling strategies are based on the experimental observations described in this thesis, in particular on the biaxial test results, discussed in Chapter 6. The simulation of unidirectional coupons shows little sensitivity to voids in uniaxial tension. For a composite with voids, the reduction in tensile strength is proportional to the reduction in stiffness. This is in agreement with the experimental results.

For the standard fibre break model (FBM), through-thickness compression has little effect on the tensile strength of the unidirectional specimen. The additional strain caused by the Poisson's effect cannot explain the important strength reduction observed experimentally in biaxial tests. This justifies the use of the biaxial failure criterion, which leads to results much closer to the experimental ones. While the

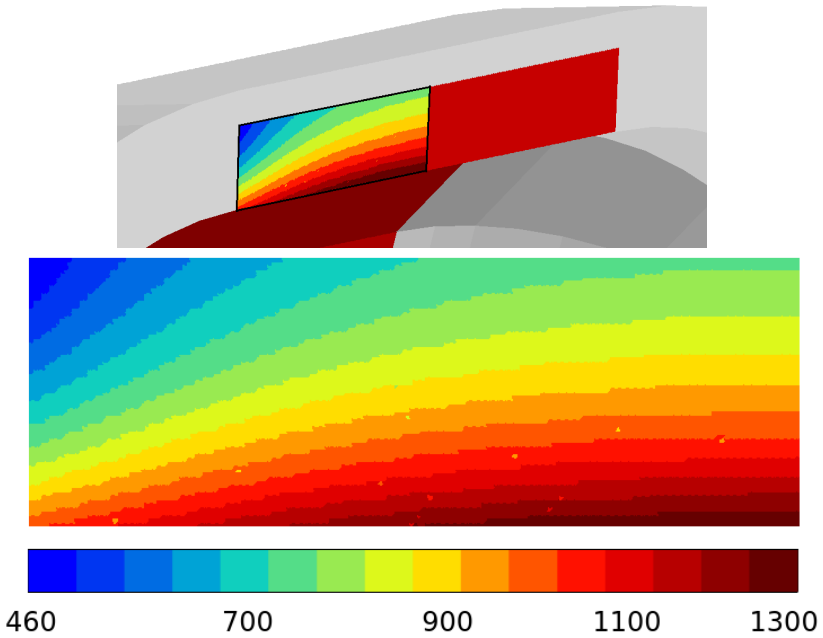

(a) Longitudinal stress σ_{11} (MPa).

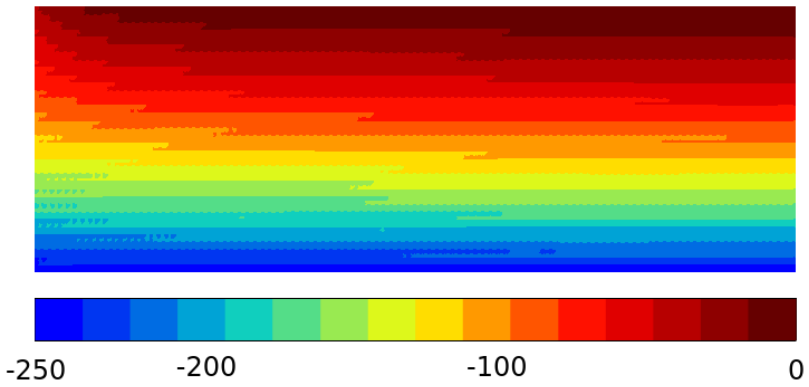

(b) Through-thickness stress σ_{33} (MPa).

Figure 7.7: Stress distribution in the hoop ply for an internal pressure of 250 bar. The contour plot location is marked by black outline in the top image. Hoop ply marked in red. Only half of the ply is shown, since the stress distribution is symmetric with respect to the right-hand side edge of the figures.

criterion does not address the micromechanics of the failure process, it can be used to provide an estimate of the effect of the multiaxial stress state.

After confirming that the proposed models show a good agreement with the experimental results, a second set of simulations is carried out to compute the burst pressure of a thick-walled composite pressure vessel. This allows evaluating the importance of the studied factors (voids, through-thickness compression) that

cannot be easily found experimentally. It is seen that the inclusion of the biaxial criterion (BIAX) leads to a much larger decrease in burst pressure than modelling void presence (GSCS, DVM). The strong negative influence of voids on strength under biaxial conditions is not captured in the proposed models and requires further investigation.

The simulations, taking into account the experimental results described in Chapter 6, show that the burst pressure of a pressure vessel may be lower than that predicted by tensile strength models, based uniquely on fibre tensile strength. This result may come as a surprise and a question can be asked: if the compression is a significant factor, why hasn't its influence been established more definitively so far? Several explanations can be offered. For instance, the effect could be masked by stress concentrations due to local material variability. Secondly, a reliable computation of stresses in a real-life structure can be problematic, due to gradients in fibre volume fraction and void fraction, as demonstrated in Chapter 4. Other damage phenomena, such as fibre-matrix debonding and longitudinal splitting, could influence the burst pressure value. Another factor could be the existence of a size effect which is not fully understood for pressure vessels [31] [32]. Finally, the high safety coefficients used at the design stage may also make the effect harder to detect.

The predictions of the numerical models lead to the conclusion that the multiaxial stress state in a thick-walled pressure vessel can potentially lead to its failure at a lower pressure than would be expected from the tensile strength of a unidirectional composite. The work presented in this thesis provides important arguments that this is the case, but further investigation is necessary. The improved understanding of the damage processes in pressure vessels will allow the manufacturers to produce more reliable and more efficient structures, leading to weight and cost savings, as well as reducing pollutant emissions.

Chapter 8

Conclusions

Chapitre 8. Conclusions

Les travaux présentés dans ce document visent à proposer une approche améliorée pour simuler le comportement mécanique des réservoirs composites renforcés par des fibres de carbone. Cette approche, développée dans le cadre du modèle de rupture des fibres de Blassiau et al., exploite des techniques expérimentales de caractérisation morphologiques à différentes échelles du matériau ainsi que des développements numériques spécifiques.

Le premier sujet discuté est la définition d'un domaine élémentaire représentatif (DER) du phénomène microscopique de rupture des fibres. Dans le Chaptire 3, ce problème est analysé par une étude numérique. Un domaine de 36 fibres d'une longueur de 4 mm est identifié comme suffisant pour représenter le DER.

Une majeure partie des travaux présentés dans ce mémoire s'intéresse à l'influence des porosités sur la résistance des réservoirs composites à haute pression. Des observations en tomographie aux rayons X et en microscopie optique ont été réalisées au sein d'un réservoirs à parois épaisses (Chapitre 4). Un taux de porosité d'environ 3 % est observé et les formes et tailles des vides sont caractérisées morphologiquement.

Le Chapitre 5 où des essais en traction sont réalisés sur des éprouvettes à double entaille permet de montrer que l'amorçage de rupture est amené par un défaut critique et le site d'amorçage dépend de la triaxialité des contraintes. La croissance des cavités est tracée à l'aide des observations tomograhiques et microscopiques, qui sont en suite utilisées afin d'optimiser un modèle par éléments finis de type Gurson-Tvergaard-Needleman. Cela permet de proposer un critère de rupture fragile de la résine époxy.

L'étude expérimentale de l'effet des cavités sur la résistance en traction d'un matériau composite carbone-époxy fait l'objet du Chapitre 6. Des stratifiés à plis croisés à différents taux de porosité sont fabriqués en modifiant le cycle de durcissement. Les essais en traction montrent une réduction limitée de la contrainte à rupture à cause des vides. Des essais biaxiaux sont en suite réalisés sur un système expérimental spécialement conçu afin d'imiter l'état des contraintes au sein d'un réservoir à parois épaisses. On observe que la compression dans le sens de l'épaisseur réduit la résistance en traction du matériau. Cet effet est plus prononcé pour des éprouvettes à taux de porosité élevé.

Dans le Chapitre 7, des modifications au modèle multiéchelle de rupture des fibres sont proposées, prenant en compte les résultats expérimentaux obtenus précédemment. Deux approches permettant de modéliser des porosités macroscopiques sont présentées, ainsi qu'un critère biaxial phénoménologique de rupture des fibres. La simulation d'un réservoir composite à parois épaisses montre que ces facteurs peuvent réduire la pression d'éclatement de l'ordre d'une dizaine de pourcents, dépendant de la géométrie du réservoir.

Plusieurs sujets abordés dans cette thèse mériteraient d'être approfondis. C'est par exemple l'effet des cavités sur le transfert de charges autour d'une fibre rompue à l'échelle microscopique. Le modèle numérique d'époxy permet de réaliser des simulations micro-mécaniques de ce type de problèmes.Une caractérisation améliorée de la croissance des cavités dans l'époxy peut être accomplie en utilisant la tomographie in situ aux rayons X. En plus, des essais sur des éprouvettes à différents rayons de fond d'entaille et à différentes vitesses permettraient une meilleure compréhension de l'effet des contraintes multiaxiales et du temps.

L'effet de la température est peut être le facteur le plus important qui devrait être inclut dans la modélisation multiéchelle de rupture longitudinale, ceci afin d'améliorer les prédictions de durée de vie des réservoirs composites qui voient de grandes variations de températures. Un autre défi est l'application du modèle aux structures de taille réelle. En ce moment, une telle simulation est très coûteuse numériquement. Des travaux sont en cours pour surmonter ce problème en utilisant la méthodologie introduite dans le Chapitre 3 [171].

8.1 Main results

In the presented thesis, experimental and numerical techniques have been used to propose an improved approach to predicting strength of fibre-reinforced composite pressure vessels, developed in the framework of an existing multiscale fibre break model of Blassiau et al. [9]. Initially, the model is critically evaluated to analyze how well-suited it is for simulating burst of fibre-reinforced pressure vessels and what factors need to be further addressed. It is concluded that a reliable simulation of the fibre break accumulation phenomenon under longitudinal tensile loading is crucial to accurate strength prediction.

The first addressed problem is the definition of a three-dimensional representative domain element (RDE) of the fibre break accumulation process happening at the microscale in a fibre-reinforced composite subjected to longitudinal tension. In Chapter 3, a mathematical framework is introduced, tying the choice of RDE to the concepts of a stochastic ergodic random function and integral range. An extensive campaign of numerical experiments is carried out, studying the fibre break process in microscopic domains of different shapes and sizes. It includes the scatter in composite strength by taking into account the stochastic character of carbon fibre strength. It is shown that a regular square array of 36 fibres of 4 mm length can be used as a RDE of the fibre break process. The fibre break topology analysis shows that in that volume fibre break clustering phenomenon occurs in a single plane. This justifies the assumption of a single fibre break plane in an RDE used by Blassiau [9].

A major part of the thesis is dedicated to the study of the influence of voids on the strength of carbon fibre reinforced composites and, in particular, composite pressure vessels. Chapter 4 presents experimental observations of a thick-walled carbon-epoxy pressure vessel, using X-ray tomography and optical microscopy. The observations confirmed that filament-wound structures can show a relatively high void content. Image processing techniques were used to characterize individual voids in the tomography volumes. An algorithm was developed and implemented, allowing an automatic measurement of composite ply orientation. The results showed that voids in composite plies are predominantly elongated along fibre direction and can be quite large, with cross-sectional dimensions of multiple fibre diameters. The resolution of the tomography results was not sufficient to observe some smaller voids. Optical microscopy observations were additionally carried out, showing some smaller voids, with dimensions close to fibre diameter. Void content measurement was carried out both on the tomography volumes and the micrographs. It was concluded that the void area fraction measured from optical microscopy images can provide a reasonable estimate of the void volume fraction in the composite.

Next to larger elongated voids discussed above, the matrix in a composite material contains microscopic, approximately spherical voids. This type of cavities is investigated in Chapter 5, using experimental and numerical techniques to

study a thermosetting epoxy resin. Double-notched round epoxy specimens are manufactured and tested in tension. Failure is localized at the notch, where a multiaxial stress state is present, mimicking that in a necking smooth specimen. Using two notches means that the unbroken notch is unloaded very shortly prior to failure, which is otherwise hard to achieve for a brittle material of this type.

Two types of observations are carried out after mechanical testing: synchrotron radiation computed tomography (SRCT) of the unbroken notches and scanning electron microscopy (SEM) of the fracture surfaces. SEM observations reveal that the location of the fracture initiation site is controlled by the notch root radius, pointing to the importance of stress triaxiality. Failure is shown to initiate from a critical defect, often in the form of a void or a cluster of voids. The position and volume of individual voids are classified from the SEM and SRCT observations, showing proof of void growth in the epoxy. Void growth data is used to optimize a Gurson-Tvergaard-Needleman finite element model. Finally, a failure criterion is discussed, showing that brittle failure of epoxy can be predicted through a combination of a critical value of the maximum principal stress and a critical defect.

In Chapter 6, an experimental study is performed to evaluate the longitudinal tensile strength of a unidirectional composite with a high void content. Test specimens are obtained from autoclave-manufactured cross-ply carbon-epoxy specimens. Low voidage material is obtained using the recommended curing cycle. High voidage specimens are obtained by lowering the curing pressure. Tensile tests show that an increase in void content lead to a moderate decrease in stiffness and tensile strength, while the strain at failure is not affected.

To mimic the stress state in a thick-walled pressure vessel, a through-thickness compressive load is considered in addition to longitudinal tension. This type of biaxial test on a representative material is proposed, since direct testing of pressure vessels is costly and offers limited possibilities of in situ damage monitoring. A custom compression system is designed and manufactured, allowing tensile testing with a locally applied through-thickness compression. For all levels of compression, failure of the longitudinal plies remains fibre-break dominated. However, the subsequent finite element analysis shows that applying compression reduces the value of the longitudinal tensile stress at failure. Furthermore, for this effect is more pronounced for the high voidage material. These results indicate that a uniaxial maximum stress criterion, commonly used to predict tensile strength of unidirectional composite, might lead to overpredicting the burst pressure of thick-walled pressure vessels.

The experimental results are used to propose extensions to the fibre break model of Blassiau et al., as described in Chapter 7. Voids are modelled at the macroscale using two methods. In the first one, the elastic coefficients of the unidirectional ply are modified according to the generalized self-consistent scheme. In the second

approach, the voids are meshed explicitly. Additionally, a phenomenological biaxial fibre break criterion is proposed, based on the test results presented in Chapter 6. Numerical simulations of a thick-walled pressure vessel pressurization show that the through-thickness stress component may lead to a significant decrease in burst pressure.

8.2 Perspectives

In the work presented in this thesis, the influence of voids in the composite material has been taken into account at the macroscale. This approach does not account for the micromechanical phenomena, such as the difference in load transfer around individual fibre breaks caused by void presence. The work of Scott et al. [137] showed a correlation between fibre break density and distance from the nearest void in a carbon-epoxy composite. A smaller fibre-matrix interface area adjacent to voids can lead to a longer recovery length around a fibre break, thus increasing a probability of a new break in the surrounding fibres. The numerical model of epoxy introduced in Chapter 5 can be used to carry out micromechanical simulations of this and other problems, taking into account a local stress state in a realistic microstructure [123].

The study on void growth in epoxy, described in Chapter 5, is based on ex situ measurements in different regions of notched specimens. An improved measurement of void growth in epoxy can be achieved thanks to the recent advances in X-ray tomography, allowing in situ observations at a very high resolution [82]. Tests on specimens with different notch root radii would allow an improved understanding of the influence of stress triaxiality. More tests at different loading speeds are necessary to better evaluate the time-dependent behaviour of epoxy.

The influence of multiaxial stress states on the fibre-dominated failure, addressed in Chapter 6, merits further investigation. While the methodology used in this thesis clearly shows the decrease in tensile strength due to through-thickness compression, the accurate computation of local stresses is not straightforward, especially for the specimens with a high void content. Tensile tests with a superposed hydrostatic pressure could be an interesting option.

As mentioned in Chapter 1, another important factor that should be addressed in composite tensile failure simulation is the influence of hygrothermal effects, and especially that of temperature. This is not a straightforward task. For instance, at elevated temperatures, the matrix loses a large part of its load bearing capability. This has a significant influence on the formation of larger fibre break i-plets. Above the glass transition temperature, the mechanism of the fibre accumulation process, as presented in Section 1.2.3, is significantly modified. Taking into account temperature is important for accurate strength prediction of composite cylinders.

An important challenge is to extend the use of the fibre break model of Blassiau et al. to large structures. While the multiscale framework allows simulating problems larger than for a purely micromechanical approach, running computations for a full scale pressure vessel is still a challenge. It has been suggested that applying the methodology presented in Chapter 3, it is possible to obtain equivalent results by applying the fibre break model to a subvolume of a pressure vessel [171].

Appendices

Appendix A

Measurement of fibre volume fraction from micrographs

The optical microscopy images obtained from the type 3 CFRP pressure vessel (Chapter 4) allow an analysis of fibre volume fraction in the hoop plies. Since the topic of fibre volume fraction distribution is not further addressed in the thesis, the results are presented in this appendix.

Fibre volume fraction is evaluated from grayscale micrographs taken at 200× magnification. For the purposes of these measurements, fibre volume fraction is defined as fibre area with respect to the total area of the micrograph, including fibres, matrix and voids. Only the hoop plies are considered, where the fibres are perpendicular to the view plane. The histogram of the pixel intensity values is analyzed to find the values corresponding to fibres and the images are binarized by global thresholding. A detail of a typical grayscale image and its corresponding histogram is shown in Figure A.1. A pixel intensity threshold of 121 is obtained by means of the global Minimum auto-threshold algorithm implemented in Fiji [126]. The choice of the threshold is arbitrary to an extent, since the transition between the fibre and the matrix phase in the image is gradual, as visible from the grayscale profile shown in Figure A.2. This highlights that a more reliable method of computing fibre volume fraction is necessary.

To solve the problem of high uncertainty of fibre volume fraction measurement using the grayscale thresholding approach, a fibre counting method is used [167]. If the number of fibres in a considered area is known, the fibre volume fraction can be evaluated from the formula

$$V_f = \frac{N_f A_f}{A_{tot}}, \tag{A.1}$$

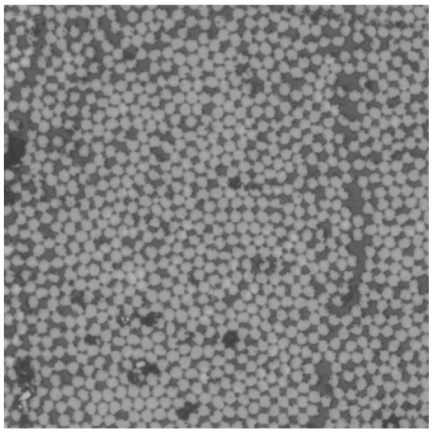

(a) Detail of a micrograph in grayscale.

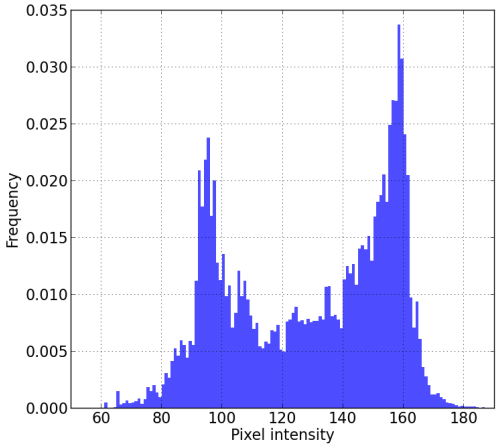

(b) Corresponding pixel intensity histogram.

Figure A.1: Fibre volume fraction: grayscale image and its pixel intensity.

where N_f is the number of fibres in the studied region, A_{tot} is the surface area of that region and A_f is the cross-sectional area of a single fibre, given by

$$A_f = \frac{\pi d_f^2}{4}. \tag{A.2}$$

Since the diameter of carbon fibres shows little scatter [71], using an average fibre diameter for all fibres is expected to provide reliable results. Some error is introduced by fibres located only partially in the measurement region. However, this error is negligible, as long as the measurement is carried out over a large surface.

An image analysis algorithm is implemented in Fiji to automatically count the number of fibres in a micrograph. First, the grayscale image is thresholded with a global threshold value of 130 found by Otsu's method [115]. This leads to less overlap between fibres in the segmented image compared with the Minimum method, which facilitates distinguishing individual fibres. The "Watershed" method implemented in Fiji is then applied to the binary image, which separates touching fibres. Finally, the number of fibres is obtained through the "Analyze Particles" function. A minimum size of the particle is set to half of the fibre area defined by Equation A, in order to avoid erroneous identification of smaller particles as fibres.

Table A.1 shows the fibre volume fraction calculated for the two analyzed hoop plies. Grayscale thresholding, believed to be less accurate, underpredicts the volume fraction in both cases. The results of the fibre counting method show that the fibre volume fraction is higher near the cylinder interior. Such tendency has been reported in the literature [34] [135]. Therefore, an accurate analysis of ply level stress in a

pressure vessel requires taking into account the non-uniform distribution of fibre volume fraction between plies.

	Thresholding	Fibre counting
Hoop ply 1	57.4%	62.8%
Hoop ply 2	56.2%	58.6%

Table A.1: Fibre volume fraction in the first and second hoop ply obtained by two image analysis methods. Hoop ply 1 is the innermost composite layer. Hoop ply 2 is located at approximately mid-thickness of the cylinder wall.

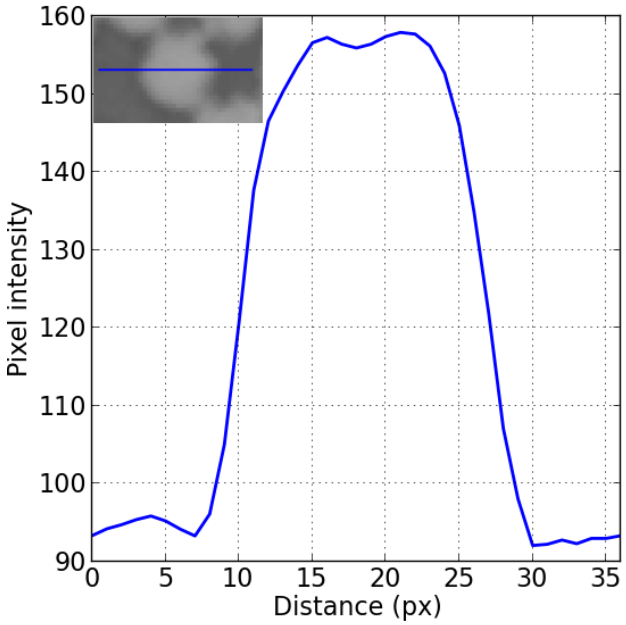

Figure A.2: A typical grayscale profile across a fibre-matrix boundary. The insert in the top left corner shows the location of the line along which the intensity profile is plotted.

Appendix B

Finite element analysis of the stress state in a thick-walled CFRP pressure vessel

B.1 Methods

Based on X-ray tomography and optical microscopy observations presented in Chapter 4, a numerical model of the type 3 thick-walled pressure vessel is built. The FFT image analysis algorithm introduced in Section 4.3 is used to measure ply thickness and orientation. The composite material in the pressure vessel is modelled as a sequence of unidirectional plies, with orientations listed in Table B.1. All plies are assigned the same material properties, listed in Table B.2. The aluminium liner is modelled as linear isotropic, with a linear hardening law. The initial Young's modulus is $E = 68.9\,\mathrm{GPa}$. After reaching the von Mises yield stress of 270 MPa, the new Young's modulus is 694 MPa. Taking into account the plasticity of the liner allows analyzing the effect of autofrettage. This procedure, used mostly to increase the fatigue resistance of the liner, leads to the appearance of important residual stresses in the composite [135]. Other advantages of autofrettage include improving the interface between the liner and composite through mechanical locking and closing the gap between the two that could appear after curing due to mismatch in thermal expansion coefficients [65]. The internal pressure loading sequence is shown in Figure B.1. At first, the cylinder is pressurized to 1655 bar, corresponding to the autofrettage pressure. Next, pressure is completely released. Then, the cylinder is pressurized again up to 2655 bar.

ply No	liner	1	2	3	4	5	6	7	8
angle	-	90°	±70°	±25°	±45°	±15°	90°	±15°	90°
thickness (mm)	5.0	6.0	1.0	1.0	2.5	2.0	4.5	7.0	1.0

Table B.1: Ply orientation and thickness used in the numerical model. The angle is measured with respect to the cylinder axis, i.e. hoop direction corresponds to 90°.

E_{11}	$E_{22} = E_{33}$	$\nu_{12} = \nu_{13}$	ν_{23}	$G_{12} = G_{13}$
180.5 GPa	6.2 GPa	0.29 -	0.40 -	5.2 GPa

Table B.2: Properties of a UD ply used for the pressure vessel simulation.

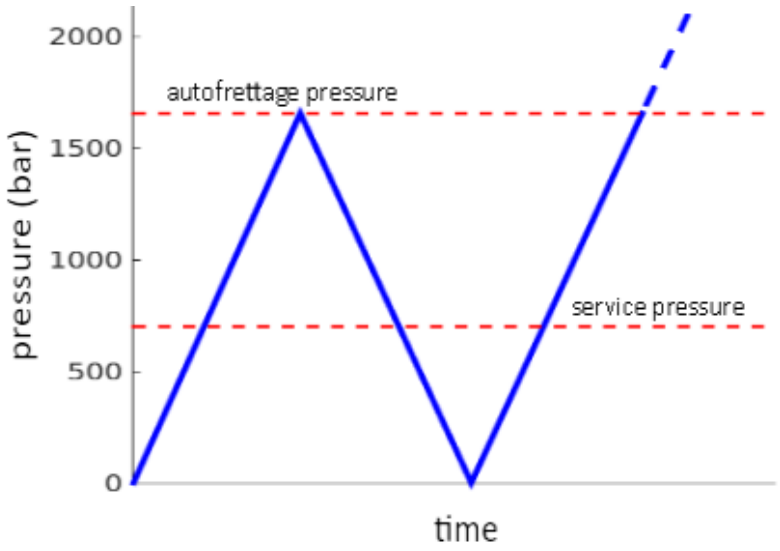

Figure B.1: Loading sequence used in the finite element simulation.

B.2 Results

Figure B.2 shows the computed values of stress in the different layers of the pressure vessel in the cylindrical section. Three components of stress are shown: hoop, axial and through-thickness. During the autofrettage stage, the aluminium liner reaches its yield stress and undergoes irreversible deformation. As shown in Figure B.2c, this leads to the presence of a compressive stress in the liner upon unloading, with a predicted value in the hoop direction of approximately −300 MPa. At the same time, a residual tensile stress appears in the composite plies, highest in the innermost hoop ply (Ply 1). Comparing the stresses at service pressure before (Figure B.2a) and after autofrettage (Figure B.2d), shows that not taking this process into account

could lead to underestimation of stresses in the composite plies. However, this effect becomes less important for higher pressures and disappears completely upon reaching again the autofrettage pressure (Figure B.2e).

The simulation shows that the maximum principal stress corresponds to axial tension (σ_{11}) and its value is highest in the hoop plies. The innermost hoop ply is the most loaded one, with a longitudinal stress approximately 20 % higher from that in the second most loaded ply. If a higher fibre volume fraction in the inner ply was taken into account (see Appendix A), this difference would be even more pronounced. It can be therefore predicted that the final failure will be triggered in this ply. This agrees well with experimental observations of Scott [135], who observed a much higher number of fibre breaks in the inner hoop ply using µCT. The second highest stress component in the hoop plies is σ_{33}, corresponding to through-thickness compression. Its value is highest on the internal surface of the cylinder and descends approximately linearly toward the outside, until falling to zero on the external surface. In the most loaded hoop ply, the absolute value of σ_{33} is equal to approximately 7% of the axial tensile stress. This value is large enough to be considered non-negligible. For thicker cylinders, even higher ratios of σ_{33}/σ_{11} are possible.

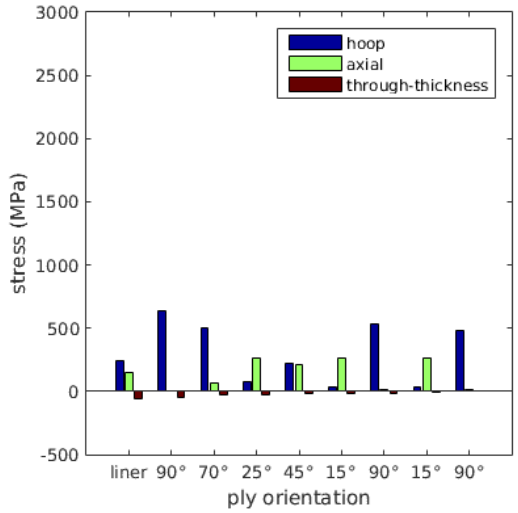

(a) 700 bar, before autofrettage.

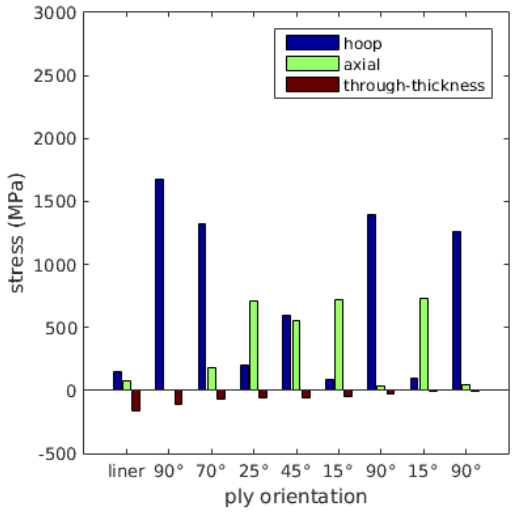

(b) Autofrettage (1655 bar).

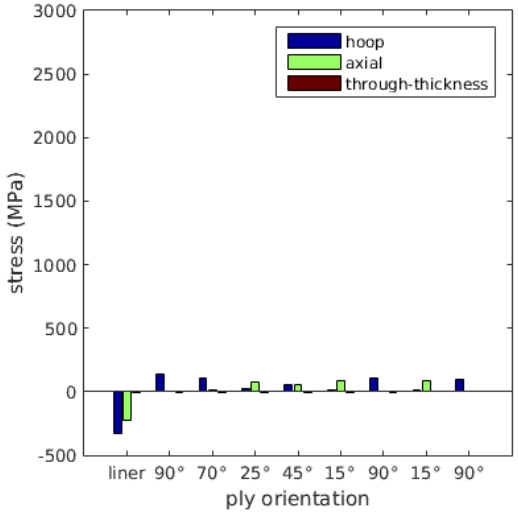

(c) 0 bar, after autofrettage.

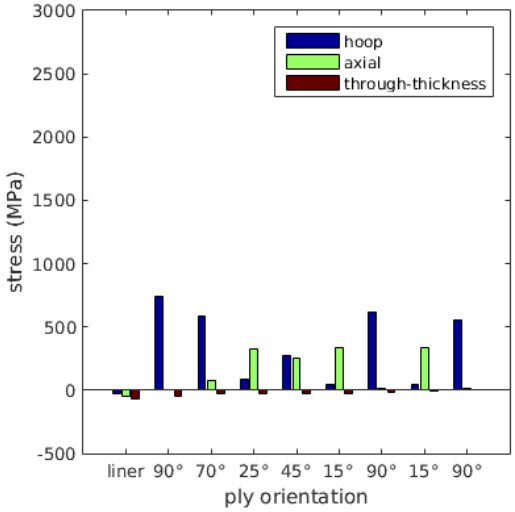

(d) 700 bar, after autofrettage.

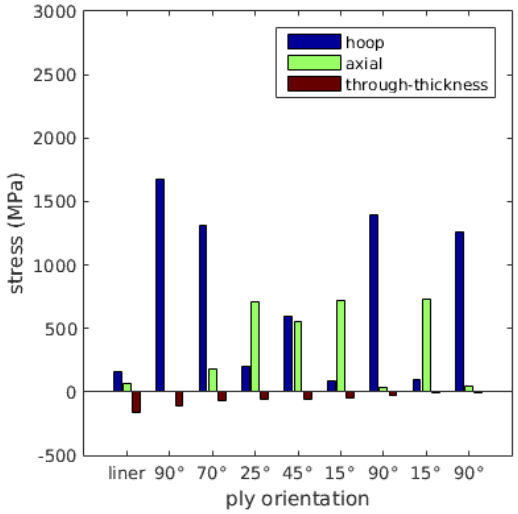

(e) 1655 bar, after autofrettage.

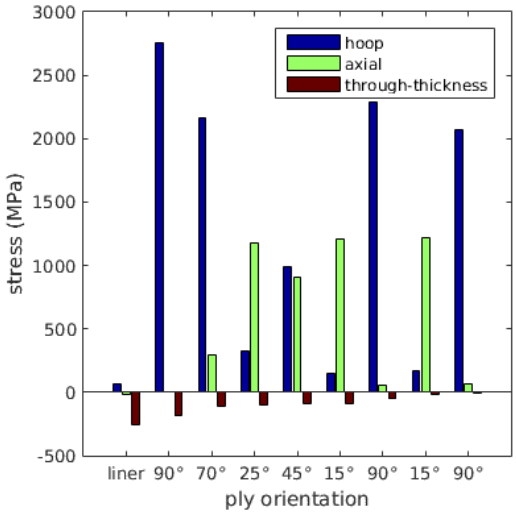

(f) 2655 bar, after autofrettage.

Figure B.2: Computed stresses at various stages of pressure vessel pressurization. For the liner, the hoop direction stress is shown.

Appendix C

Damage development in cross-ply carbon-epoxy specimens under tensile loading

Mechanical tests on low and high-voidage specimens are discussed in Chapter 6. In this appendix, complimentary information on damage development under tensile loading is provided, with a focus on the influence of macroscopic voids.

C.1 Fracture surfaces

Scanning Electron Microscopy (SEM) was used to observe the fracture surfaces of selected specimens after tensile testing. An Au/Pd coating was applied to improve the electrical conductivity of the specimens. Figure C.1a shows the surface of a fibre in a longitudinal ply after failure. It is still mostly covered in resin, which implies high quality of the fibre-matrix interface and, by extension, an effective stress transfer around broken fibres. Fracture surfaces of fibres in the 0° ply are mostly flat, with an easily identifiable fracture initiation site, surrounded by a propagating hackle pattern. This type of fracture surface is typical of brittle failure and bears resemblance to that observed in notched epoxy specimens discussed in Chapter 5. The initiation site is predominantly located on fibre surface, as shown in Figures C.1b and C.1c. This indicates that surface flaws are the dominant factor in fibre failure. This might be due to the location of the critical flaws, but also due to the fact that the stress generated by a fibre break on an adjacent intact fibre is not uniform, but its value is highest on the surface facing the break [106] [46] [174] [149] [175]. In some cases, the hackle pattern orientation on neighbouring fibres allows deducing the failure sequence. In Figure C.1b, it can be seen that three adjacent fibres failed from the direction of a neighbouring cross-ply (on the right side of the figure). In

Figure C.1c, two fibres near the lower left edge of the image broke at a point where they were in contact with each other. That led to a cascade-like failure of three neighbouring fibres (toward upper right of the figure).

C.2 Damage development observation

Two low-voidage and two high-voidage specimens were loaded in tension at a constant cross-head spead of 1 mm/min, with several intermediate load hold phases. During the hold phases, a 30 mm length of the polished lateral edge was mapped using a digital microscope at 100× magnification, in order to observe damage development, in particular matrix cracking in the transverse plies. The number of cracks at each load level was counted and classified by the transverse ply in which they occurred. The plies are referred to by numbers from 1 to 4, where plies 1 and 4 are closer to the specimen surface.

Transverse cracking is usually the first damage mechanism observed in cross-ply composite specimens loaded in tension [151]. After reaching a certain strain, cracks start appearing at random locations in the transverse plies. They propagate through the width and thickness of the specimen, in a plane perpendicular to the loading direction. Here, transverse cracking is analyzed in the specimens tested with intermittent hold phases. Significant differences in the cracking process are present between the specimens with different void contents. Figure C.2 shows the evolution of crack density measured from a single specimen of each type. Each line corresponds to the crack density measured in one transverse ply. In the low void content specimen, first cracks appear at 50 % to 60 % of ultimate tensile strength (UTS). The number of cracks increases at higher strains, but even shortly prior to failure their locations are mostly random. The low number of recorded cracks can be attributed to the relatively low thickness of the plies. Reduction in transverse ply thickness is known to lead to a lower crack density [118].

Figure C.3 illustrates three stages of damage development in a high voidage specimen. At first, cracks appear exclusively at voids. The stress threshold is much lower than for the low voidage specimen, at approximately 30 % UTS. The reduction of the cracking threshold due to void presence has been well documented in the literature [69] [145] [1] [98]. From the micrographs it cannot be said if the cracks span the whole width of the specimen, but other authors show that this type of void-induced cracks is at first localized on the free edge [139] [98]. Similar tendency for free edge cracking onset was observed in specimens without intentionally introduced voids [133] [79]. At stress levels close to failure, cracks start appearing away from the voids visible on the surface. In some cases, it can be seen that new cracks appear at the same position along specimen length as the already existing cracks in other

plies. An example of this can be seen in Figure C.3c. This can be explained by stress redistribution in the plane of the first crack.

Figure C.4 shows a detail of a high voidage specimen photographed at high magnification before applying a tensile load and then shortly prior to failure. Four transverse cracks are observed in the field of view. The first crack formed at a void and propagated gradually until spanning the whole ply thickness. The other cracks, not passing through voids, appeared instantaneously between two frame acquisitions. Multiple fibre breaks are visible in the longitudinal plies. However, the high number of fibre breaks could be caused by the local reduction of fibre diameter on the surface due to polishing. No correlation is observed between the location of transverse cracks and fibre break density. The appearance of transverse cracks does not have an effect on the macroscopic stiffness of the specimen. This is attributed to the low ratio of transverse to longitudinal stiffness of a unidirectional CFRP. It can be therefore assumed that transverse plies have a negligible effect on the tensile strength of the cross-ply laminate [110]. Therefore, the strength of the laminate is believed to depend almost exclusively on the strength of the 0° plies.

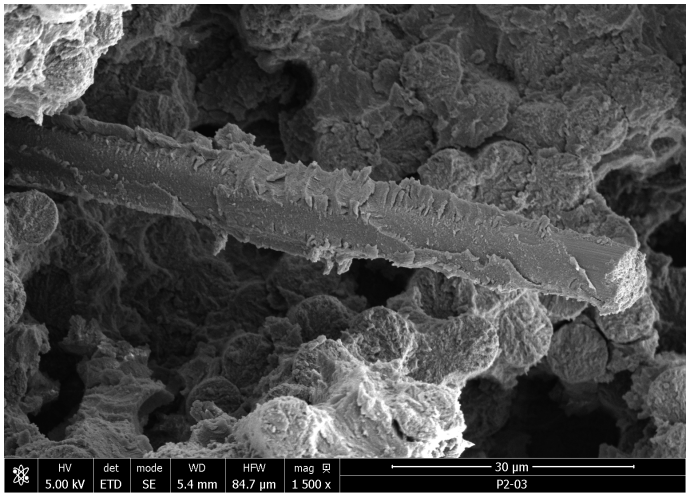

(a) Fibre pulled out from a 0° ply.

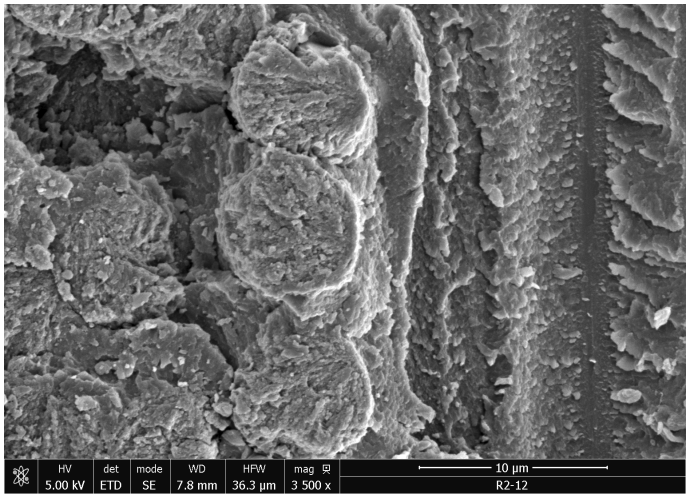

(b) Fracture of fibres in a longitudinal ply (left) originating from the direction of an adjacent transverse ply (right).

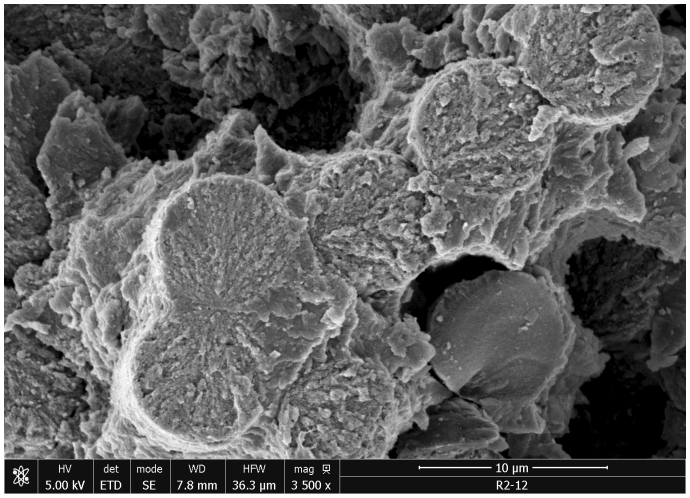

(c) Fracture initiation at a contact point between fibres.

Figure C.1: SEM fractography: CFRP cross-ply specimens after tensile failure.

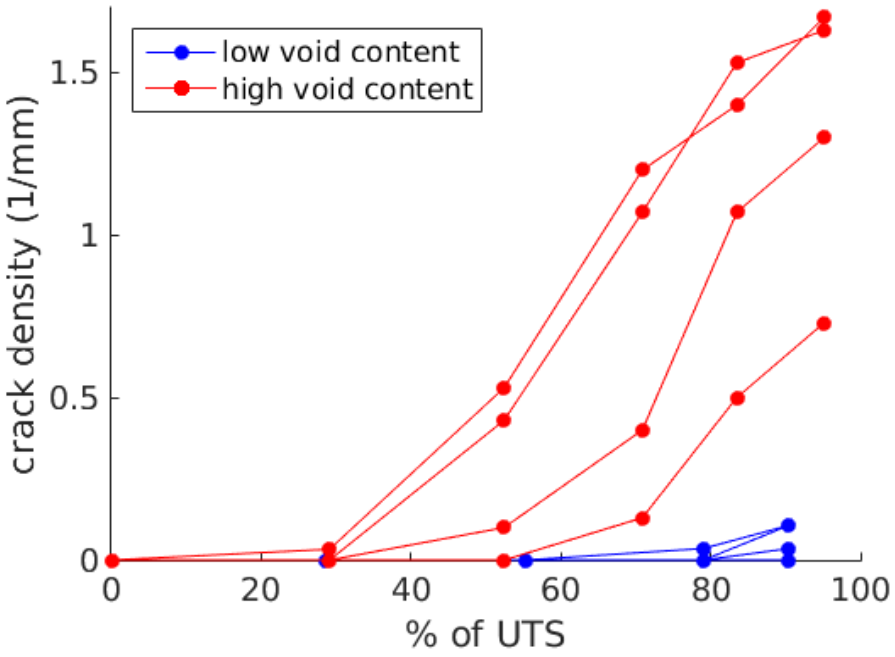

Figure C.2: Crack density evolution in a high and low-voidage specimen as a function of stress. Each line corresponds to a single transverse ply (four per specimen). The cracks were counted along a 300 mm length of the lateral edge of the specimens.

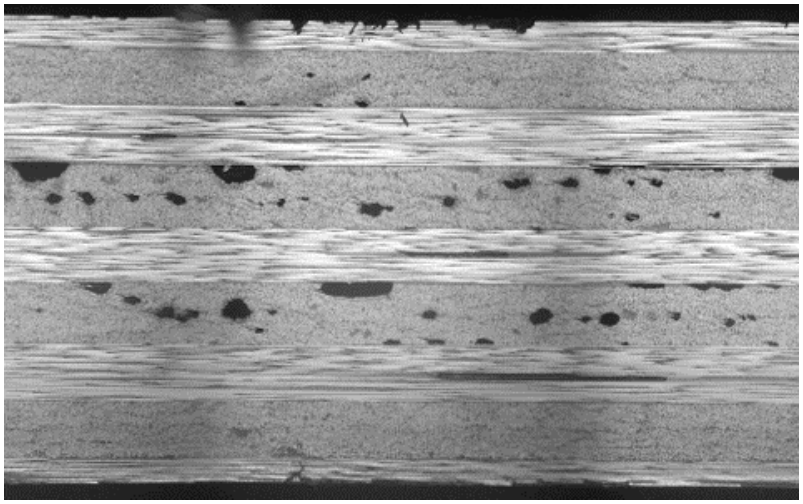

(a) 0% UTS.

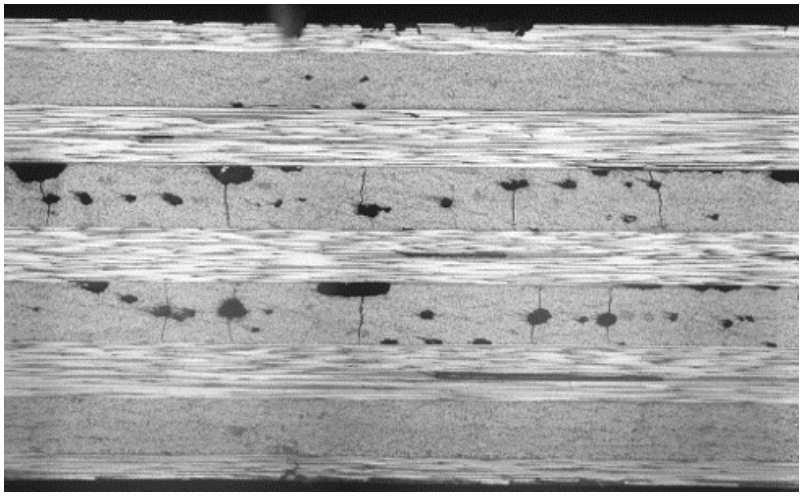

(b) 68% UTS.

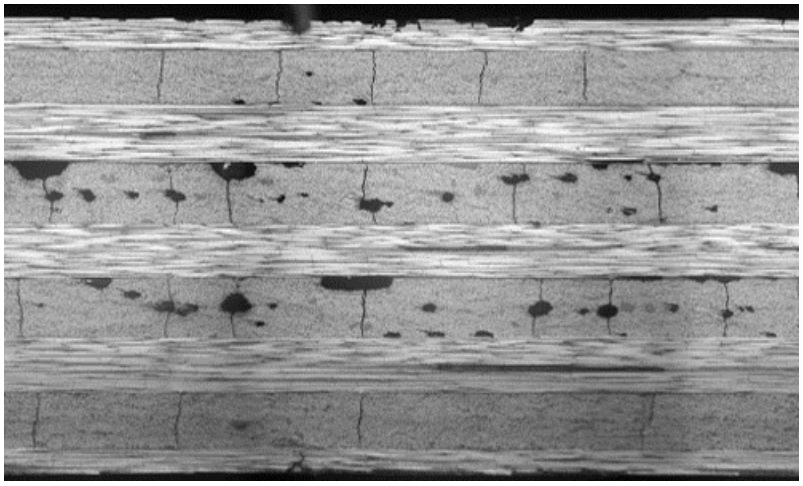

(c) 97% UTS.

Figure C.3: A representative high-voidage specimen: transverse crack evolution under tensile loading applied in the horizontal direction of the image. Stress is provided as a percentage of the ultimate tensile strength (UTS). Load is applied in the horizontal direction of the image. Failure occurred at 1034 MPa.

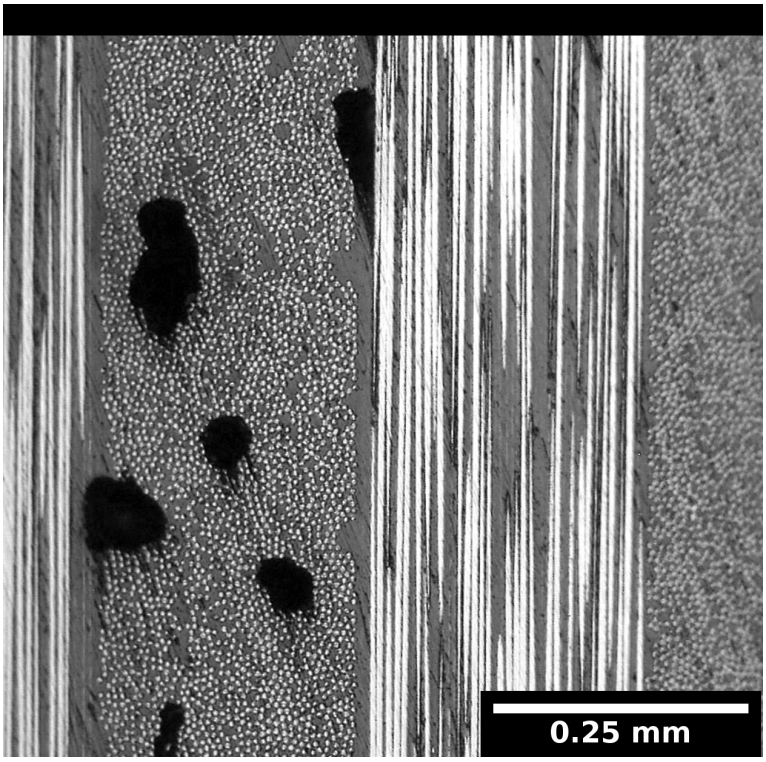

(a) Pristine state.

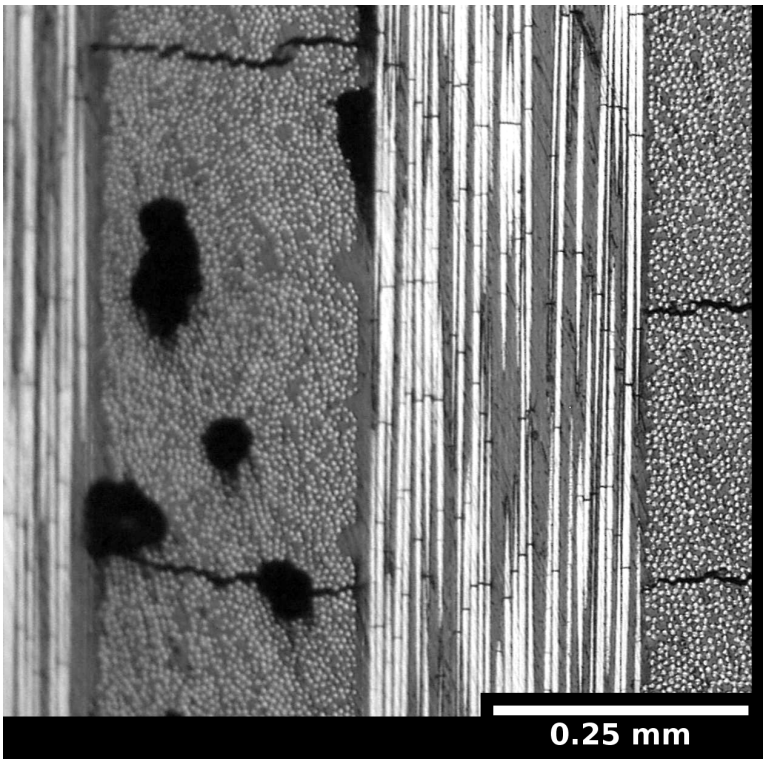

(b) State shortly before failure.

Figure C.4: Digital microscopy of damage evolution on the lateral edge of a high-voidage specimen under tensile loading applied in the vertical direction of the image. Transverse cracks and fibre breaks can be seen.

Bibliography

[1] S. Aratama, R. Hashizume, K. Takenaka, K. Koga, Y. Tsumura, T. Miyake, M. Nishikawa, and M. Hojo. Microscopic observation of voids and transverse crack initiation in CFRP laminates. *Advanced Composite Materials*, 25(sup1):115–130, 2016.

[2] C. Baxevanakis. *Comportement statistique à rupture des composites stratifiés*. PhD thesis, Ecole des Mines de Paris, 1994.

[3] S. Behzadi, P.T. Curtis, and F.R. Jones. Improving the prediction of tensile failure in unidirectional fibre composites by introducing matrix shear yielding. *Composites Science and Technology*, 69(14):2421 – 2427, 2009.

[4] S.C. Bennett, D.J. Johnson, and W. Johnson. Strength-structure relationships in PAN-based carbon fibres. *Journal of Materials Science*, 18(11):3337–3347, 1983.

[5] Y. Benveniste. A new approach to the application of Mori-Tanaka's theory in composite materials. *Mechanics of Materials*, 6(2):147 – 157, 1987.

[6] J. Besson and R. Foerch. Large scale object-oriented finite element code design. *Computer Methods in Applied Mechanics and Engineering*, 142(1):165 – 187, 1997.

[7] J. Besson, D. Steglich, and W. Brocks. Modeling of crack growth in round bars and plane strain specimens. *International Journal of Solids and Structures*, 38(46):8259 – 8284, 2001.

[8] S. Beucher. *Segmentation d´images et morphologie mathematique*. PhD thesis, Ecole des Mines de Paris, 1990.

[9] S. Blassiau. *Modélisation des phénomènes microstructuraux au sein d'un composite unidirectionnel carbone/epoxy et prédiction de durée de vie: Contrôle et qualification de réservoirs bobinés*. PhD thesis, Ecole des Mines de Paris, 2005.

[10] S. Blassiau, A. Thionnet, and A. Bunsell. Micromechanisms of load transfer in a unidirectional carbon-fibre epoxy composite due to fibre failures. Part 1: Micromechanisms and 3D analysis of load transfer, the elastic case. *Composite Structures*, 74:303–318, 2006.

[11] S. Blassiau, A. Thionnet, and A. Bunsell. Micromechanisms of load transfer in a unidirectional carbon-fibre epoxy composite due to fibre failures. Part 2: Influence of viscoelastic and plastic matrices on the mechanism of load transfer. *Composite Structures*, 74:319–331, 2006.

[12] S. Blassiau, A. Thionnet, and A. Bunsell. Micromechanisms of load transfer in a unidirectional carbon-fibre epoxy composite due to fibre failures. Part 3: Multiscale reconstruction of composite behaviour. *Composite Structures*, 83:312–323, 2008.

[13] M. Bodaghi, C. Cristóvão, R. Gomes, and N.C. Correia. Experimental characterization of voids in high fibre volume fraction composites processed by high injection pressure RTM. *Composites Part A: Applied Science and Manufacturing*, 82:88–99, 2016.

[14] G. Boisot, L. Laiarinandrasana, J. Besson, C. Fond, and G. Hochstetter. Experimental investigations and modeling of volume change induced by void growth in polyamide 11. *International Journal of Solids and Structures*, 48(19):2642 – 2654, 2011.

[15] P.W. Bridgman. The stress distribution at the neck of a tension specimen. *Transactions ASM*, 32:553–574, 1944.

[16] B. Budiansky. On the elastic moduli of some heterogeneous materials. *Journal of the Mechanics and Physics of Solids*, 13(4):223 – 227, 1965.

[17] R.E. Bullock. Strength ratios of composite materials in flexure and in tension. *Journal of Composite Materials*, 8(2):200–206, 1974.

[18] A. Bunsell, L. Gorbatikh, H. Morton, S. Pimenta, I. Sinclair, M. Spearing, Y. Swolfs, and A. Thionnet. Benchmarking of strength models for unidirectional composites under longitudinal tension. *Composites Part A: Applied Science and Manufacturing*, 111:138 – 150, 2018.

[19] A.R. Bunsell, S. Joannès, and A. Marcellan. 2 - testing and characterization of fibers. In Anthony R. Bunsell, editor, *Handbook of Properties of Textile and Technical Fibres (Second Edition)*, The Textile Institute Book Series, pages 21–55. Woodhead Publishing, second edition edition, 2018.

[20] S.G. Burnay and J.V. Sharp. Defect structure of PAN-based carbon fibres. *Journal of Microscopy*, 97(1-2):153–163, 1973.

[21] W.J. Cantwell, A.C. Roulin-Moloney, and T. Kaiser. Fractography of unfilled and particulate-filled epoxy resins. *J. Mater. Sci.*, 23(5):1615–1631, 1988.

[22] H.-A. Cayzac, K. Saï, and L. Laiarinandrasana. Damage based constitutive relationships in semi-crystalline polymer by using multi-mechanisms model. *International Journal of Plasticity*, 51:47 – 64, 2013.

[23] M. Challier, J. Besson, L. Laiarinandrasana, and R. Piques. Damage and fracture of polyvinylidene fluoride (PVDF) at 20 degree C: Experiments and modelling. *Eng. Fract. Mech.*, 73:79 – 90, 2006.

[24] L.-P. Chao and J.H. Huang. Prediction of elastic moduli of porous materials with equivalent inclusion method. *Journal of Reinforced Plastics and Composites*, 18(7):592–605, 1999.

[25] H.S Choi, K.J Ahn, J.-D Nam, and H.J Chun. Hygroscopic aspects of epoxy/carbon fiber composite laminates in aircraft environments. *Composites Part A: Applied Science and Manufacturing*, 32(5):709 – 720, 2001.

[26] H.Y. Chou. *Damage Analysis of Composite Pressure Vessels Using Acoustic Emission Monitoring*. PhD thesis, RMIT University, 2011.

[27] H.Y. Chou, A.R. Bunsell, G. Mair, and A. Thionnet. Effect of the loading rate on ultimate strength of composites. application: Pressure vessel slow burst test. *Composite Structures*, 104:144 – 153, 2013.

[28] R. Christensen, H. Schantz, and J. Shapiro. On the range of validity of the mori-tanaka method. *Journal of the Mechanics and Physics of Solids*, 40(1):69 – 73, 1992.

[29] R.M. Christensen. A critical evaluation for a class of micro-mechanics models. *J. Mech. Phys. Solids*, 38(3):379 – 404, 1990.

[30] R.M. Christensen and K.H. Lo. Solutions for effective shear properties in three phase sphere and cylinder models. *Journal of the Mechanics and Physics of Solids*, 27(4):315 – 330, 1979.

[31] D. Cohen. Application of reliability and fiber probabilistic strength distribution concepts to composite vessel burst strength design. *Journal of Composite Materials*, 26(13):1984–2014, 1992.

[32] D. Cohen. Pressurized ring test for composite pressure vessel hoop strength and stiffness evaluation. *Journal of Composites, Technology and Research*, 17(4):331–340, 1995.

[33] D. Cohen. Influence of filament winding parameters on composite vessel quality and strength. *Composites Part A: Applied Science and Manufacturing*, 28(12):1035 – 1047, 1997.

[34] D. Cohen, S.C. Mantell, and L. Zhao. The effect of fiber volume fraction on filament wound composite pressure vessel strength. *Composites Part B: Engineering*, 32:413–429, 12 2001.

[35] T.A. Collings. Transverse compressive behaviour of unidirectional carbon fibre reinforced plastics. *Composites*, 5(3):108 – 116, 1974.

[36] M.L. Costa, S.F.M. De Almeida, and M.C. Rezende. The influence of porosity on the interlaminar shear strength of carbon/epoxy and carbon/bismaleimide fabric laminates. *Composites Science and Technology*, 61(14):2101 – 2108, 2001.

[37] A.H. Cottrell. Strong solids. *Proceedings of the Royal Society A: Mathematical, Physical and Engineering Sciences*, 282(1388):2–9, 1964.

[38] H.L. Cox. The elasticity and strength of paper and other fibrous materials. *British Journal of Applied Physics*, 3(3), 1952.

[39] G. Curtis, J. Milne, and W. Reynolds. Non-hookean behaviour of strong carbon fibres. *Nature*, 220:1024–1025, 1968.

[40] ASTM D 2734-16. Standard test method for void content of reinforced plastics. Technical report, ASTM, 2016.

[41] P. Davies, F. Mazéas, and P. Casari. Sea water aging of glass reinforced composites: Shear behaviour and damage modelling. *Journal of Composite Materials*, 35(15):1343–1372, 2001.

[42] W.J. Drugan and J.R. Willis. A micromechanics-based nonlocal constitutive equation and estimates of representative volume element size for elastic composites. *Journal of the Mechanics and Physics of Solids*, 44(4):497–524, 1996.

[43] M. El Asloun, J.B. Donnet, G. Guilpain, M. Nardin, and J. Schultz. On the estimation of the tensile strength of carbon fibres at short lengths. *Journal of Materials Science*, 24(10):3504–3510, 1989.

[44] A. Farouk, N. Langrana, and G. Weng. Modulus prediction of a cross-ply fiber reinforced fabric composite with voids. *Polymer Composites*, 13(4):285–294, 1992.

[45] L. Feret. La grosseur des grains des matières pulvérulentes. *Premières Commun. la Nouv. Assoc. Int. l'essai matér.*, pages 428 – 436, 1930. groupe D.

[46] B. Fiedler, A. Klisch, and K. Schulte. Stress concentrations in multiple fibre model composites. *Composites Part A: Applied Science and Manufacturing*, 29(9):1013 – 1019, 1998.

[47] K.W. Gan, M.R. Wisnom, and S.R. Hallett. Effect of high through-thickness compressive stress on fibre direction tensile strength of carbon/epoxy composite laminates. *Composites Science and Technology*, 90:1–8, 2014.

[48] K. Goto, M. Arai, M. Nishimura, and K. Dohi. Strength evaluation of unidirectional carbon fiber-reinforced plastic laminates based on tension-compression biaxial stress tests. *Advanced Composite Materials*, 27(4):413–426, 2018.

[49] H.A.L. Guerin and D.M. Elliott. Degeneration affects the fiber reorientation of human annulus fibrosus under tensile load. *Journal of Biomechanics*, 39(8):1410 – 1418, 2006.

[50] A.L. Gurson. Continuum theory of ductile rupture by void nucleation and growth: Part I — Yield criteria and flow rules for porous ductile media. *Journal of Engineering Materials and Technology*, 99(1):2–15, 1977.

[51] Y.K. Hamidi, L. Aktas, and M.C. Altan. Three-dimensional features of void morphology in resin transfer molded composites. *Composites Science and Technology*, 65(7):1306 – 1320, 2005.

[52] Z. Hashin. The elastic moduli of heterogeneous materials. *Journal of Applied Mechanics*, 29:143–150, 1962.

[53] Z. Hashin. Analysis of composite materials: A survey. *Journal of Applied Mechanics*, 50(3):481–505, 1983.

[54] J.M. Hedgepeth. Stress concentrations in filamentary structures. *Report, NASA TND882, Langley Research Center*, 1961.

[55] J.M. Hedgepeth and P. VanDyke. Local stress concentrations in imperfect filamentary composite materials. *Journal of composite materials*, 1:294–309, 1967.

[56] S. Hernández, F. Sket, J.M. Molina-Aldareguia, C. González, and J. Llorca. Effect of curing cycle on void distribution and interlaminar shear strength in polymer-matrix composites. *Composites Science and Technology*, 71(10):1331 – 1341, 2011.

[57] S. Hernández, F. Sket, C. González, and J. Llorca. Optimization of curing cycle in carbon fiber-reinforced laminates: Void distribution and mechanical properties. *Composites Science and Technology*, 85:73 – 82, 2013.

[58] E. Hervé and A. Zaoui. Elastic behaviour of multiply coated fibre-reinforced composites. *International Journal of Engineering Science*, 33(10):1419 – 1433, 1995.

[59] R. Hill. Elastic properties of reinforced solids: Some theoretical principles. *Journal of the Mechanics and Physics of Solids*, 11(5):357–372, 1963.

[60] R. Hill. A self-consistent mechanics of composite materials. *Journal of the Mechanics and Physics of Solids*, 13(4):213 – 222, 1965.

[61] P.J. Hine, R.A. Duckett, A.S. Kaddour, M.J. Hinton, and G.M. Wells. The effect of hydrostatic pressure on the mechanical properties of glass fibre/epoxy unidirectional composites. *Composites Part A: Applied Science and Manufacturing*, 36(2):279 – 289, 2005.

[62] M.J Hinton and P.D Soden. Predicting failure in composite laminates: the background to the exercise. *Composites Science and Technology*, 58(7):1001 – 1010, 1998.

[63] J.W. Hitchon and D.C. Phillips. The effect of specimen size on the strength of cfrp. *Composites*, 9(2):119–124, 1978.

[64] J.W. Hitchon and D.C. Phillips. The dependence of the strength of carbon fibres on length. *Fibre Science and Technology*, 12:217–233, 1979.

[65] A. Hocine, D. Chapelle, M.L. Boubakar, A. Benamar, and A. Bezazi. Experimental and analytical investigation of the cylindrical part of a metallic vessel reinforced by filament winding while submitted to internal pressure. *International Journal of Pressure Vessels and Piping*, 86(10):649–655, 2009.

[66] D. K. Hsu and S. M. Nair. Evaluation of porosity in graphite-epoxy composite by frequency dependence of ultrasonic attenuation. In Donald O. Thompson and Dale E. Chimenti, editors, *Review of Progress in Quantitative Nondestructive Evaluation*, pages 1185–1193, Boston, MA, 1987. Springer US.

[67] D.K. Hsu and K.M. Uhl. A morphological study of porosity defects in graphite-epoxy composites. In Donald O. Thompson and Dale E. Chimenti, editors, *Review of Progress in Quantitative Nondestructive Evaluation*, pages 1175–1184, Boston, MA, 1987. Springer US.

[68] H. Huang and R. Talreja. Effects of void geometry on elastic properties of unidirectional fiber reinforced composites. *Composites Science and Technology*, 65(13):1964 – 1981, 2005.

[69] Y. Huang, J. Varna, and R. Talreja. Statistical methodology for assessing manufacturing quality related to transverse cracking in cross ply laminates. *Composites Science and Technology*, 95:100 – 106, 2014.

[70] T. Ishikawa, M. Matsushima, and Y. Hayashi. Hardening non-linear behaviour in longitudinal tension of unidirectional carbon composites. *Journal of Materials Science*, 20(11):4075–4083, 1985.

[71] F. Islam, S. Joannès, and L. Laiarinandrasana. Evaluation of critical parameters in tensile strength measurement of single fibres. *Journal of Composites Science*, 3(69), 2019.

[72] H. Jeong. Effects of voids on the mechanical strength and ultrasonic attenuation of laminated composites. *Journal of Composite Materials*, 31(3):276–292, 1997.

[73] D. Jeulin, T. Kanit, and S. Forest. Representative volume element: A statistical point of view. In David J. Bergman and Esin Inan, editors, *Continuum Models and Discrete Systems*, pages 21–27, Dordrecht, 2004. Springer Netherlands.

[74] D.J. Johnson. Structure property relationships in carbon fibers. *Journal of Physics D - Applied Physics*, 20(3):286–291, 1987.

[75] K.D. Jones and A.T. DiBenedetto. Fiber fracture in hybrid composite systems. *Composites Science and Technology*, 51(1):53 – 62, 1994.

[76] J. Kakakasery, V. Arumugam, K. Abdul Rauf, D. Bull, A.R. Chambers, C. Scarponi, and C. Santulli. Cure cycle effect on impact resistance under elevated temperatures in carbon prepreg laminates investigated using acoustic emission. *Composites Part B: Engineering*, 75:298–306, 2015.

[77] T. Kanit, S. Forest, I. Galliet, V. Mounoury, and D. Jeulin. Determination of the size of the representative volume element for random composites: statistical and numerical approach. *International Journal of Solids and Structures*, 40(13):3647–3679, 2003.

[78] A. Kelly and W.R. Tyson. Tensile properties of fibre-reinforced metals: Copper/tungsten and copper/molybdenum. *Journal of the Mechanics and Physics of Solids*, 13(6):329–350, 1965.

[79] S. Kohler, J. Cugnoni, R. Amacher, and J. Botsis. Transverse cracking in the bulk and at the free edge of thin-ply composites: Experiments and multiscale modelling. *Composites Part A: Applied Science and Manufacturing*, 124:105–468, 2019.

[80] E.J. Kohn, A.G. Sands, and R.C. Clark. Quantitative measurement of void content in glass-filament-wound composites and correlation of interlaminar shear strength with void content. *I&EC Product Research and Development*, 7(3):179–183, 1968.

[81] K.K. Kratmann, MP.F. Sutcliffe, L.T. Lilleheden, L.T. Pyrz, and O.T Thomsen. A novel image analysis procedure for measuring fibre misalignment in unidirectional fibre composites. *Composites Science and Technology*, 69(2):228–238, 2009.

[82] R. Kumar, J. Villanova, P. Lhuissier, and L. Salvo. In situ nanotomography study of creep cavities in al-3.6-cu alloy. *Acta Materialia*, 166:18 – 27, 2019.

[83] L. Laiarinandrasana, J. Besson, M. Lafarge, and G. Hochstetter. Temperature dependent mechanical behaviour of PVDF: Experiments and numerical modelling. *International Journal of Plasticity*, 25(7):1301–1324, 2009.

[84] L. Laiarinandrasana, O. Klinkova, F. Nguyen, H. Proudhon, T.F. Morgeneyer, and W. Ludwig. Three dimensional quantification of anisotropic void evolution in deformed semi-crystalline polyamide 6. *International Journal of Plasticity*, 83:19–36, 2016.

[85] L. Laiarinandrasana, T.F. Morgeneyer, Y. Cheng, L. Helfen, V. Le Saux, and Y. Marco. Microstructural observations supporting thermography measurements for short glass fibre thermoplastic composites under fatigue loading. *Contin. Mech. Thermodyn.*, pages 1–19, 2019.

[86] E.N. Landis and D.T. Keane. X-ray microtomography. *Materials Characterization*, 61(12):1305–1316, 2010.

[87] C. Lantuéjoul. Ergodicity and integral range. *Journal of Microscopy*, 161(3):387–403, 1991.

[88] J.E. Little, X. Yuan, and M.I. Jones. Characterisation of voids in fibre reinforced composite materials. *NDT&E International*, 46:122 – 127, 2012.

[89] L. Liu, B.M. Zhang, D.F. Wang, and Z.J. Wu. Effects of cure cycles on void content and mechanical properties of composite laminates. *Composite Structures*, 73(3):303 – 309, 2006.

[90] A. Madra, N. El Hajj, and M. Benzeggagh. X-ray microtomography applications for quantitative and qualitative analysis of porosity in woven glass fiber reinforced thermoplastic. *Composites Science and Technology*, 95:50 – 58, 2014.

[91] G.W. Mair. *Safety Assessment of Composite Cylinder for Gas Storage by Statistical Methods*. Springer International Publishing, 1st edition, 2017.

[92] J.P. Marquez. Fourier analysis and automated measurement of cell and fiber angular orientation distributions. *International Journal of Solids and Structures*, 43(21):6413 – 6423, 2006.

[93] G. Matheron. *The Theory of Regionalized Variables and Its Applications*. Les Cahiers du Centre de Morphologie Mathématique de Fontainebleau, 1971.

[94] G. Matheron. *Estimating and Choosing. An Essay on Probability in Practice*. Springer-Verlag, 1989.

[95] R. Maurin, P. Davies, N. Baral, and C. Baley. Transverse properties of carbon fibres by nano-indentation and micro-mechanics. *Applied Composite Materials*, 15(2):61, 2008.

[96] M. Mehdikhani. *Effect of Voids on Damage Development in Carbon Fiber-reinforced Polymer Composites*. PhD thesis, KU Leuven, 2018.

[97] M. Mehdikhani, L. Gorbatikh, I. Verpoest, and S.V. Lomov. Voids in fiber-reinforced polymer composites: A review on their formation, characteristics, and effects on mechanical performance. *Journal of Composite Materials*, 53(12):1579–1669, 2019.

[98] M. Mehdikhani, E. Steensels, A. Standaert, K.A.M. Vallons, L. Gorbatikh, and S.V. Lomov. Multi-scale digital image correlation for detection and quantification of matrix cracks in carbon fiber composite laminates in the absence and presence of voids controlled by the cure cycle. *Composites Part B: Engineering*, 154:138–147, 2018.

[99] Ministère de la transition écologique et solidaire. Dossier de presse - Plan de déploiement de l'hydrogène pour la transition énergétique. 2018. Retrieved from: https://www.ecologique-solidaire.gouv.fr/plan-hydrogene-outil-davenir-transition-energetique (12/01/2020).

[100] H. Miyagawa, C. Sato, T. Mase, E. Drown, L.T. Drzal, and K. Ikegami. Transverse elastic modulus of carbon fibers measured by Raman spectroscopy. *Materials Science and Engineering: A*, 412(1-2):88–92, 2005.

[101] X.P. Morelle, J. Chevalier, C. Bailly, T. Pardoen, and F. Lani. Mechanical characterization and modeling of the deformation and failure of the highly crosslinked RTM6 epoxy resin. *Mechanics of Time-Dependent Materials*, 21(3):419–454, 2017.

[102] R. Moreton and W. Watt. Tensile strength of carbon fibers. *Nature*, 247:360–361, 1974.

[103] T. Mori and K. Tanaka. Average stress in matrix and average elastic energy of materials with misfitting inclusions. *Acta Metallurgica*, 21(5):571–574, 1973.

[104] A.P. Mouritz. Ultrasonic and interlaminar properties of highly porous composites. *Journal of Composite Materials*, 34(3):218–239, 2000.

[105] M. Nakada, Y. Miyano, M. Kinoshita, R. Koga, T. Okuya, and R. Muki. Time-temperature dependence of tensile strength of unidirectional CFRP. *Journal of Composite Materials*, 36(22):2567–2581, 2002.

[106] M.R. Nedele and M.R. Wisnom. Three-dimensional finite element analysis of the stress concentration at a single fibre break. *Composites Science and Technology*, 51(4):517 – 524, 1994.

[107] Y. Nikishkov, L. Airoldi, and A. Makeev. Measurement of voids in composites by X-ray computed tomography. *Composites Science and Technology*, 89:89–97, 2013.

[108] M.S. Nixon and A. Aguado. *Feature Extraction & Image Processing for Computer Vision, Third Edition*. Academic Press, December 2012.

[109] J. Noda, M. Nakada, and Y. Miyaho. Temperature dependence of accumulation of fiber breakages under tensile loading for unidirectional cfrp laminates. *Journal of Reinforced Plastics and Composites*, 27(10):1005–1019, 2008.

[110] J. Noda, T. Okabe, N. Takeda, and M. Shimizu. Tensile strength of CFRP cross-ply laminates containing transverse cracks. *Advanced Composite Materials*, 15(1):81–93, 2006.

[111] T. Okabe, H. Sekine, K. Ishii, M. Nishikawa, and N. Takeda. Numerical method for failure simulation of unidirectional fiber-reinforced composites with spring element model. *Composites Science and Technology*, 65(6):921–933, 2005.

[112] H. Okuda, R.J. Young, F. Tanaka, J. Watanabe, and T. Okabe. Tensile failure phenomena in carbon fibres. *Carbon*, 107:474–481, 2016.

[113] P. Olivier, J.P. Cottu, and B. Ferret. Effects of cure cycle pressure and voids on some mechanical properties of carbon/epoxy laminates. *Composites*, 26(7):509 – 515, 1995.

[114] R. Olsson. A survey of test methods for multiaxial and out-of-plane strength of composite laminates. *Composites Science and Technology*, 71(6):773–783, 2011.

[115] N. Otsu. A threshold selection method from gray-level histograms. *IEEE Transactions on Systems, Man, and Cybernetics*, 9(1):62–66, 1979.

[116] T.V. Parry and A.S. Wronski. The effect of hydrostatic pressure on the tensile properties of pultruded cfrp. *Journal of Materials Science*, 20(6):2141–2147, 1985.

[117] T.V. Parry and A.S. Wronski. The tensile properties of pultruded grp tested under superposed hydrostatic pressure. *Journal of Materials Science*, 21(12):4451–4455, 1986.

[118] A. Parvizi, K.W. Garrett, and J.E. Bailey. Constrained cracking in glass fibre-reinforced epoxy cross-ply laminates. *Journal of Materials Science*, 13(1):195–201, 1978.

[119] E. Pérez-Pacheco, J.I. Cauich-Cupul, A. Valadez-González, and P.J. Herrera-Franco. Effect of moisture absorption on the mechanical behavior of carbon fiber/epoxy matrix composites. *Journal of Materials Science*, 48(5):1873–1882, 2013.

[120] A. Pilato. *Caractérisation des structures composites bobinées épaisses, application à l'étude du comportement de réservoirs de stockage d'hydrogène.* PhD thesis, Université Bordeaux 1, 2011.

[121] S. Pimenta. *Fibre failure modelling*, pages 193–224. 2015.

[122] S. Pimenta and S.T. Pinho. Hierarchical scaling law for the strength of composite fibre bundles. *Journal of the Mechanics and Physics of Solids*, 61(6):1337 – 1356, 2013.

[123] P.A. Poulet. *Effet de la variabilité microstructurale sur le comportement d'un composite UD verre/PA11 : de la caractérisation expérimentale à la modélisation multi-échelle.* PhD thesis, Ecole des Mines de Paris, 2017.

[124] B. Pourdeyhimi, R. Dent, and H. Davis. Measuring fiber orientation in nonwovens. Part III: Fourier transform. *Textile Research Journal*, 67(2):143–151, 1997.

[125] S. Preibisch, S. Saalfeld, and P. Tomancak. Globally optimal stitching of tiled 3D microscopic image acquisitions. *Bioinformatics*, 25(11):1463–1465, 2009.

[126] J.M.S. Prewitt and M.L. Mendelsohn. The analysis of cell images. *Annals of the New York Academy of Sciences*, 128(3):1035–1053, 1966.

[127] D. Purslow. On the optical assessment of the void content in composite materials. *Composites*, 15:207–210, 1984.

[128] C. Pélissou, J. Baccou, Y. Monerie, and F. Perales. Determination of the size of the representative volume element for random quasi-brittle composites. *International Journal of Solids and Structures*, 46(14-15):2842–2855, 2009.

[129] D. Raz-Ben Aroush, E. Maire, C. Gauthier, S. Youssef, P. Cloetens, and H.D. Wagner. A study of fracture of unidirectional composites using in situ high-resolution synchrotron X-ray microtomography. *Composites Science and Technology*, 66(10):1348 – 1353, 2006.

[130] T. Rev, G. Czel, and M.R. Wisnom. A novel test method to induce bi-axial stress states in thin-ply carbon composites under combined longitudinal tension and transverse compression. In *American Society for Composites 2018, 33rd Technical Conference*, Seattle, September 2018.

[131] J. Rojek, C. Breite, Y. Swolfs, and L. Laiarinandrasana. Void growth measurement and modelling in a thermosetting epoxy resin using sem and tomography techniques. *Continuum Mechanics and Thermodynamics*, 2020.

[132] B.W. Rosen. Tensile failure of fibrous composites. *AIAA Journal*, 2(11):1985–1991, 1964.

[133] H. Saito, H. Takeuchi, and I. Kimpara. Experimental evaluation of the damage growth restraining in 90 layer of thin-ply cfrp cross-ply laminates. *Advanced Composite Materials*, 21(1):57–66, 2012.

[134] J. Schindelin, I. Arganda-Carreras, E. Frise, V. Kaynig, M. Longair, T. Pietzsch, S. Preibisch, C. Rueden, S. Saalfeld, B. Schmid, J.-Y. Tinevez, D. J. White, V. Hartenstein, K. Eliceiri, P. Tomancak, and A. Cardona. Fiji: an open-source platform for biological-image analysis. *Nat. Methods*, 9:676–682, 2012.

[135] A.E. Scott. *Analysis of a hybrid composite pressure vessel using multi-scale computed tomography techniques*. PhD thesis, University of Southampton, 2011.

[136] A.E. Scott, M. Mavrogordato, P. Wright, I. Sinclair, and S.M. Spearing. In situ fibre fracture measurement in carbon-epoxy laminates using high resolution computed tomography. *Composites Science and Technology*, 71(12):1471 – 1477, 2011.

[137] A.E. Scott, I. Sinclair, S.M. Spearing, M.N. Mavrogordato, and W. Hepples. Influence of voids on damage mechanisms in carbon/epoxy composites determined via high resolution computed tomography. *Composites Science and Technology*, 90:147 – 153, 2014.

[138] A.E. Scott, I. Sinclair, S.M. Spearing, A. Thionnet, and A.R. Bunsell. Damage accumulation in a carbon/epoxy composite: Comparison between a multiscale model and computed tomography experimental results. *Composites: Part A*, 43:1514–1522, 2012.

[139] T.A. Sebaey, J. Costa, P. Maim
i, Y. Batista, N. Blanco, and J.A. Mayugo. Measurement of the in situ transverse tensile strength of composite plies by means of the real time monitoring of microcracking. *Composites Part B: Engineering*, 65:40 – 46, 2014.

[140] N. Selles, A. King, H. Proudhon, N. Saintier, and L. Laiarinandrasana. Time dependent voiding mechanisms in polyamide 6 submitted to high stress triaxiality: experimental characterisation and finite element modelling. *Mechanics of Time-Dependent Materials*, 22(3):351–371, 2018.

[141] C.H. Shen and G.S. Springer. Effects of moisture and temperature on the tensile strength of composite materials. *Journal of Composite Materials*, 11(1):2–16, 1977.

[142] M. Shioya, E. Hayakawa, and A. Takaku. Non-hookean stress-strain response and changes in crystallite orientation of carbon fibres. *Journal of Materials Science*, 31(17):4521–4532, 1996.

[143] R.H. Sigley, A.S. Wronski, and T.V. Parry. Tensile failure of pultruded glass-polyester composites under superimposed hydrostatic pressure. *Composites Science and Technology*, 41(4):395 – 409, 1991.

[144] A. Siriruk and D. Penumadu. *Effect of Sea Water on Polymeric Marine Composites*, pages 129–142. Springer Netherlands, Dordrecht, 2014.

[145] S. Sisodia, E.K. Gamstedt, F. Edgren, and J. Varna. Effects of voids on quasi-static and tension fatigue behaviour of carbon-fibre composite laminates. *Journal of Composite Materials*, 49(17):2137–2148, 2015.

[146] A.G. Stamopoulos, K.I. Tserpes, P. Prucha, and D. Vavrik. Evaluation of porosity effects on the mechanical properties of carbon fiber-reinforced plastic unidirectional laminates by X-ray computed tomography and mechanical testing. *Journal of Composite Materials*, 50(15):2087–2098, 2016.

[147] D.E.W. Stone and B. Clarke. Ultrasonic attenuation as a measure of void content in carbon-fibre reinforced plastics. *Non-Destructive Testing*, 8(3):137–145, 1975.

[148] A. Brent Strong. *Fundamentals of Composites Manufacturing: Materials, Methods and Applications*, chapter 17, pages 437–451. Society of Manufacturing Engineers, 2nd edition, 11 2007.

[149] Y. Swolfs, L. Gorbatikh, V. Romanov, S. Orlova, S.V. Lomov, and I. Verpoest. Stress concentrations in an impregnated fibre bundle with random fibre packing. *Composites Science and Technology*, 74:113 – 120, 2013.

[150] Y. Swolfs, I. Verpoest, and L. Gorbatikh. A review of input data and modelling assumptions in longitudinal strength models for unidirectional fibre-reinforced composites. *Composite Structures*, 150:153–172, 2016.

[151] N. Takeda and S. Ogihara. In situ observation and probabilistic prediction of microscopic failure processes in cfrp cross-ply laminates. *Composites Science and Technology*, 52(2):183 – 195, 1994.

[152] R. Talreja. On failure theories for composite materials. In K. Naumenko and M. Aßmus, editors, *Advanced Methods of Continuum Mechanics for Materials and Structures*, pages 379–388. Springer Singapore, Singapore, 2016.

[153] R.P. Tavares, F. Otero, A. Turon, and P.P. Camanho. Effective simulation of the mechanics of longitudinal tensile failure of unidirectional polymer composites. *International Journal of Fracture*, 208(1):269–285, 2017.

[154] A. Thionnet, H.Y. Chou, and A. Bunsell. Fibre break processes in unidirectional composites. *Composites Part A: Applied Science and Manufacturing*, 65:148–160, 2014.

[155] J. Thomason. On the application of weibull analysis to experimentally determined single fibre strength distributions. *Composites Science and Technology*, 77:74–80, 2013.

[156] J.L. Thomason. The interface region in glass fibre-reinforced epoxy resin composites: 1. sample preparation, void content and interfacial strength. *Composites*, 26(7):467–475, 1995.

[157] M.T. Todinov. Is Weibull distribution the correct model for predicting probability of failure initiated by non-interacting flaws? *International Journal of Solids and Structures*, 46(3):887 – 901, 2009.

[158] O. Tsugiyuki, M. Nakada, and Y. Miyano. Temperature dependence of longitudinal tensile strength in unidirectional carbon fiber-reinforced plastic. *Journal of Composite Materials*, 48(28):3569–3573, 2014.

[159] V. Tvergaard. Influence of void nucleation on ductile shear fracture at a free surface. *Journal of the Mechanics and Physics of Solids*, 30(6):399 – 425, 1982.

[160] V. Tvergaard and A. Needleman. Analysis of the cup-cone fracture in a round tensile bar. *Acta Metallurgica*, 32(1):157 – 169, 1984.

[161] P.W.J. van den Heuvel, T. Peijs, and R.J. Young. Failure phenomena in two-dimensional multifibre microcomposites: 2. a raman spectroscopic study of the influence of inter-fibre spacing on stress concentrations. *Composites Science and Technology*, 57(8):899 – 911, 1997.

[162] P.W.J. van den Heuvel, Y.J.W. van der Bruggen, and T. Peijs. Failure phenomena in multi-fibre model composites: Part 1. an experimental investigation into the influence of fibre spacing and fibre—matrix adhesion. *Composites Part A: Applied Science and Manufacturing*, 27(9):855 – 859, 1996.

[163] W.H.M. Van Dreumel and J.L.M. Kamp. Non Hookean behaviour in the fibre direction of carbon-fibre composites and the influence of fibre waviness on the tensile properties. *Journal of Composite Materials*, 11(4):461–469, 1977.

[164] F. Vautard, J. Dentzer, M. Nardin, J. Schultz, and B. Defoort. Influence of surface defects on the tensile strength of carbon fibers. *Applied Surface Science*, 322:185–193, 2014.

[165] J. Watanabe, F. Tanaka, R. Higuchi, H. Matsutani, H. Okuda, and T. Okabe. A study of stress concentrations around fiber breaks in unidirectional CF/epoxy composites using double-fiber fragmentation tests. *Advanced Composite Materials*, 27(6):575–587, 2018.

[166] J. Watanabe, F. Tanaka, H. Okuda, and T. Okabe. Tensile strength distribution of carbon fibers at short gauge lengths. *Advanced Composite Materials*, 23(5-6):535–550, 2014.

[167] M.C. Waterbury and L.T. Drzal. Determination of fiber volume fractions by optical numeric volume fraction analysis. *Journal of Reinforced Plastics and Composites*, 8(6):627–636, 1989.

[168] A.S. Watson and R.L. Smith. An examination of statistical theories for fibrous materials in the light of experimental data. *Journal of Materials Science*, 20(9):3260–3270, 1985.

[169] W. Weibull. A statistical theory of the strength of materials. *Ingeoniorstenskaps Academian Handlingar*, 1939.

[170] T. Weitkamp, M. Scheel, J.L. Giorgetta, V. Joyet, V. Le Roux, G. Cauchon, T. Moreno, F. Polack, A. Thompson, and J.P. Samama. The tomography beamline ANATOMIX at synchrotron SOLEIL. *Journal of Physics: Conference Series*, 849:12–37, 2017.

[171] M.P. Widjaja, S. Joannès, A. Bunsell, G. Mair, and A. Thionnet. Defining a reduced volume zone for the simulation of burst test on a composite pressure vessels. In *ICSAAM 2018 - 8th International Conference on Structural Analysis of Advanced Materials*, Tarbes, France, August 2018.

[172] M.R. Wisnom. Size effects in the testing of fibre-composite materials. *Composites Science and Technology*, 59(13):1937 – 1957, 1999.

[173] Y. Wu, R. Shivpuri, and L.J. Lee. Effect of macro and micro voids on elastic properties of polymer composites. *Journal of Reinforced Plastics and Composites*, 17(15):1391–1402, 1998.

[174] Z. Xia, W.A. Curtin, and P.W.M. Peters. Multiscale modeling of failure in metal matrix composites. *Acta Materialia*, 49(2):273 – 287, 2001.

[175] G. Yamamoto, M. Onodera, K. Koizumi, J. Watanabe, H. Okuda, F. Tanaka, and T. Okabe. Considering the stress concentration of fiber surfaces in the prediction of the tensile strength of unidirectional carbon fiber-reinforced plastic composites. *Composites Part A: Applied Science and Manufacturing*, 121:499 – 509, 2019.

[176] P. Yang and R. Elhajjar. Porosity content evaluation in carbon-fiber/epoxy composites using X-ray computed tomography. *Polymer-Plastics Technology and Engineering*, 53(3):217–222, 2014.

[177] J. Yao, W. Yu, and D. Pan. Tensile strength and its variation of PAN-based carbon fibers. III. weak-link analysis. *Journal of Applied Polymer Science*, 110(6):3778–3784, 2008.

[178] Q. Zheng and R.J. Morgan. Synergistic thermal-moisture damage mechanisms of epoxies and their carbon fiber composites. *Journal of Composite Materials*, 27(15):1465–1478, 1993.

[179] P.A. Zinoviev and S.V. Tsvetkov. Mechanical properties of unidirectional organic-fiber-reinforced plastics under hydrostatic pressure. *Composites Science and Technology*, 58(1):31 – 39, 1998.

[180] P.A. Zinoviev, S.V. Tsvetkov, G.G. Kulish, R.W. van den Berg, and L.J.M.M. Van Schepdael. The behavior of high-strength unidirectional composites under tension with superposed hydrostatic pressure. *Composites Science and Technology*, 61(8):1151–1161, 2001.

[181] C. Zweben. Tensile failure of fiber composites. *AIAA Journal*, 6(12):2325–2331, 1968.

[182] C. Zweben. Is there a size effect in composites? *Composites*, 25(6):451–454, 1994.

RÉSUMÉ

Dans cette thèse, on analyse l'effet de la porosité sur le comportement mécanique d'un matériau composite à fibres de carbone utilisé dans le cadre d'applications à hautes performances. Les réservoirs hyperbare destinés au stockage de l'hydrogène en sont un exemple. Du fait de leur fabrication par enroulement filamentaire, ces structures à parois épaisses présentent des taux de porosité parfois très élevés. La conséquence de telles porosités sur la durabilité des réservoirs et plus largement sur des structures composites chargées de manière multi-axiale est très peu documentée. Les travaux présentés ici s'inscrivent par ailleurs dans le développement d'un modèle existant à MINES ParisTech et ayant fait ses preuves pour prédire la résistance de composites unidirectionnels. Il s'agit ici de perfectionner ce modèle en intégrant de nouveaux facteurs comme les porosités. Des observations (tomographie aux rayons X et microscopie optique) d'un réservoir sont réalisées afin de caractériser les vides et leur distribution au sein de la structure. En parallèle, une étude expérimentale est conduite sur des éprouvettes à différents taux de porosité. La résistance de ces éprouvettes, chargées simultanément en traction longitudinale et compression transverse, est évaluée grace à un système expérimental spécialement conçu. A des échelles encore plus fines, des essais sont réalisés sur des échantillons d'époxy entaillés pour caractériser la croissance des cavités microscopiques et le comportement mécanique de la résine sous un état des contraintes multi-axial. Toutes ces données expérimentales sont ensuite exploitées et intégrées dans le modèle numérique afin de simuler le comportement à rupture d'un réservoir à parois épaisses.

MOTS CLÉS

composites, époxy, fibres de carbone, modélisation, éléments finis, tomographie

ABSTRACT

The topic of this thesis is the influence of voids on the mechanical properties of carbon fibre reinforced polymers used in high performance applications, such as pressure vessels for hydrogen storage. Manufactured through filament winding, these thick-walled structures can show a significant void content. The effect of these voids on the strength of pressure vessels and, more in general, on the strength of composite structures subjected to multiaxial loads, is not thoroughly understood. The work presented in this thesis is carried out in the context of an existing model of tensile failure of unidirectional composites developed at MINES ParisTech. The objective of the work presented here is to take into account additional factors, such as void content. X-ray tomography and optical microscopy observations are carried out to characterize voids in a carbon-epoxy pressure vessel. In another experimental study, mechanical tests are performed on carbon-epoxy specimens with different levels of void content. The influence of a biaxial load (longitudinal tension and through-thickness compression) is evaluated using a custom-designed experimental setup. At the microscopic scale, tests on notched epoxy specimens are carried out to investigate microscopic void growth and the mechanical behaviour of the resin under a multiaxial stress state. Finally, a numerical approach to modelling failure of a thick-walled cylinder is proposed in the framework of the multiscale fibre break model, taking into account the experimental observations.

KEYWORDS

composites, epoxy, carbon fibres, modelling, finite element analysis, computed tomography